EUROPEAN ORGANIZATION FOR NUCLEAR RESEARCH

CERN-SPSC-2023-XXX
SPSC-SR-XXX
November 7, 2023

COMPASS Status Report 2023

The COMPASS Collaboration

Abstract

The report reviews the activities and achievements of the Collaboration from July 2022 to October 2023. An overview of the 2022 data-taking is presented. The results and ongoing analysis of the data collected in 2022 and previous years are discussed.

Contents

1 Introduction

The report describes the progress in the analysis of COMPASS data for both hadron spectroscopy and the structure of the nucleon in the period from July 2022 to October 2023. It illustrates the status of the various analyses and the main results. The report contains a section dedicated to the summary of the COMPASS apparatus performance during the physics Run of 2022 with polarised muons and transversely polarised deuteron target.

In section 2, the analysis of peripheral hadron-beam scattering data is presented and the rich results coming from the studies of diffractive dissociation reactions are discussed. In Primakoff reactions, various final states are being investigated: quasi-elastic Compton scattering, single and double π^0 production, $\pi^+ \pi^-$ production, etc. Currently, the main focus lies on the study of single π^0 production. In diffractive dissociation reactions, the study of excited meson resonances produced progressed by applying sophisticated partial-wave analysis (PWA) techniques to decompose the coherent superposition of amplitudes and to determine the strength and phase of the contributing partial waves. In addition, novel analysis techniques are developed utilizing the unprecedented precision of the COMPASS data. Currently, we are focused on searches for the spin-exotic $\pi_1(1600)$ in various final states such as $b_1(1235)\pi$, $f_1(1285)\pi$, $\eta^{(\prime)}\pi$, and $K^- K^0_S K^0_S$. This is complemented by exploring the strange-meson spectrum in kaon diffraction into the $K^-\pi^-\pi^+$ final state.

The nucleon structure studies are described in Sections 3–5. The analyses of exclusive meson production channels from the 2012 data have been finalized: results for ρ^0 Spin Density Matrix Elements (SDME) have recently been published [1]. The analyses of the data collected in 2016–2017 with the muon beam and a 2.5 m long liquid H_2 target progressed significantly. The data have been re-processed with several improvements (updated calibrations, fixed alignment problems, etc.). On the Monte-Carlo side, several adjustments have been made to the event generators (HEPGen++, DJANGOH), which lead to improvements in the exclusive analyses (π^0, DVCS) and an improved description of radiative processes (evaluation of radiative corrections). All 2016 analyses (DVCS and exclusive π^0, ϕ and J/ψ channel studies) have been redone with newly processed data. A significant progress has been achieved for the Deeply Virtual Compton Scattering (DVCS) data analysis. The results are now close to a final shape and the 2016 analysis is planned to be accomplished soon and prepared for a publication. The exclusive π^0 production cross section studies have been finalised and released. Some systematic tests are still ongoing, but the preparations for the paper drafting have already been started. The extraction of the SDMEs for exclusive ϕ production is progressing, as well as the exploratory study for exclusive J/ψ-production cross section measurement (potentially also the SDME extraction). In the meantime, a global alignment quality test has been launched for 2017 data. Several issues have been identified and are now being addressed. The data is being prepared for future re-processing, e.g. we are now checking final ECAL and RICH calibrations.

We have concluded the analysis of charged pion and kaon multiplicities from the 2016 data. The main missing piece for this analysis was the accounting for radiative effects, which was recently accomplished. The results are now being prepared for a publication. The TMD analysis of the large sample of SIDIS events collected during 2016 is also advancing: the study of single-hadron unpolarized azimuthal asymmetries and hadron transverse momentum distributions has been extended to the entire 2016 sample. The results have been corrected for radiative effects. The systematic studies are still ongoing, but both asymmetry and hadron transverse momentum distribution analyses are close to the accomplishment.

Our results on transverse-spin-dependent azimuthal asymmetries of pion and kaon pairs produced in muon-proton and muon-deuteron semi-inclusive deep inelastic scattering and Collins and Sivers transverse-spin asymmetries in inclusive muoproduction of ρ^0 mesons have recently been published [2], [3]. Several studies for the transverse-spin dependent effects carried out on the 2010 proton sample, have been postponed. They will be accomplished in parallel with analogous analyses of freshly collected 2022 deuteron data. This concerns the study of unpolarized azimuthal asymmetries in hadron pair production, the same-charge dihadron Collins-like and Sivers-like transverse spin dependent asymmetries, the multi-D transverse-spin asymmetries, and the extraction of the g_2^{p} structure function.

In section 4 we present the progress in the analysis of the COMPASS Drell–Yan (DY) data collected in 2015 and in 2018. Our study dedicated to the double J/ψ production in pion-nucleon interactions has recently been published [4]. The paper draft with final results on transverse spin asymmetries in Drell–Yan process is in a final drafting stage and will be submitted to PRL in the course of 2023. The preliminary results of an analogous study carried out for the J/ψ mass range have been released. Obtained J/ψ transverse spin asymmetries were found to be small and compatible with zero. These results are expected to shed light on charmonia production mechanisms and possibly also gluon TMD PDFs. The cross-section extractions being carried out both for the Drell–Yan and J/ψ production channels have been accomplished and preliminary results have been released. Both analyses had a significant progress thanks to improvements in the Monte Carlo description of the setup and experimental conditions (detector and trigger efficiencies), and other technical aspects, such as revisiting the event selection criteria and systematic studies.

The analysis of the fresh 2022 data collected last year with longitudinally polarized 160 GeV/c muon beam and transversely polarized deuteron (^{6}LiD) target is in full swing. Several analysis activities have started already during the data taking (e.g. detector stability analyses, detector alignment, data quality tests). One of the key elements, the alignment campaign progressed fast and allowed us to perform twice the full processing of the entire 2022 sample, including all 10 periods (coupled weeks of data-taking). The processed data from the second production was considered to be good enough for asymmetry extraction analysis. All technical aspects of the analysis have been carefully addressed including: event selection procedure and requirements, thorough data quality and data stability tests, dilution factor evaluation, obtaining the target polarization values for all periods. The Collins and Sivers asymmetries have been extracted along with other transverse spin asymmetries. In the current stage of the analysis we focus on a detailed study of the Collins and Sivers terms. The extraction has been performed for different kinematic dependencies and ranges. The asymmetries have been scrutinized for systematic effects and possible biases. No critical issues have been identified, and the obtained results were considered as trustful. A tremendous work has been performed, leading to a first release of preliminary results for the Collins and Sivers asymmetries from about a half of the 2022 data sample. First extractions have also been performed for the dihadron Collins-like asymmetries. The results obtained for Collins and Sivers asymmetries look very promising, in particular clear indications for a small, non-zero effect has been observed for the Collins case at relatively large x-Bjorken range for both single-hadron and dihadron channels. The single hadron results for Collins and Sivers asymmetries have been presented at SPIN conference and dedicated paper drafting has already been started.

The main ongoing analyses and their status are summarized in the Table 1 and Table 2. The status the COMPASS spectrometer during the 2022 data taking is described in section 6. During the commissioning phase in 2022, the COMPASS spectrometer and target systems preparations progressed according to the original schedule. The commissioning of the detectors was accomplished in time and the physics data taking took place according to the schedule (from June 07 to November 09, about 150 days). The spectrometer performed stably during the Run, demonstrating overall 90% efficiency. No critical problems that could potentially harm physics results occurred during the data taking. The beam delivery by the accelerator complex was also stable with overall efficiency of about 73%. The total number of protons delivered on T6 production target reached 5.95×10^{18}, which amounts to 98% of the request. The last COMPASS data-taking performed in 2022 was highly successful.

Table 1: Summary of the results presented in the report.

Channel	**Status**	**Details**
Hadron data		
Chiral anomaly and radiative width of $\rho(770)$ in $\pi^-\gamma \to \pi^-\pi^0$	update	determine systematic uncertainties improve background subtraction
Study ambiguities in PWA	new	mathematical ambiguities in PWA of final states with two pseudoscalars
Technical advances for the $3\pi\gamma\gamma$ final state and beyond	update	reconstruction with improved ECAL calibration and improvements in detector simulation
Study of isovector resonances in $\pi^- p \to K^- K^0_\text{S} K^0_\text{S}\, p$	update	event selection finished
Development of novel methods for partial-wave analyses	new	impose continuity and regularization in PWA based on information-field theory
PWA of $\pi^- p \to \pi^-\pi^0\omega\, p$	update	partial-wave decomposition yielding potential $\pi_1(1600)$ signal
Study strange mesons in $K^- p \to K^-\pi^-\pi^+ p$	update	analysis finalized including measurement of 11 strange mesons, starting paper drafting
Study of exclusive reactions with 2012 data		
SDME for exclusive ρ	final	EPJC (2023) 83 924
Study of exclusive reactions with 2016 data		
DVCS cross section and t-slope	update	new production of 2016 data significant progress in the analysis
π^0 cross section t and ϕ dependence	final	preliminary results, new 2016 data production, finalizing systematics, starting paper drafting
J/ψ cross section	update	full 2016-2017 data processed, event selection, exploratory analysis (SDMEs)
SDME for exclusive ϕ	update	results with improved production of 2016 data cross-check of SDMEs
Study of exclusive reactions with 2017 data		
DVCS and exclusive π^0	new	verifying the alignment quality, several issues identified, work in progress
Hadron multiplicities with 2016 data		
hadron, pion and kaon multiplicities	final	preliminary 2016 results released, paper drafting, new radiative corrections applied
$\bar{\text{p}}$/p and K$^-$/K$^+$ multiplicity ratios	final	preliminary 2016 results released, paper drafting, new radiative corrections applied

Table 2: Summary of the results presented in the report.

Channel **Transverse spin and TMD analyses in SIDIS**	**Status**	**Details**
Collins and Sivers asymmetries (2022 data)	new	2022 data analysis in full swing, preliminary results released (50% of the data), paper drafting started
Dihadron Collins-like asymmetries (2022 data)	new	first look, exploratory analysis
MultiD analysis of transverse spin asymmetries (proton 2010 data)	postponed	to be resumed with a parallel 2022 analysis
Inclusive ρ^0 Collins and Sivers asymmetries, (proton 2010 data)	final	PLB 843 (2023) 137950
Measurement of g_2^{p} (SIDIS 2010 data)	postponed	to be resumed with a parallel 2022 analysis
Transverse and longitudinal spin asymmetries (proton 2007, 2010 and 2011 data)	ongoing	study of systematic effects and models, paper drafting
Dihadron transverse spin asymmetries with PID (proton 2010 and deuteron 2002-2004 data)	final	PLB 845 (2023) 138155
Dihadron Collins and Sivers asymmetries h^+h^+ and h^-h^-, (proton 2010 data)	postponed	to be resumed with a parallel 2022 analysis
Unpolarised azimuthal asymmetries (proton 2016/17 data)	update	new radiative corrections applied, systematics new improved production of 2016 data
Dihadron unpolarized azimuthal asymmetries h^+h^-, h^+h^+ and h^-h^-, (proton 2016/17 data)	postponed	to be resumed with a parallel 2022 analysis
P_T distributions in SIDIS on unpolarised proton data (2016/17)	update	new radiative corrections, systematics new improved production of 2016 data
Drell–Yan and Charmonium analyses		
Drell–Yan transverse spin asymmetries final results (2015+2018 data)	final	final drafting stage of the paper, enlarged mass range, submission in 2023
Transverse spin asymmetries in J/ψ mass range	update	preliminary results released, first ever measurement, interest from theorists
Drell–Yan unpolarized azimuthal asymmetries (Drell-Yan 2018 data)	ongoing	study of systematic effects
Double J/ψ production cross section	final	PLB 838 (2023) 137702
Drell–Yan cross section and nuclear effects	update	preliminary results released, paper project systematics, interest from theorists
Unpolarized asymmetries in J/ψ production	ongoing	study of systematic effects
J/ψ cross section ratio: Al/W (Drell-Yan 2018 data)	update	preliminary results released study of systematic effects
Beam PID analysis (CEDARs)	ongoing	neural network studies

2 General status of Primakoff and spectroscopy data analyses

2.1 Photon-pion interactions in peripheral pion-nucleus scattering

In 2009, we collected data using a pion beam and a Nickel target to investigate π^--photon scattering via the Primakoff processes. In these processes, the pion beam scatters off quasi-real photons originating from the Coulomb field of the nuclear target. Such processes lead to the production of final states such as $\pi^-\gamma$, $\pi^-\pi^0$, $\pi^-\pi^0\pi^0$, and others. Our current emphasis is on the $\pi^-\pi^0$ final state, which offers insights into the chiral anomaly and the $F_{3\pi}$ constant. Historically, the value of $F_{3\pi}$ was derived by measuring the cross-section of events near the kinematic threshold in $M_{\pi^-\pi^0}$, where the chiral anomaly's contribution is predominant. This method utilized only a fraction of the available data and had limited control over systematics arising from the tail of the $\rho(770)$ meson, resulting in a measurement accuracy of $F_{3\pi}$ at the 10% level. Our objective is to employ the dispersive approach proposed by Hoferichter *et al.* [5], which allows for the use of data up to $M_{\pi^-\pi^0} = 1\,\mathrm{GeV}/c^2$, encompassing the $\rho(770)$ resonance peak. This method not only promises a more precise measurement of $F_{3\pi}$ but also facilitates the measurement of the radiative coupling $\rho(770)^- \to \pi^-\gamma$ concurrently [6].

The $\pi^-\pi^0$ data sample is contaminated with background from diffractive $\pi^- + \mathrm{Ni} \to \pi^-\pi^0\pi^0 + \mathrm{Ni}$ events. To determine the number of Primakoff-signal events and distinguish them from this background, we generate a realistic $\pi^-\pi^0\pi^0$ Monte Carlo sample. This sample is grounded in the results of new a partial-wave analysis (PWA) of COMPASS $\pi^-\pi^0\pi^0$ data. We then process this Monte Carlo data through the full detector simulation and event selection pipeline. With the signal and background profiles derived from the simulation, we can fit the measured momentum transfer distribution in bins of $M_{\pi^-\pi^0}$, as depicted in Fig. 1a for one of the bins. This fits yield the count of Primakoff events in each bin, highlighted in red in Fig. 1b. When we fit the distribution within the dispersive framework, we obtain $F_{3\pi} = 10.3 \pm 0.1(\mathrm{stat}) \pm 0.6(\mathrm{syst})\mathrm{GeV}^{-3}$ and $\Gamma_{\rho\to\pi\gamma} = 76 \pm 1(\mathrm{stat})^{+10}_{-8}(\mathrm{syst})\mathrm{keV}$. The primary contributors to the systematic uncertainty include the luminosity determination using charged kaon decays into $\pi^-\pi^0$ and $\pi^-\pi^0\pi^0$. Additionally, the computation of the number of Primakoff events in bins of $M_{\pi^-\pi^0}$ also cases non-negligible systematic effects. We have also examined the potential effects of the material map descriptions in the Monte Carlo simulations.

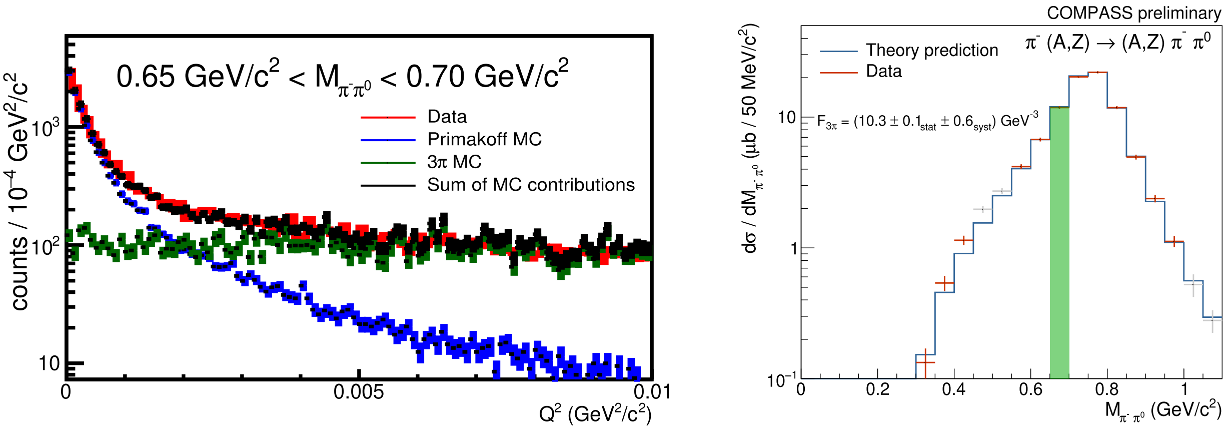

(a) (b)

Fig. 1: In (1a): distribution in squared four-momentum transfer Q^2 from the beam pion to the data for mass bin $0.65\,\mathrm{GeV}/c^2 < M_{\pi^-\pi^0} < 0.7\,\mathrm{GeV}/c^2$. The red histogram shows the measured distribution. The black histogram shows sum of the Primakoff-signal contribution (blue histogram) and the 3π background contributions (green histogram). The shape of both contributions is determined from simulated data based on the corresponding models. The yield of both distributions is determined from a fit the the measured Q^2 distribution. In (1b), two pion mass spectrum after the background subtraction is show in red. It is overlaid by the fit curve with the dispersive framework from [5] shown in blue. The mass bin shown in (1a) is highlighted in green.

The next step in our analysis is to minimize the systematic uncertainties, especially those affecting the value of $\Gamma_{\rho\to\pi\gamma}$. Improvements in the background modelling and better understanding of luminosity measurements will help to achieve that. Apart from the three-pion background already addressed, we're delving into potential background sources stemming from reactions where the target nucleous is excited. Following the upcoming publication on the 2009 Primakoff analysis, we plan to analyze an additional data set taken in 2012 to enhance our measurements of $F_{3\pi}$ and pion polarizabilities.

2.2 Results on diffractive pion and kaon dissociation

The COMPASS collaboration remains at the forefront of hadron spectroscopy, with a renewed emphasis on the diffractive production of kaons. This research is instrumental in enhancing our understanding of the light-meson spectrum and identifying supernumerary states. Our primary objective is the exploration of exotic states that enrich the conventional $q\bar{q}$ quark model. Notably, the decay channels $\omega\pi^-\pi^0$ and 3π are under rigorous analysis, with studies of the former by COMPASS being recently started. Concurrently, we are striving to complete the SU(3)$_{\text{flavor}}$ nonets and investigate the intrinsic $s\bar{s}$ content of isovector a_J and π_J states using $K^-K^0_S$ and $K^0_SK^0_S\pi^-$ final states.

Utilizing a $190\,\text{GeV}/c$ beam of pions and kaons impinging on a hydrogen target, COMPASS has collected an extensive dataset from diffractive dissociation reactions. These reactions enable studying excitations of the beam particle into transient intermediate resonances, X, which rapidly decay into a observable final-state hadrons. Two successful data taking years of 2008 and 2009 equipped the analysis team with an unprecedented sets of diffractive events of various topologies. The newly analysed dataset for the reaction $K^-\,p \to K^-\pi^-\pi^+\,p$ surpasses previous benchmarks, being 3.5 times larger than the prior largest sample. Our dataset for the $\pi^-\pi^0\omega(782)$ final state is fourfold that of the BNL E852 experiment. An updated analysis of the process $\pi^-\,p \to 3\pi\,p$ based on the full data set from 2008 and 2009, ncompassing over 100 million events, doubles the dataset of the previously published 3π analyses and underscores COMPASS's capabilities.

The partial wave analysis is the linchpin technique at COMPASS, facilitating decomposition of data and elucidating hadron interactions' dynamics. The robust two-step approach, consisting of an angular decomposion and a resonance model fit, is a robust tool for analyzing a variety of channels. For multi-body final states, such as 3π, $\omega\pi^-\pi^0$, and $K^-\pi^+\pi^-$, the isobar model becomes essential, postulating sequential two-body decays. The cross section is modeled as the squared magnitude of the coherent sum of decay and transition amplitudes, with the latter determined by fits to the observed kinematic distribution. For two-body final states, such as $\eta^{(\prime)}\pi$ and newly studied $K^0_{\text{S}}K^-$, ambiguities related to the partial-wave decomposition complexify the angular analysis. Understanding of these effect has been advanced recently in the group (see subsection 2.2.1 and in collaboration with theory colleagues [7].

Technological advancements in have been essential, with a shift from Geant3 to the Geant4-based framework for modeling detector effects. New implementation had offered a detailed simulation of the electromagnetic calorimeter needed for progress on studying reaction with neutral pions and photons. Innovations at COMPASS analysis technique also include the introduction of novel model-selection methodologies for the partial-wave decomposition of the $K^-\pi^-\pi^+$ sample (see subsection 2.2.6). The integration of Information Field Theory into the Partial-Wave Analysis, coupled with machine-learning tools (see subsection 2.2.4), might revolutionized our approach to partial wave analysis strategy. Preliminary, studies on simulated data have validated the efficacy of the new method.

2.2.1 *Studying ambiguities in the partial-wave decomposition of the K^-K_S final state*

In the diffractive-dissociation reaction $\pi^- + p \to K^0_{\text{S}}K^- + p$, the negative beam pion is excited to light-meson states which possess dominantly $J^{PC} = \text{even}^{++}$ quantum numbers. Additionally, the $K^0_{\text{S}}K^-$ final state has isospin $I = 1$ and no overall strangeness, which enables us to probe the intrinsic $s\bar{s}$ content of the isovector a_J states.

The $K^0_{\text{S}}K^-$ final state is a system of two pseudoscalar particles, known to be subject for appearance of mathematical ambiguities. Partial-wave decomposition models the observed cross-section as a squared linear combination of Legendre polynomials in the cosin of the scattering angle, with the coefficients being referred to as transition amplitudes of partial waves. In previous studies [8, 9], it was shown that such an expression can exhibit discrete ambiguities in the values of these waves. These ambiguities are associated with the unobserved overall phase of the amplitude. The highest total angular momentum of the wave included in the set determines the order of the polynomial in the tangent of the scattering angle. Conjugating the roots of the polynomial doesn't alter the squared expression, i.e. model intensity that is fitted to data, but it corresponds to a different set of transition amplitudes.

We've undertaken studies to deepen our grasp of the phenomenon and devise strategies to address it [10]. Initially, we crafted a model for the partial-wave amplitudes that closely mirrors physical amplitudes – continuous across an extensive two-body mass range and exhibiting resonant-like signals. Leveraging this model, we derived the complete set of ambiguous solutions for the partial-wave amplitudes. This allowed us to discern their shape, continuity, and differentiate them from the physical model. Our observations revealed that these ambiguities can yield amplitude distributions markedly deviating from the initial model. Such deviations might enable us to filter out "unphysical" solutions, especially if resonant-like structures emerge at unexpected masses. In addition, we noted that the amplitude of the highest-spin partial wave remains the same for all ambiguity classes. Subsequently, we generated Monte Carlo data based on the amplitude model and executed a partial-wave decomposition of this data. This was aimed at exploring a scenario where partial-wave amplitudes are inferred from finite data sets. The decomposition outcomes largely align with the computed solutions, though statistical variations do emerge, affecting aspects like the number of solutions discerned by the decomposition.

In the case of the $K^0_\mathrm{S}K^-$ system, we've pinpointed a method that effectively curtails the ambiguities. By excluding the partial waves with an odd spin—which are anticipated to be suppressed—from the partial-wave model, the ambiguous solutions are essentially eradicated. This verification facilitates the differentiation between the physical and ambiguous solutions within the complete wave set.

2.2.2 Technical advances for the $3\pi\gamma\gamma$ final state and beyond

Over the past year, we've been transitioning to a new detector description based on Geant4. This shift brings numerous enhancements, notably a fine-detail modelling of the electromagnetic calorimeter, a feature absent in the previously utilized GEANT3 framework. The TGEANT framework, originally designed for simulating data structure program of COMPASS experiment, required significant updates to cater to the experimental setup of the spectroscopy program. We've incorporated a description of the hydrogen target, integrated elements of the hadron trigger, and made substantial improvements to the recoil proton detector's implementation. The electromagnetic calorimeter module, of the shashlik type, has been detailed further to align with observed event characteristics. This updated module showcases spiraling scintillating fibers and a layered lead-scintillator structure. Impressively, despite these intricate details, we've managed to maintain minimal run time per event, thanks to discovered optimizations.

Currently, a large-scale Monte Carlo production with TGEANT is underway, which will be pivotal for the partial wave analysis of the $\eta\pi$, $f_1\pi$, and $K_sK_s\pi$ final states [11]. This revamped description has been instrumental in identify specific artifacts in the hadron data, linking them to features in the detector design. For example, long term mystery of efficiency drop in the recoil proton distribution is finally explained by calibration connectors mounted to the scintillator slabs of the recoil proton detector.

Beyond the Monte Carlo description, strides have been made in refining the calibration and selection processes, particularly concerning the recoil proton detector. We've improved the time calibration of the photomultipliers by utilizing elastic scattering events. By reconstructing the scattered pion with the COMPASS spectrometer, we've been able to gauge the measurements of the recoil proton detector against it. This method has enabled us to derive run-dependent calibrations with remarkable precision. As a result, our analysis can now accommodate events with multiple reconstructed recoil proton tracks, provided all but one are outside the geometrical acceptance of the recoil proton slabs. As the result, we increased the signal efficiency and purity for events with a observed proton track, leading to an approximate 10% surge in selected events for the $\eta\pi^-$ final state.

Moreover, we performed a new reconstruction of the raw data from the years 2008 and 2009. One of the major improvements of this new data production is an updated calibration of the ECAL energy reconstruction. This yielded a better time stability of the ECAL performance as well as an enhanced energy resolution. The analysis of the $\pi^-K^0_\mathrm{S}K^0_\mathrm{S}$ final state (see section 2.2.3) is the first analysis that is based on the new data production. Furthermore, especially, upcoming analysis of final states such as $3\pi\gamma\gamma$ will significantly profit from the improved ECAL resolution.

2.2.3 $\pi^-K^0_S K^0_S$ final state

The $\pi^-K^0_\mathrm{S}K^0_\mathrm{S}$ final state contains information on the a_J and π_J resonances similar to the $\pi^-\pi^-\pi^+$ final state. However, the production threshold is higher, which gives enhanced access to higher radial excitations, while the ground states are kinematically suppressed. Besides of ordinary mesons, the enigmatic $a_1(1420)$ signal [12] interpreted as a rescattering effect [13] is expected to show up, as well as the spin-exotic hybrid candidate, the $\pi_1(1600)$ in the predicted but yet unobserved $K^*\bar{K}$ decay channel. Additionally, the involved two-body resonances (isobars) are different to those seen in the 3π analysis [14], allowing one to study $s\bar{s}$ coupling of the π_J and a_J states. The event selection of diffractively produced $\pi^- K^0_S K^0_S$ systems resulted in $\sim 240\,000$ candidates. To reduce background contributions from the 5π final states, a significance study on the optimal separation of the decay vertex $K^0_S \to \pi^+\pi^-$ of the comparably long-lived K^0_S to the production vertex was performed. A kinematic fit of the track momenta using the known K^0_S mass as constraint has been employed to improve experimental resolution.

The invariant-mass spectrum of the $(K^0_S K^0_S)$ system (Fig. 2a) indicates an increased intensity at threshold corresponding to the $f_0(980)$ isobar, and at $\sim$ 1.3 GeV/c^2 due to the $f_2(1270)$. Another peak shows up at $\sim$ 1.5 GeV/c^2 where the $f_0(1500)$ and the $f_2'(1525)$ are expected, as well as a shoulder at higher masses hinting to the presence of the $f_0(1710)$. As for the $\pi^-\pi^-\pi^+$ final state at COMPASS, no structure for $f_0(1370)$ is seen. In the $(\pi^- K_S)$ subsystem (Fig. 2b), the $K^*(892)$ dominates the distribution as a narrow peak at its nominal mass. One finds an enhancement in the corresponding invariant-mass spectrum at $\sim$ 1.4 GeV/c^2 where the $K^*(1410)$, the $K_0^*(1430)$ and the $K_2^*(1430)$ are expected. The full three-body invariant-mass spectrum (Fig. 2c) has a broad peak at 1.75 GeV/c^2 and a shoulder at 2.1 GeV/c^2. However, as many resonances contribute there, definite conclusion awaits for completion of the partial-wave analysis. Nonetheless, we observe in the three-body invariant mass region at about 1.8 GeV/c^2 already indications for the presence of the decay channel $\pi(1800) \to f_0(980)\pi^-$, a candidate for a hybrid meson. We also see a significant intensity at the locations of the previously mentioned $a_1(1420)$ and the $\pi_1(1600)$.

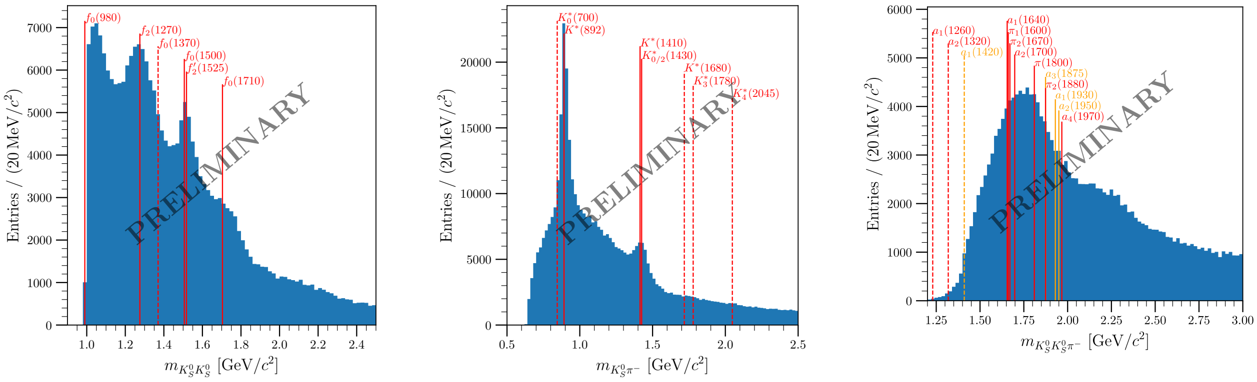

(a) (b) (c)

Fig. 2: Invariant-mass spectra of the isobar subsystems $(K^0_S K^0_S)$ (2a) and $(\pi^- K_S)$ (2b) and invariant-mass spectrum of the $(\pi^- K^0_S K^0_S)$ final state (2c). Red vertical lines correspond to states that are established according to the Particle Data Group, orange lines correspond to states that need further confirmation. Dashed lines indicate the absence of a clear signal of this state in our data.

2.2.4 3π final state

The combined dataset from the 2008 and 2009 data-taking periods for the process $\pi^- p \to \pi^-\pi^-\pi^+ p$ contains over 100 million events, making it the most extensive set available for studying light mesons. For a set of this size, the primary source of uncertainties in the analysis are systematic. A significant systematic challenge arises from the partial-wave model used to decompose the observed data distribution. The high precision of our data requires us to model also small signal. Hence, the analysis has to deal with a large pool of waves in order to include all partial-waves that potentially could contribute to our data. This vastness can lead to overfitting due to an excess of parameters.

Previous studies [15–19] have employed regularization techniques to manage this expansive wave set. In these methods, the log-likelihood function is augmented with a regularization term that penalize intensity for every wave. While this technique improves results, it sometimes yields discontinuities of the wave intensity between neighbour bins, contradicting our expectation for a consistent physical signal.

Our objective is to more directly integrate our comprehensive prior knowledge into the analysis. Collaborating with peers from the Excellence Cluster Origins and the Max-Planck Institute for Astrophysics, we've redefined the partial-wave analysis within the context of information field theory [10]. We've executed this analysis using the NIFTy package [20–23]. This innovative, non-parametric model for partial waves not only ensures bin-to-bin continuity but also provides regularization, pushing minor waves towards zero. A notable feature of this method is its requirement to fit data across all bins simultaneously. This simultaneous fitting has become feasible thanks to the significant acceleration of the partial wave implementation, achieved through machine learning tools.

We have performed studies on simulated data that demonstrate the feasibility and effectiveness of this new method. By making use of the additional continuity information, we have been able to recover the known input of the simulated data. Our tests on simulated data underscore the potential and efficiency of this novel approach. This method addresses the limitations of the binned approach, which stem from inherent discontinuity of individual bins. As a result, we can diminish the systematic uncertainty tied to the selection of the partial-wave model. We're currently applying this new technique to real data and have initiated preliminary efforts to extend its use to other final states.

2.2.5 $\pi^-\pi^0\omega(782)$ *final state*

The $\pi^-\pi^0\omega(782)$ final state is of particular interest because it provides insight into $b_1\pi$, which is predicted to exhibit the highest branching fraction of the spin-exotic $\pi_1(1600)$ [24]. Notably, past experiments have seen the $\pi_1(1600)$ in this decay mode. The most sophisticated analysis of the BNL E852 experiment dates roughly two decades ago. The analysis asserts the presence of not only the $\pi_1(1600)$ but also the $\pi_1(2015)$, which however, warrants further verification [25]. The COMPASS dataset for $\pi^-\pi^0\omega(782)$, produced through diffractive scattering, comprises approximately 720,000 events. This is over four times the number of events recorded by E852.

We have undertaken a partial-wave analysis of the $\pi^-\pi^0\omega(782)$ final state [26]. The first stage of this analysis, the angular decomposition, has been recently completed. It's noteworthy that $\pi^-\pi^0\omega(782)$ isn't a stable final state. The $\omega(782)$ predominantly decays to $\pi^-\pi^0\pi^+$, resulting in a 5-body final state. The decay amplitude of $X^- \to \pi^-\pi^0\omega(782)$ is modelled using the isobar model. For the decay $\omega(782) \to \pi^-\pi^0\pi^+$, we employed an effective description, grounded in the decay via P-wave and a Dalitz-plot modulation, as experimentally measured by BES-III [27]. Consequently, our decomposition leverages the full high-dimensional phase-space information. By considering partial waves up to a total spin $J = 8$ and decays via various channels, we incorporated a total of 893 partial waves in this analysis. Applied advanced wave-selection techniques benefits from our previous analyses of $K^-\pi^-\pi^+$ (see Sec. 2.2.6 and Ref. [19]) and $\pi^-\pi^-\pi^+$ (see Sec. 2.2.4) helped finding relevant contributions and stabilize the fit.

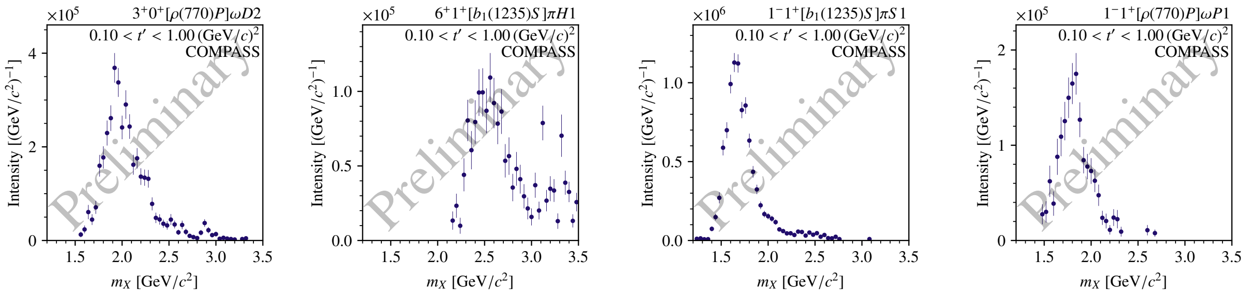

(a) (b) (c) (d)

Fig. 3: Intensities of selected partial waves as a function of the invariant mass of the $\omega\pi^-\pi^0$ system. The corresponding wave is denoted at each plot in the top-right corner.

In the decomposed waves we observe clear resonance-like signals for established states like the $a_4(1970)$, $\pi(1800)$, and $a_2(1320)$. Additionally, we detected signals in less explored J^{PC} sectors, where all observed states warrant further verification. Figure 3a shows the intensity of a $\rho(770)\omega$ wave in the $J^{PC} = 3^{++}$ sector. The distribution shows a clear peak around 2.0 GeV$/c^2$ suggesting an a_3 state at this mass. Figure 3b shows the intensity of the $b_1(1235)\pi$ wave in the $J^{PC} = 6^{++}$ sector. We observe a signal at 2.5 GeV$/c^2$ which agrees well with the $a_6(2450)$ state only seen by one experiment in the $K_S K$ final state [28].

In the intriguing spin-exotic 1^{-+} sector, we discerned a distinct resonance-like signal for $\pi_1(1600)$ in the $b_1(1235)\pi$ channel as shown in Figure 3c. However, there's no evident hint of an excited π_1 in $b_1(1235)\pi$, such as the $\pi_1(2015)$ claimed by BNL E852. Furthermore, we observed a resonance-like structure for $\rho(770)\omega$ waves in the 1^{-+} sector around 1.8 GeV$/c^2$, shown in Fig. 3d. Whether this structure is consistent with $\pi(1600)$ is currently under study.

Our ongoing resonance-model fit of $\pi^-\pi^0\omega(782)$ has shown promising preliminary results.

2.2.6 Diffractive kaon dissociation into the $K^-\pi^-\pi^+$ final state

To deepen our understanding of the light-meson spectrum and identify supernumerary states, it's crucial to complete the SU(3)$_{\text{flavor}}$ nonets, including the strange counterparts of non-strange light mesons. The spectrum of strange mesons remains less explored than that of non-strange light mesons [29].

At COMPASS, we study excited strange mesons in the diffractive dissociation reaction $K^- p \to K^-\pi^-\pi^+ p$ using the 2.4% K^- component in the 190 GeV$/c$ negative hadron beam [19, 30]. This effort yielded a dataset of approximately 720 000 exclusive $K^-\pi^-\pi^+$ events, making it the world's largest sample for this reaction This is currently the world's largest sample of this reaction. It surpasses the previous largest sample from the CERN WA03 experiment by 3.5 times [31].

Based on this $K^-\pi^-\pi^+$ sample, we performed a comprehensive partial-wave analysis going beyond what was done before in the strange-meson sector [32]. First, we performed a partial-wave decomposition were we inferred the model from data using novel model-selection techniques pioneered at COMPASS [19]. Then, we performed a resonance-model fit, where we modeled the measured partial-wave amplitudes of 14 selected waves in terms of strange-meson resonances and additional background components. We also conducted systematic studies, in order to refine our analysis and determine uncertainties on the measured masses and widths of the studied strange mesons.

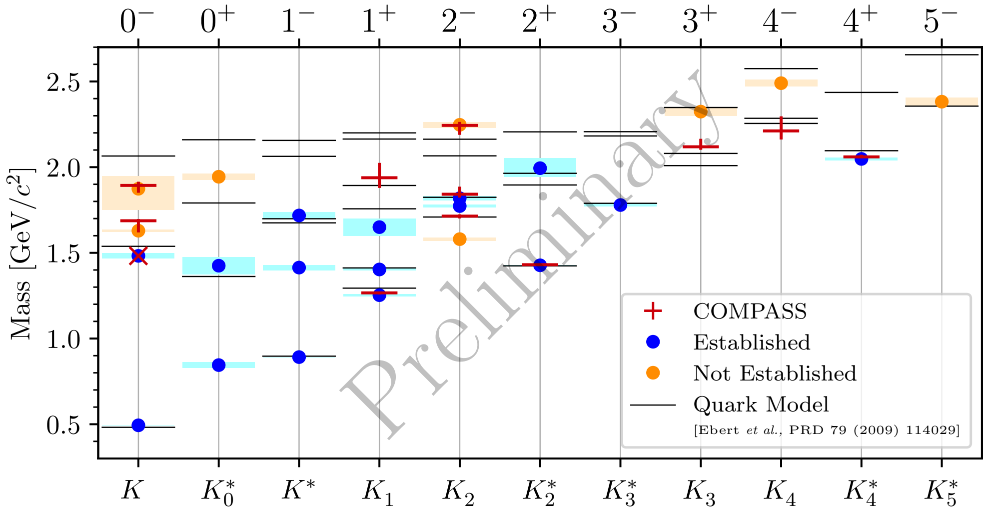

Fig. 4: Spectrum of strange mesons, i.e. nominal masses of strange mesons grouped by their J^P quantum numbers. The red pluses represented our measured mass values. The horizontal line of each plus gives the mass as obtained in the main analysis. The vertical line of each plus gives the corresponding total uncertainty, i.e. the quadratically added statistical and asymmetric systematic uncertainty. The blue data points show the masses of established states, the orange data points those of not established states as listed by the PDG [29]. The similarly colored boxes represent the corresponding uncertainties. The black horizontal lines show the masses of states as predicted by the quark-model calculation in ref. [33].

Our analysis faced challenges related to the particle identification of kaons that doesn't span the entire momentum range, leading to: (i) There is a non-negligible background of about 10 % in the $K^-\pi^-\pi^+$ sample from other diffractive reactions such as $\pi^- p \to \pi^-\pi^-\pi^+ p$. We developed an approach to handle these incoherent backgrounds by effectively taking them into account in the partial-wave decomposition and then explicitly modeling them in the resonance-model fit. In this way, these backgrounds can be separated from strange-meson signals at the level of the resonance-model fit. For the dominant background from the reaction $\pi^- p \to \pi^-\pi^-\pi^+ p$, we developed a model based on the high-precision results from our COMPASS $\pi^-\pi^-\pi^+$ analysis [34]. (ii) There are regions in the $K^-\pi^-\pi^+$ phase-space with practically zero experimental acceptance. These blind spots lead to a reduced distinguishability among certain partial waves, which causes analysis artifacts in these waves. Consequently, the affected waves cannot be interpreted in terms of physics signals. However, we were able to proof in various systematic studies as well as Monte Carlo input-output studies that only a subset of waves is affected by these analysis artifacts and that the other waves can still be used to study strange meson.

Navigating the challenges, we finalized the first strange meson analysis in COMPASS and the most comprehensive study of the $K^-\pi^-\pi^+$ final state, so far. The studies led to the measurement the masses and widths of 11 strange mesons from almost all J^P sectors and from a wide mass range as shown by the red pluses in Fig. 4. In this way, we obtained the so far most complete picture of the strange-meson spectrum coming from a single analysis. We observe signals of well-known states such as the $K_1(1270)$ or the $K_4^*(2045)$ in agreement with previous observations. Also, we observe for the first time the high-mass states $K_2(2250)$, $K_3(2320)$, and $K_4(2500)$ in a final-state different from $\Lambda\bar{p}$ in a partial-wave analysis. Our uncertainties for most of the measured masses and widths are competitive with previous measurements of these parameters. In the $J^P = 0^-$ sector, we find evidence for three excited pseudoscalar states, while quark-model calculations predict only two states in this mass region (cf. red pluses and cross and black horizontal lines in Fig. 4). This indicates that one of these states is a supernumerary state in addition to the conventional $q\bar{q}$ states. According to their masses, the $K(1630)$ is the best candidate for this exotic strange meson. This would be the first observation of an exotic state in the strange-meson sector (except for the κ / $K(700)$). As a final step, we are aiming to publish these results in a journal paper.

3 General status of 2016–2017 data analyses

During 2022-2023 we reached a significant progress in finalization of several key analyses based on 2016 data. The data has been re-processed with an improved detector alignment and updated calibrations for electromagnetic calorimeters. On Monte-Carlo side, several adjustments have been made to the event generators (HEPGen++, DJANGOH), which lead to improvements in the exclusive analyses (π^0, DVCS) and in the description of radiative processes (evaluation of radiative corrections). In the meantime, we are applying established analysis frameworks to the 2017 data. Currently we are scrutinizing the stability of detector planes and alignment reliability for all data-taking periods of 2017 evaluating the pseudo-efficiencies of all detector planes. The final calibrations for electromagnetic calorimeters and RICH are being prepared and tested. The advances and prospects for various analyses are detailed in the next sections.

3.1 Multiplicity of hadrons produced in DIS off LH target (2016 data)

Hadron multiplicities are defined as the number of hadrons produced per DIS event and the analysis is performed in bins of x, y and z:

$$\frac{dM^h(x,y,z)}{dz} = \frac{1}{N^{DIS}_{events}(x,y)} \frac{dN^{DIS}_h(x,y,z)}{dz}\,, \tag{1}$$

where N^{DIS}_{events} is the number of DIS events and N^{DIS}_h the number of hadrons. Several corrections have to be applied to the data in order to obtain final multiplicities: acceptance corrections A, radiative corrections RC and removal of decay products of diffractively produced vector meson VM_{corr}

$$\frac{M^h(x,y,z)}{dz} = M^h_{raw}(x,y,z)/dz \frac{VM_{corr}(x,y,z)RC(x,y,z)}{A(x,y,z)}\,. \tag{2}$$

With the same method, multiplicities of identified hadrons, namely pions and kaons, are obtained. Here, $N^{DIS}_{\pi,K}$ is the number of pions/kaons obtained after RICH PID unfolding. The RICH unfolding is performed using the standard COMPASS method (see Ref. [35] and references therein).

One of the interesting quantities is the sum of charged multiplicities integrated over z and averaged over y, which to a very good approximation is equal to the sum of favoured and unfavoured fragmentation functions. As these do not directly depend upon x, the value of

$$\mathcal{M}^h(x) = \left\langle \int\limits_{z=0.2}^{z=0.85} \left(\frac{M^{h^+}(x,y,z)}{dz} + \frac{M^{h^-}(x,y,z)}{dz} \right) dz \right\rangle_y \tag{3}$$

should be rather flat as a function of x, as it was observed when analysing the COMPASS data from a ^{6}LiD target [35]. In the case of $\mathcal{M}^K(x)$, low x events are sensitive to the contribution from the strange quark fragmentation function multiplied by the strange quark parton distribution function (PDF). At high x, since the strange PDF is small, we expect the result to correspond to the sum of favoured and unfavoured fragmentation functions as in the case of π and h.

The SIDIS events were recorded along with the DCVS data during 2016/2017 data taking using a liquid hydrogen target and 160 GeV/c μ^+ and μ^- beams. The analysis currently focusses on data from the second half of 2016, as the spectrometer, especially the RICH detector for kaon and pion identification, was more stable during this time than in the beginning of the year.

As reported previously a final step was missing before the multiplicity analysis in bins of z, x and y could be concluded. The updated MC generator, which includes radiative processes, DJANGOH [36] had to be re-integrated into the COMPASS full Monte Carlo chain. The obtained MC simulated SIDIS events were compared in detail to real data. Examples for the comparison illustrate the good agreement between data and MC. Figure 5 (left) shows the fraction of events with and without any other charged particle detected except of incoming and outgoing muons, Fig. 5 (right) the p_T^2 distribution for charged particles with respect to the virtual photon for events with more than two additional charged particles reconstructed in the spectrometer besides incoming and outgoing muons. Here, the radiative peak stems from photons, which converted to electron-positron pairs.

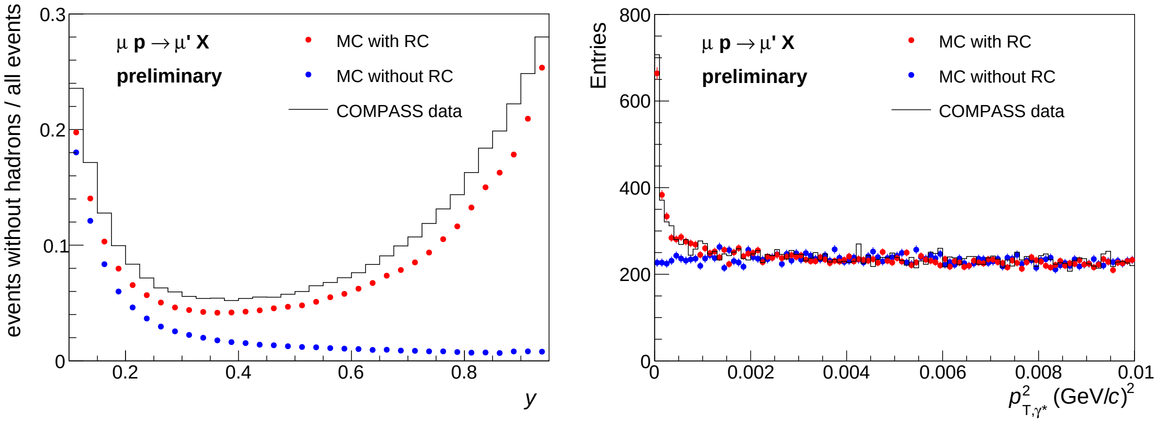

Fig. 5: Left: fraction of events with and without any other charged particle detected besides incoming and outgoing muons, right: p_T^2 distribution for charged particles with respect to the virtual photon for events with more than two additional charged particles reconstructed in the spectrometer in addition to incoming and outgoing muon.

Comparing the size of the newly obtained radiative corrections to the ones used previously for SIDIS events, we find that they differ up to 15% at high y and high z. Note that the previous method of obtaining RC for SIDIS events was also used in SMC and NMC experiments, and these corrections are part of the so-called dilution factor in COMPASS and SMC experiments. In general, these advances in the simulation and estimation of the radiative effects impact several other analyses including transverse-momentum-dependent (TMD) effects (azimuthal asymmetries, TMD multiplicities and P_T distributions).

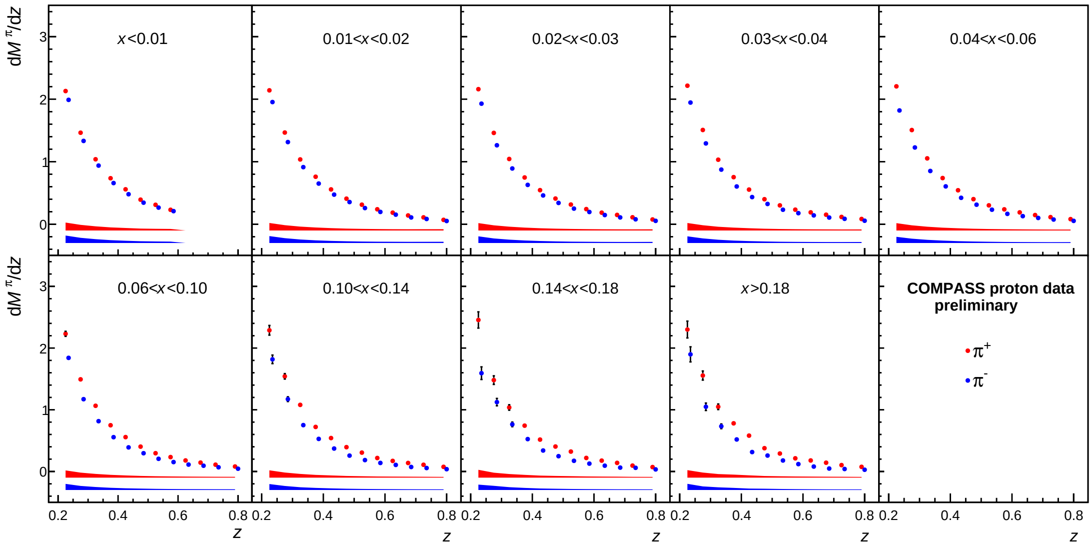

Fig. 6: Multiplicities dM^π/dz in bins of x and z, averaged over y.

In addition to the implementation of the new radiative corrections, the analysis of multiplicities of charged π, K and h was updated using new productions of data and MC. With better data and MC quality it was easier to disentangle other systematic effects. For example, one of the triggers had to be removed from the analysis (LAST trigger timing instabilities) and the phase space was reduced due to a problem observed with the RICH detector.

Results for multiplicities from the 2016 data were released in September 2023 and were already shown on recent conferences [37]. In Fig. 6 the z dependence for the π^+ (red) and π^- (blue) multiplicities is shown in nine bins of x, averaged over y. The same is shown in Fig. 7 for kaons. The multiplicities show the expected strong dependence on z with the results for positive particles larger than for negative ones, especially at larger x. These results complement our deuteron results published in [35], [38].

The sum of multiplicities integrated over z and averaged over y (see eq. 3) should agree within 1% with

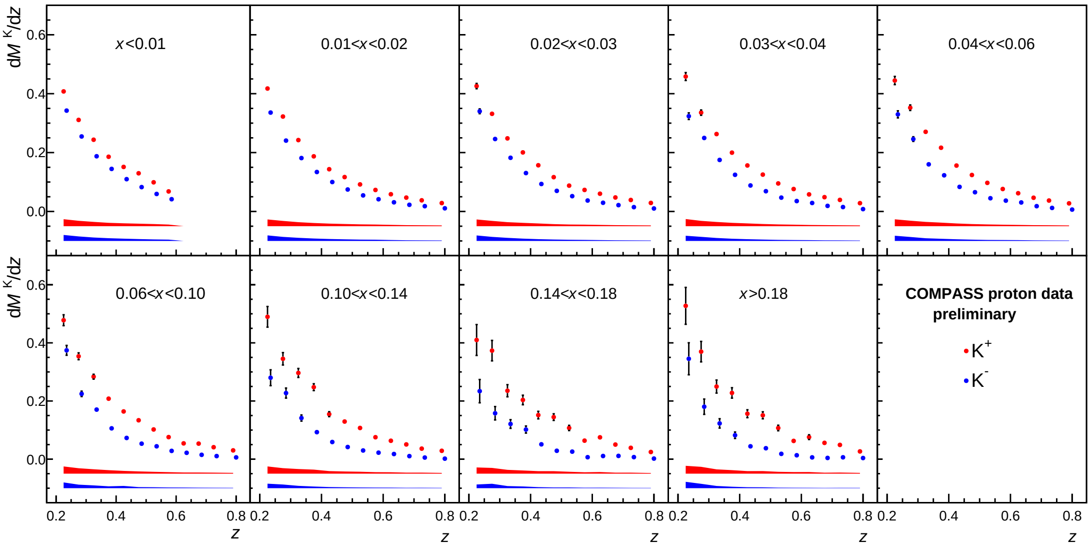

Fig. 7: Multiplicities dM^K/dz in bins of x and z, averaged over y.

the results for the deuteron target. However, the difference between the new results and the published ones

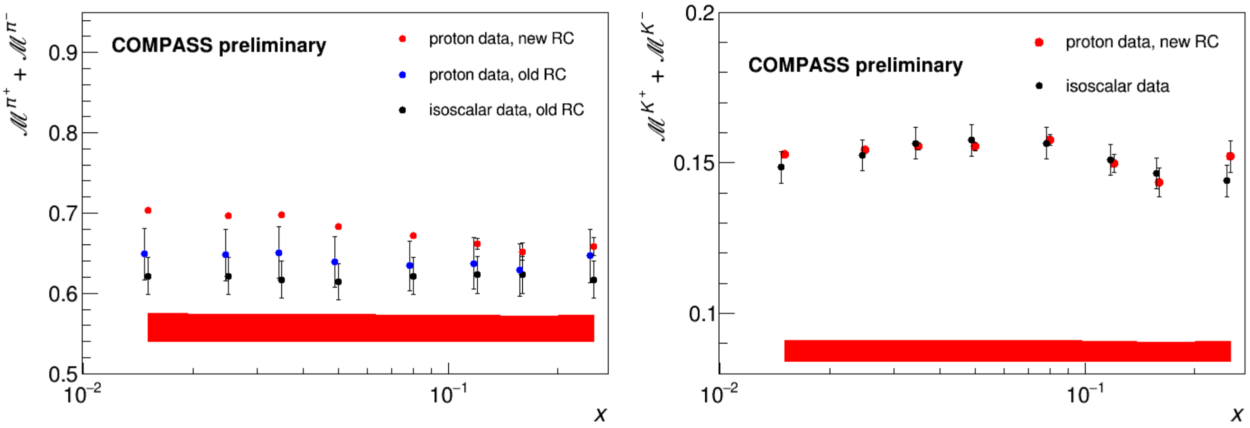

Fig. 8: Left: Values of $\mathcal{M}^{\pi^+} + \mathcal{M}^{\pi^-}$ as a function of Bjorken x with statistical uncertainties. The comparison of the present results with new or old radiative correction is shown, as well as the COMPASS deuteron results published in [35]. Right: Values of $\mathcal{M}^{K^+} + \mathcal{M}^{K^-}$ as a function of Bjorken x with statistical uncertainties. The Comparison of the present results with COMPASS deuteron results published in [38] is shown. Note that for deuteron data and proton data with old RC the systematic and statistical uncertainties combined are shown.

for pions is sometimes larger than 10 %. The main culprit for the difference is the effect of the new radiative corrections using DJANGOH, which especially impact results at low values of x. For kaons the agreement is much better, due to the fact that a rough estimate of the new radiative corrections was applied to the data.

It is interesting to note that, according to LO pQCD, for hadrons and pions the sum of multiplicities of two charges is expected to be rather flat in x and this was observed for the previously published data [35]. In the present data, a clear x dependence is visible.

3.2 Transverse momentum structure of the nucleon from unpolarized SIDIS measurements

The COMPASS analyses aiming to study the transverse momentum dependent (TMD) phenomena in unpolarized SIDIS benefited from the improvements in 2016 SIDIS data analyses quoted in the previous sections and exclusive analyses quoted in Sec. 3.3. In particular, the advances made for description of radiative effects in Monte Carlo and evaluation of radiative corrections, have been applied to the unpolarized SIDIS asymmetries analysis and are currently being applied to the TMD multiplicities (P_T distributions) studies.

In next sections the progresses in TMD studies with unpolarized SIDIS measurements are summarised. In some cases, our strategy is to finalise ongoing studies in parallel with the same measurement performed using recent COMPASS SIDIS data collected in 2022 with transversely polarized deuteron target. In particular, this is the case for the exploratory study of the unpolarized dihadron asymmetries, performed in 2022, and described in last year's report [39]. This work was temporarily suspended focusing on other priority topics. The analysis will be resumed in near future, and performed in parallel for 2016 proton and 2022 deuteron data.

3.2.1 Azimuthal asymmetries

The azimuthal modulations (asymmetries) of hadrons produced in DIS are an important probe to study the partonic TMD structure of the nucleon. For unpolarised target and longitudinally polarised beam the SIDIS cross-section contains three asymmetries [40]:

- $A_{\mathrm{UU}}^{\cos\phi_h}$ has a complicated structure function, which includes a mix of twist-2 and twist-3 PDFs and FFs. The asymmetry is expected to be sensitive to the intrinsic quark transverse momentum $\langle k_T^2\rangle$ via the Cahn effect. The term is suppressed by a factor of Q^-1;
- $A_{\mathrm{UU}}^{\cos 2\phi_h}$ can be attributed to the Boer–Mulders TMD PDF coupled to the Collins fragmentation function, but it is also expected to get a contribution from the Cahn effect, though at higher orders;
- $A_{\mathrm{LU}}^{\sin\phi_h}$ is induced by quark-gluon correlations and higher-twist effects. The term is suppressed by a factor of Q^-1

So far, COMPASS published unpolarized SIDIS asymmetry results only with the isoscalar ^{6}LiD (deuteron) target [41]. The extraction was performed from the transversely polarised data collected in 2004, properly mixing the events with different polarizations (in order to cancel the spin effects and obtain an "upolarised" sample). The azimuthal asymmetries for charged hadrons have been extracted both in one-dimensional bins of x, or z, or P_T integrating over other variables ("1D results"), and in a three-dimensional grid over x, z and P_T ("3D results") [41]. Similar analysis was then initiated for the proton asymmetries using the SIDIS data collected with unpolarized liquid hydrogen (LH) target in 2016 and 2017. In 2019, while carefully studying the impact of diffractively-produced vector mesons on the proton 2016 asymmetries, corresponding analysis has been carried out also for the deuteron case. The "exclusive hadrons" – charged hadrons coming for the decay of diffractively-produced vector mesons[1] (VM), are characterised by large azimuthal asymmetries and constitute a non-negligible fraction of the final hadron sample in some kinematic regions. Their contribution to the measured 3D azimuthal asymmetries was evaluated for both proton 2016 and deuteron 2004 data and the exclusive-hadron-subtracted deuteron asymmetries were published [42].

At that time, the 1D exclusive-hadron-subtracted deuteron asymmetries were not included in the publication because of larger systematic uncertainties. However, with recent studies aiming to use both proton and deuteron data to perform point-by-point extraction of the Boer-Mulders TMD PDF [43], the exclusive-hadron-subtracted azimuthal asymmetries were re-evaluated also for the 1D-case and released in May 2023.

The original and the exclusive-hadron-subtracted $A_{\mathrm{UU}}^{\cos\phi_h}$ and $A_{\mathrm{UU}}^{\cos 2\phi_h}$ asymmetries are compared in Figs. 9 and 10, respectively.

Similar to the proton case, the $A_{\mathrm{UU}}^{\cos\phi_h}$ asymmetries differ significantly from the uncorrected ones in z bins only, while for the $A_{\mathrm{UU}}^{\cos 2\phi_h}$ the differences are visible nearly in all kinematic bins. The error bars in the figures show the statistical uncertainties. The systematic ones are a factor of 2.4 to 4 larger.

Very likely, these are the last results from the "old" deuteron data collected in 2002-2004 and 2006. Several studies are planned, when a refined Monte Carlo for the 2022 deuteron data is available. In particular, with the new data we plan to perform all measurements that are currently being done for 2016 proton sample, but with an enlarged kinematic coverage, thanks to the larger acceptance of the COMPASS spectrometer in 2022.

The first preliminary results for the unpolarised asymmetries from a fraction of 2016 data collected with LH target and $\mu^{\pm}$ beam were obtained in 2018 and later updated with more statistics, better Monte Carlo description of the apparatus and studying additional kinematic dependences (in particular on Q^2). These results appeared e.g. in the 2021 report [44] and were presented at various conferences [45, 46].

This year the analysis was extended to the rest of the 2016 data including more data taking periods (about a factor of 2 more data than previously) reconstructed with a better alignment and corrected calibrations. In addition improved and larger Monte Carlo sample was produced for acceptance corrections, with period-dependent

---

[1] mainly ρ^0 and ϕ

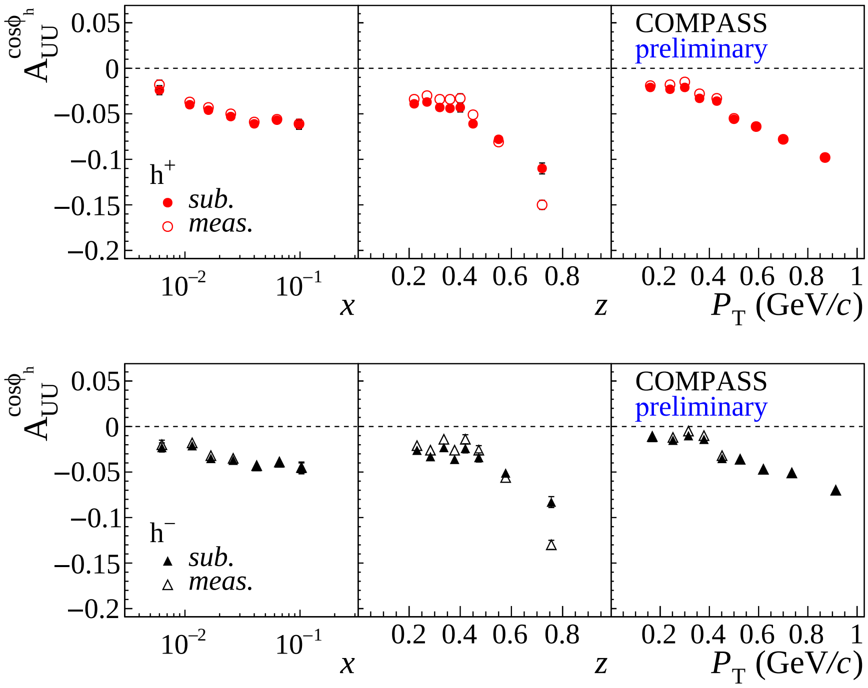

Fig. 9: Top: the subtracted $A_{UU}^{\cos\phi_h}$ asymmetry for h^+ as a function of x, z and P_T (closed points) compared to the published asymmetry (open points). Bottom: the corresponding comparison for h^-.

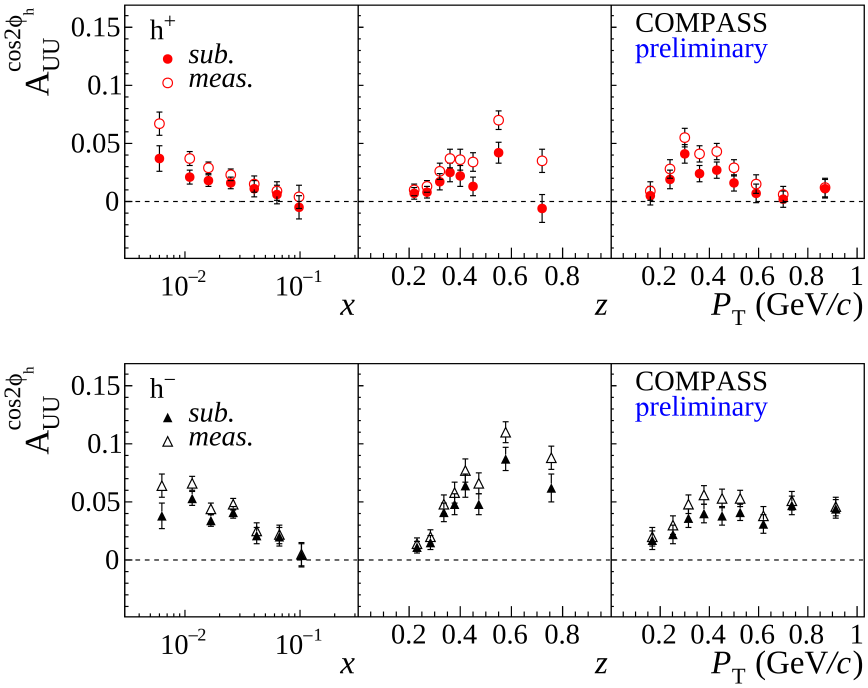

Fig. 10: Top: the subtracted $A_{UU}^{\cos 2\phi_h}$ asymmetry for h^+ as a function of x, z and P_T (closed points) compared to the published asymmetry (open points). Bottom: the corresponding comparison for h^-.

detector and trigger efficiencies. Unfortunately, these improvements did not solve the discrepancies observed for the $\cos\phi_h$-amplitudes as a function of the primary vertex position, which was mentioned in our previous reports. For the moment, these discrepancies are being accounted for at the level of systematic uncertainties. In general, increasing the size of the data sample and new MC did not change the results qualitatively as can be seen in Fig. 11 where the old and new results are compared.

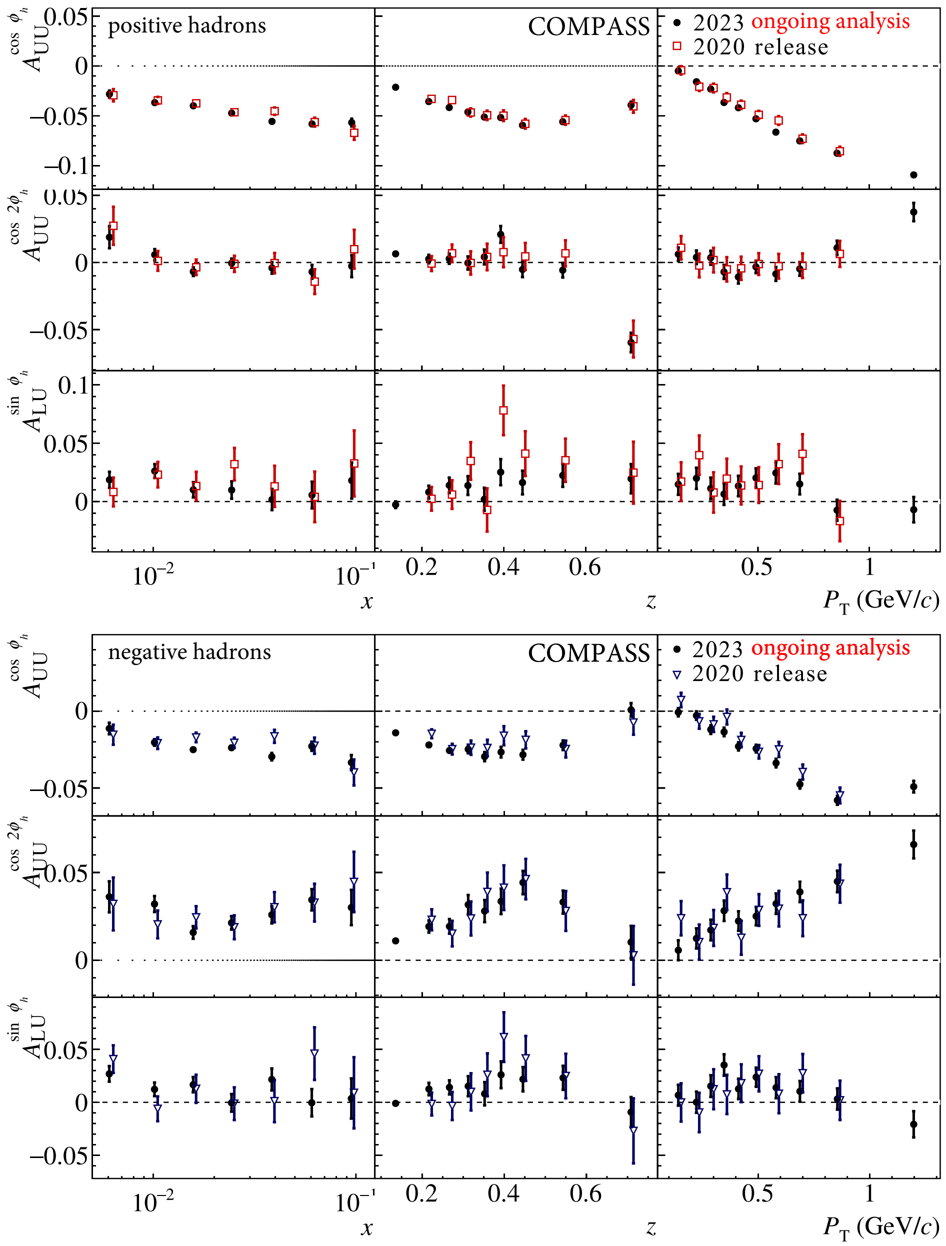

Fig. 11: The azimuthal asymmetries for h^+ and h^- from the ongoing analysis described in this report compared to the previously released results. The differences are small (radiative corrections are not applied here).

One of the most important updates introduced recently in the analysis of SIDIS asymmetries with proton 2016 data has been the evaluation of the impact of QED radiative effects. They are important for the correct interpretation of the asymmetries, as they can be expressed in terms of TMD PDFs and fragmentation functions thanks to factorisation, which is defined at tree (Born) level. Radiation of real photons by the incoming and outgoing muons biases the experimentally measured x and Q^2 values w.r.t. to those that characterised the actual hard scattering process at parton level. Moreover, the muon momenta define the gamma–nucleon system in which the angle ϕ_h and the transverse momentum P_T are defined, so the radiation of photons affects also those quantities.

We obtain the radiative corrections from the DJANGOH MC generator [36, 47], which simulates the radiative effects in the lepton scattering and generates final state hadrons via Lund fragmentation model (based on LEPTO). The generator was adapted for the use at COMPASS, tuned to be consistent with the previously used analytical inclusive correction and thoroughly tested. The Cahn effect was implemented into the generator and found to have negligible impact on the radiative corrections. Two examples of data-to-MC comparisons shown in Fig. 12 and 13 illustrate that the radiative effects are well described by the MC. Further details on

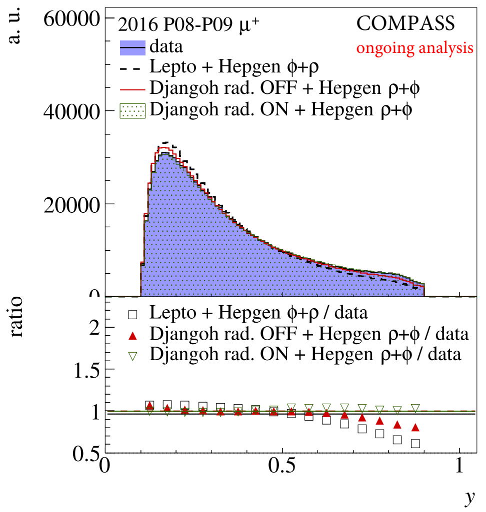

Fig. 12: The y distribution for DIS events compared in real data and different MC samples: LEPTO and DJANGOH with radiative effects off and on. The latter reproduces the shape in the data.

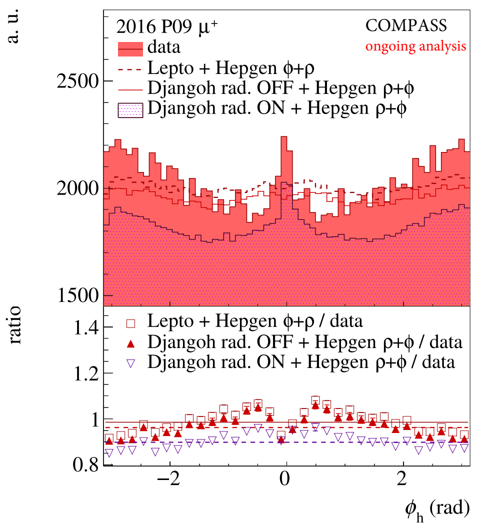

Fig. 13: The ϕ_h distribution for h^+ compared in real data and MCs. The peak at $\phi_h = 0$ is caused by e^+ (miss-identified as hadrons) coming from conversion of real photons radiated by the muons. DJANGOH reproduces the effect.

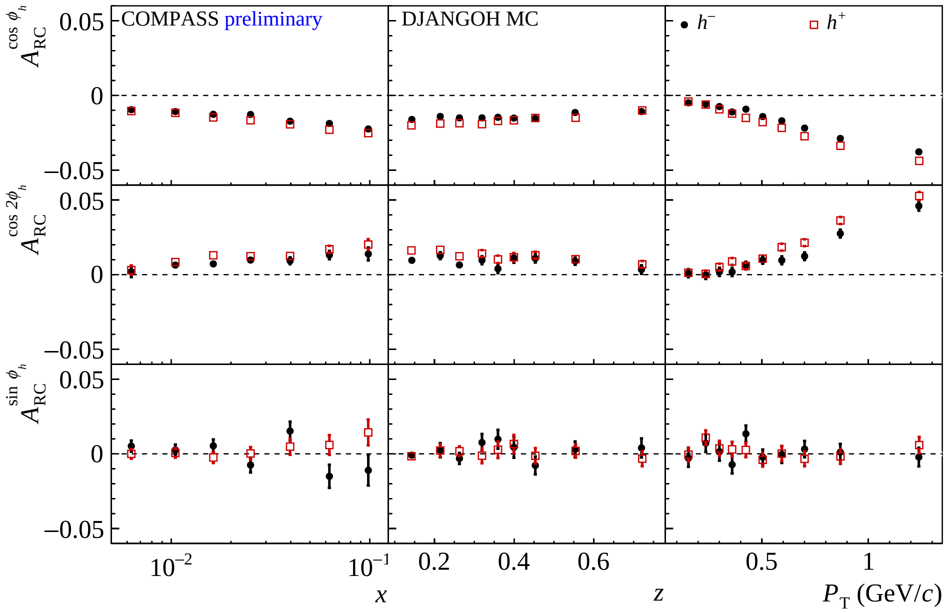

Fig. 14: The azimuthal modulation amplitudes of the radiative correction coefficients.

DJANGOH MC and its validation can be found in Sec. 3.1.

The radiative corrections for the asymmetries are significant, as can be seen from Fig. 14, where the amplitudes A_{RC} of the azimuthal modulations of the correction factors are shown. They are comparable in magnitude to the measured asymmetries (see Fig. 11). The corrections were presented at SPIN2023 [48] and will be applied to the measured asymmetries, which we are being prepared for a release and publication.

3.3 Study of exclusive reactions from 2016 and 2017 data

Generalized Parton Distributions (GPDs) can be studied via exclusive processes, such as Deeply Virtual Compton Scattering (DVCS) or Hard Exclusive Meson Production (HEMP). Various related measurements provide inputs for the parameterisations of different GPDs. The DVCS process is often considered as the golden channel for the study of GPDs. DVCS measurements in the kinematic domain covered by COMPASS encode important information on the chiral-even parton helicity conserving GPD H and indirectly on the transverse extension of partons inside the proton. Hard exclusive production of the scalar meson π^0 is analyzed in parallel to DVCS. The π^0 production constitutes one of the main sources of background in DVCS measurements. On the other hand, the hard exclusive π^0 production channel provides important information on GPDs. In particular it is sensitive to the chiral-even GPDs ($\tilde{H}$, $\tilde{E}$) and also to the parton helicity flip, or to the chiral-odd GPDs (H_T and $\overline{E}_T$). Hard exclusive production of vector mesons (ρ, ω, ϕ, J/ψ) is sensitive to the GPDs conserving the parton helicity (H, E) and allows investigation of contribution of up, down, strange or charm quarks and gluons. They are also sensitive to the chiral-odd GPDs.

Comparatively to the SPSC report presented in June 2022 [39], we are currently finalizing the exclusive π^0 production (see section 3.3.1), updating the Deeply Virtual Compton Scattering (DVCS) analysis (see section 3.3.7), progressing with the analysis of exclusive ϕ production data and exploring exclusive J/ψ production channel (section 3.3.8). All aforementioned analyses are currently being performed using the 2016 data set, while the exploration of the 2017 data set is starting in parallel. The 2017 sample contains about 2 times more statistics compared to the 2016 set (due to a better operation of the SPS in 2017). We recall that the analysis of the small data sample collected during the first one-month-long pilot Run in 2012, lead to 4 publications on these topics: DVCS [49], exclusive π^0 production [50], exclusive vector meson production ρ [1] and ω [51].

3.3.1 Status of exclusive π^0 production

The goal of the measurement is the determination of the exclusive π^0 production cross section using 160 GeV/c polarized μ^+ and μ^- muon beams and a liquid hydrogen target. The multi-differential muon proton cross section:

$$\frac{\mathrm{d}^4\sigma_{\mu\mathrm{p}}}{\mathrm{d}Q^2\mathrm{d}t\mathrm{d}\nu\mathrm{d}\phi} \tag{4}$$

is determined as a function of the virtual photon four-momentum transfer squared Q^2, the four-momentum transfer between the target and recoiled proton t, the virtual photon energy in the laboratory system ν, and the azimuthal angle between the lepton scattering plane and the hadron plane ϕ.

After the correction for acceptance, luminosity and background subtraction, the differential μp cross section is extracted separately for μ^+ and μ^- beams. The unpolarised cross section is obtained by averaging over the two beam polarities. The γ^*p cross section is extracted from the unpolarised muon–proton cross section using the transverse virtual-photon flux $\Gamma = \Gamma(E_\mu, Q^2, \nu)$:

$$\frac{\mathrm{d}^4\sigma_{\mu\mathrm{p}}}{\mathrm{d}Q^2\mathrm{d}t\mathrm{d}\nu\mathrm{d}\phi} = \Gamma\frac{\mathrm{d}^2\sigma_{\gamma^*\mathrm{p}}}{\mathrm{d}t\mathrm{d}\phi} \tag{5}$$

The virtual-photon–proton exclusive π^0 production unpolarised cross-section is decomposed into the following components:

$$\frac{\mathrm{d}^2\sigma^{\gamma^*\mathrm{p}}}{\mathrm{d}t\mathrm{d}\phi} = \frac{1}{2\pi}\left[\frac{\mathrm{d}\sigma_\mathrm{T}}{\mathrm{d}t} + \epsilon\frac{\mathrm{d}\sigma_\mathrm{L}}{\mathrm{d}t} + \epsilon\cos(2\phi)\frac{\mathrm{d}\sigma_\mathrm{TT}}{\mathrm{d}t} + \sqrt{2\epsilon(1+\epsilon)}\cos(\phi)\frac{\mathrm{d}\sigma_\mathrm{LT}}{\mathrm{d}t}\right], \tag{6}$$

where $\sigma_\mathrm{T}, \sigma_\mathrm{L}, \sigma_\mathrm{TT},$ and σ_LT are structure functions and ϵ is the virtual photon polarisation parameter. The subscripts T and L denote the contribution of a transversely and longitudinally polarised γ^*, respectively, the subscripts TT and LT denote the interference terms. The structure functions in equation (6) are connected to the chiral-even and chiral-odd (transversity) GPDs ($\tilde{H}$, $\tilde{E}$, H_T and $\overline{E}_\mathrm{T}$) via the convolution with hard scattering amplitudes. In the following, the ϕ-dependence of the exclusive π^0 cross-section is shown after averaging over the measured $|t|$-range, while the $|t|$-dependence is extracted after the integration over ϕ. A set of phenomenological predictions for exclusive π^0 production channel for COMPASS kinematics are available from GPD models by Goloskokov and Kroll [52]. More results are expected soon by Liuti and collaborators [53] adapting their models for the COMPASS kinematic domain.

COMPASS results from the 2012 pilot Run were published in [50]. Preliminary results from the 2016 data set were presented in June 2022 at the ICHEP2022 conference and later updated for the IWHSS2023 conference (June 2023). The aim of the third and final analysis iteration performed in October 2023 was:

- to take advantage of the last improvements in the COMPASS data reconstruction software and settings and to take into account a better calibration of the electromagnetic calorimeters,
- to improve the evaluation of the background to the exclusive π^0 production, which originates from non-exclusive deep-inelastic scattering processes (SIDIS) where additional low energetic hadrons are produced, but not detected.
- to enlarge the acceptance in ν and Q^2 compared to the first analysis [50]. This allows us to study the evolution of the cross section as a function of Q^2 and dependence on ν (or x_B).

3.3.2 Improvements of the 2016 data production and ECAL calibration

The 2016 measurement was split in ten periods, each lasting two weeks. Each period was divided into two sub-periods with alternating beam polarities. All periods used in this analysis, together with flux values for both beam polarities are listed in Table 3. The statistics of exclusive π^0 events after the selections (described in the next section) is listed in Table 4.

Table 3: RD productions used in this note with corresponding flux values.

period	$N_{\mu^+} (\times 10^8)$	$N_{\mu^-} (\times 10^8)$
2016 P04	9713.13	7532.65
2016 P05	7665.33	6982.63
2016 P06	7789.15	6387.11
2016 P07	8995.02	7909.04
2016 P08	9496.00	8406.54
2016 P09	7423.83	7039.16
total for π^0	51.08 10^{11}	44.26 10^{11}
total DVCS (for reference)	51.99 10^{11}	44.96 10^{11}

Table 4: Number of exclusive π^0 events after all selections from each data periods and normalization to a same muon flux.

	exclusive π^0		normalized to $10 \cdot 10^{11}$ muons	
period	μ^+	μ^-	μ^+	μ^-
2016P04	137	118	141 ± 12	157 ± 14
2016P05	121	104	158 ± 14	149 ± 15
2016P06	128	112	164 ± 15	175 ± 17
2016P07	125	144	139 ± 12	182 ± 15
2016P08	183	136	193 ± 14	162 ± 14
2016P09	117	106	158 ± 15	151 ± 15
total	811	720	159 ± 5.6	163 ± 6.1

Several problems have been discovered in previous stages of data-productions and respective analyses. In particular, it was found that due to a technical glitch, μ^- subperiods of the first three periods were processed with wrong (old) calibration files. This caused the exclusive π^0 signal to be underestimated and embedded in the background, most notably for P05 period. In addition, new Beam Momentum Station (BMS) back-propagation coefficients had to be produced for some of the periods, in order to adapt to the changed position of the beam telescope. These and other issues have all been fixed and new data production has been performed. Current analysis is based on this final improved production.

Apart from underlined fixes, the new production contains new calorimeter timing calibrations, energy calibrations for the calorimeter cells evaluated using the reconstructed π^0 mass peak position adjustment based on dedicated analysis of muon data. All faulty, unstable, or noisy calorimeter cells were mapped and excluded in the production level both in the experimental data and in MC.

Despite the π^0-mass peak corrections have been correctly applied, it turned out that π^0 mass peak was still slightly shifted with respect to the PDG value. Therefore, it was decided to apply extra post-production π^0 mass correction coefficients. This energy correction improved the position of π^0 mass peak and significantly helped to enhance the exclusive π^0 signal above the background. The numbers of π^0 events collected for each period and each beam charge are in a reasonable agreement, as demonstrated in Table 4.

In COMPASS setup the photons can be detected in three electromagnetic calorimeters ECAL0, ECAL1, ECAL2, each made of approximately 2000 cells, placed at 3m, 13m and 35m from the center of the liquid hydrogen target, respectively. Due to the kinematics of the exclusive π^0 production reaction, the largest x_B values (or smallest ν values at fixed Q^2) are reached in the closest calorimeter, ECAL0. The exclusive π^0 production cross section decreases considerably when x_B decreases, so almost no π^0 are expected in ECAL2, which is confirmed by the data. Hence ECAL2 is not used for this analysis.

In the final analysis the 2016 data contain 549, 225 and 37 events with the two decay photons respectively in ECAL0, ECAL1 and ECAL0 × ECAL1 for the μ^+ beam and 486, 194 and 40 events with the two decay photons in ECAL0, ECAL1 and ECAL0 × ECAL1 for the μ^- beam. So there are 68%, 27% and 5% of the events with the two decay photons in ECAL0, ECAL1 and ECAL0 × ECAL1 respectively. This underlines the importance of the new calorimeter ECAL0 build for 2016-2017 measurements, as it allows to reach the largest x_B values (or smallest ν values at fixed Q^2).

3.3.3 *Event selection and improvement of SIDIS background subtraction*

To describe the exclusive π^0 production process $\mu p \to \mu' p' \pi^0$, we will use the following notations:

- k, k' - four-momenta of the incident muon and scattered muon
- q, q' - virtual photon and π^0 four-momentum
- p, p' - target proton and recoil proton four momenta
- E_{π^0} and E_p - the energy of the real photon and of the recoil proton in the lab
- $t = (q - q')^2 = (p - p')^2$ the four-momentum transfer to the proton target (t is negative for exclusive processes)
- $t' = t - t_{\min}$, where $|t_{\min}|$ is the minimum transfer

The event selection and background estimation procedure is split into five main steps. In the very first stage we consider the sample of events with the Ladder, Middle or Outer triggers fired and the following loose kinematics constraints satisfied $0.8 < Q^2/(\mathrm{GeV/c})^2 < 10$ and $0.01 < y < 0.99$.

1. Only reconstructed vertices with an incoming and outgoing muon tracks and no associated spectrometer tracks are considered. In addition vertices are checked to be inside the liquid Hydrogen target volume and to satisfy certain quality criteria (reasonable χ^2, etc.).

2. If at least one vertex is retained, we loop over pairs of photon clusters in the electromagnetic calorimeters with an invariant mass $M_{\gamma\gamma}$ compatible with the π^0 mass (see Fig.15). The lower energy cluster has to have an energy larger than:
   0.5 GeV/c^2 in ECAL0 and 0.63 GeV/c^2 in ECAL1 (to be above the noise threshold in each ECAL cell)
   and the higher energy cluster has to have an energy larger than:
   2 GeV/c^2 in ECAL0 and 2.5 GeV/c^2 in ECAL1 (adapted to the investigated kinematic range).
   As it was noted above, no exclusive π^0 mesons are expected in ECAL2.

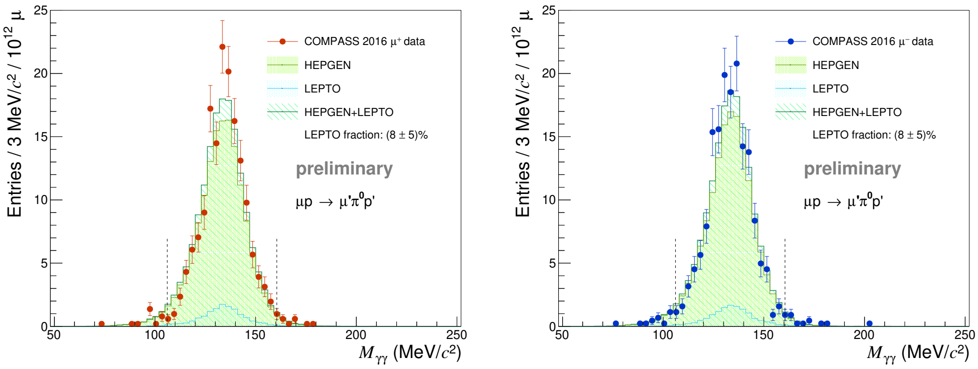

Fig. 15: $M_{\gamma\gamma}$ distribution shown for the full event selection while the cut on the π^0 mass is disabled, μ^+ is shown on the left and μ^- on the right.

3. If the given event contains an exclusive π^0 candidate, we check for recoil tracks reconstructed in the CAMERA detector and build a list of exclusive-event candidates from all possible combinations of selected vertices, π^0 candidates, and CAMERA tracks. The list of candidates is reduced by applying quality cuts and imposing exclusivity criteria on 4 selected variables as described in the following.

   The detection of the proton in CAMERA allows to apply zero missing mass criteria to remove non-exclusive events:

$$M^2_{\text{undet}} = M^2_{X=0} = (k + p - k' - q' - p')^2 \tag{7}$$

   We check then the differences between azimuthal angles and transverse momenta of the proton (with respect to the direction of the incident muon) reconstructed by either the forward spectrometer or CAMERA:

$$\Delta\varphi = \varphi^{\text{CAMERA}} - \varphi^{\text{miss}} \tag{8}$$

$$\Delta p_T = |p_T^{\text{CAMERA}}| - |p_T^{\text{miss}}| \tag{9}$$

   Δp_T can be evaluated either w.r.t. the virtual photon direction or the laboratory Z axis. In fact, the latter option gives a better width and is used in the plot presented in the following.

   In addition, we compare the Z-position of the hits in the inner CAMERA ring given either by the scintillator or by the interpolation between the vertex and the outer ring:

$$\Delta Z = Z_{\text{ring A}} - Z_{\text{interp.}} \tag{10}$$

   The selection criteria applied to the 4 exclusivity variables (see Figs 16) are the following ones:

   - $|\Delta\varphi| < 0.4$ rad
   - $|\Delta p_T| < 0.3$ GeV/c
   - $|\Delta Z| <$16 cm
   - $|M^2_{\text{undet}}| < 0.3$ (GeV/c^2)^2

4. After the above described selections a kinematic fit for the exclusive π^0 production process is applied in order:

   - to improve the selection of exclusive events and to reduce the SIDIS background
   - to determine at best all the observables and notably Q^2, ν, t and ϕ, which are the key variables to study the process.

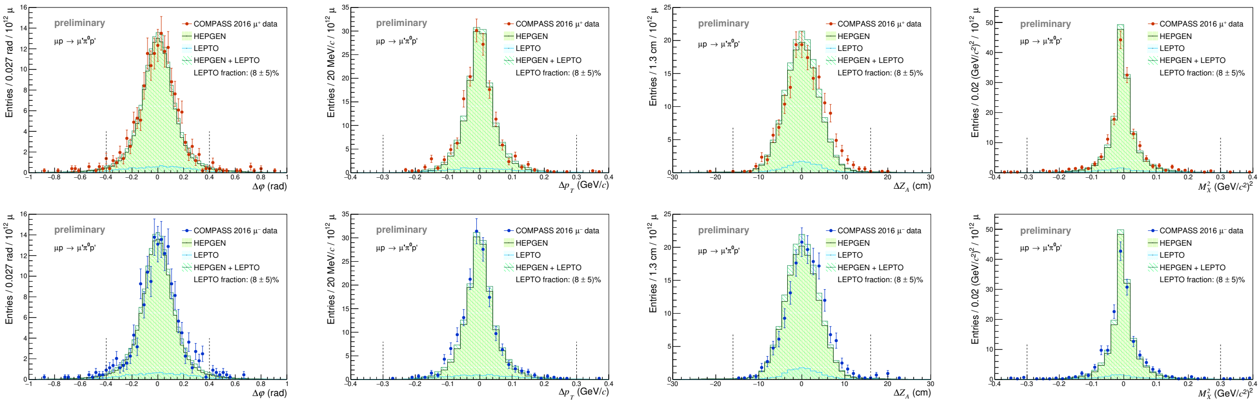

Fig. 16: Distributions of the exclusivity variables for μ$^+$ beam (top row) and μ$^-$ beam (bottom row): $\Delta\varphi$ and Δp_T in the upper row, and ΔZ_A and the four-momentum balance in the bottom row. Each distribution is plotted after applying all the selection criteria except the cut on the plotted variable itself. The data are represented in red. In green the sum of LEPTO and HEPGen++ is shown to describe the share of signal and background in the data. In bright green is shown the HEPGen++ simulation of the exclusive signal and in blue the LEPTO simulation of the non-exclusive contribution. Note that only the events which have successfully passed the kinematic fit are accounted.

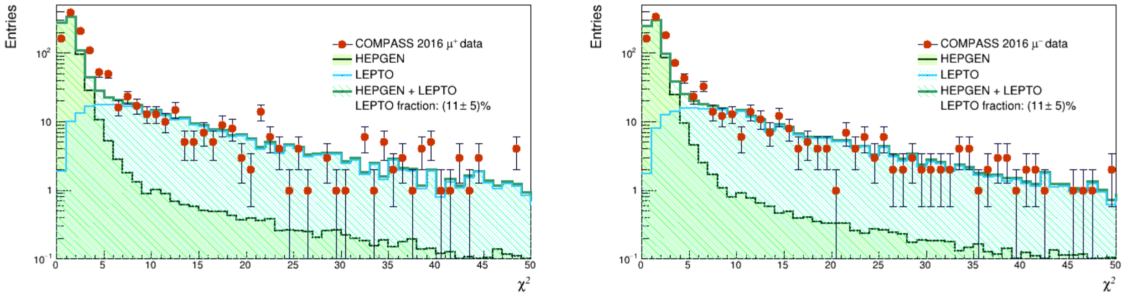

Fig. 17: $\chi^2_{reduced}$ distribution of the kinematic fit for μ+ (left) and μ− (right) beam.

It is verified that the fitting procedure converges and it is checked that the following condition is always satisfied: $\chi^2_{red} < 7$ is applied (see Fig. 17). The effect of varying the χ^2-criterion limits is taken into account at the level of systematic uncertainties.

The last group of selection conditions is defined as follows:

- $|t_{\mathrm{fit}}| \in (0.08, 0.64)$ (GeV/c)^2. Here $|t| = 0.08$ (GeV/c)^2 is safely above the minimum transfer value for a low energetic proton reaching the outer ring of CAMERA and $|t| = 0.64$ (GeV/c)^2 is a safe value for a good separation between protons and other charged particles.
- $0.04 < y_{\mathrm{fit}} < 0.9$; $6.4 < \nu_{\mathrm{fit}} < 40$ GeV; $1 < Q^2_{\mathrm{fit}} < 8$ (GeV/c)^2
  In the final analysis of the 2016 data set the kinematic coverage has been enlarged relatively to the previous analyses (publication of the 2012 pilot Run [50] and previous release of 2022). We benefit from the large geometrical sizes of ECAL0, which gives access to lower ν region. Besides this, we enlarge the domain at larger ν and Q^2. In the previous analyses the kinematic coverage was only $8.5 < \nu_{\mathrm{fit}} < 28$ GeV and $1 < Q^2_{\mathrm{fit}} < 5$ (GeV/c)^2.

Finally, we keep only those events, in which only one combination passes all exclusivity conditions. The loss of events due to this requirement is about 1%.

5. in the next stage of the analysis the SIDIS background fraction is determined. At variance with our previous analyses, this evaluation is now done after the kinematic fit, which results in a smaller background contribution due to a better determination of the observables and improved resolutions.

The LEPTO generator with the so-called high-p_T COMPASS tuning[2] is used to describe the non-exclusive background. The HEPGen++ π^0 generator [54, 55] is used to model the signal distributions – the single π^0 muoproduction. For each HEPGen++ generated events, a weight evaluated using the cross-section of the 2016 version Goloskokov-Kroll (GK2016) model [56] describing our previous COMPASS result with the 2012 data set [50] is assigned. To speed up the weight calculation, a lookup table was generated using the GK2016 model. The events generated by LEPTO and HEPGen++ are independently passed to TGeant [3] which then transports them through the complete simulation of the COMPASS setup. Resulting simulated MC samples are then processed by the event-reconstruction software (CORAL) in the same way as it is done for the real data (RD).

Since only a scarce information is available on the cross section for exclusive π^0 production and SIDIS background contribution in the COMPASS kinematic domain, the reconstructed MC event distributions, are normalised to the experimentally measured π^0 yield and the relative fractions (r_{LEPTO}) and (1-r_{LEPTO}) of the respective LEPTO and HEPGen++ contributions to the total sample are determined from a fit to the two exclusivity variables $\Delta\varphi$ and Δp_T. The fit is done using two different methods: least squares fitting and ROOT TFractionFitter (likelihood fit).

The fit of the MC mixture (HEPGen++ and LEPTO) to the data using TFractionFitter is shown in Figs. 16. One can see that the background events from LEPTO (in blue) are distributed rather flat, while the HEPGen events are concentrated in a narrow peak centred around zero[4].

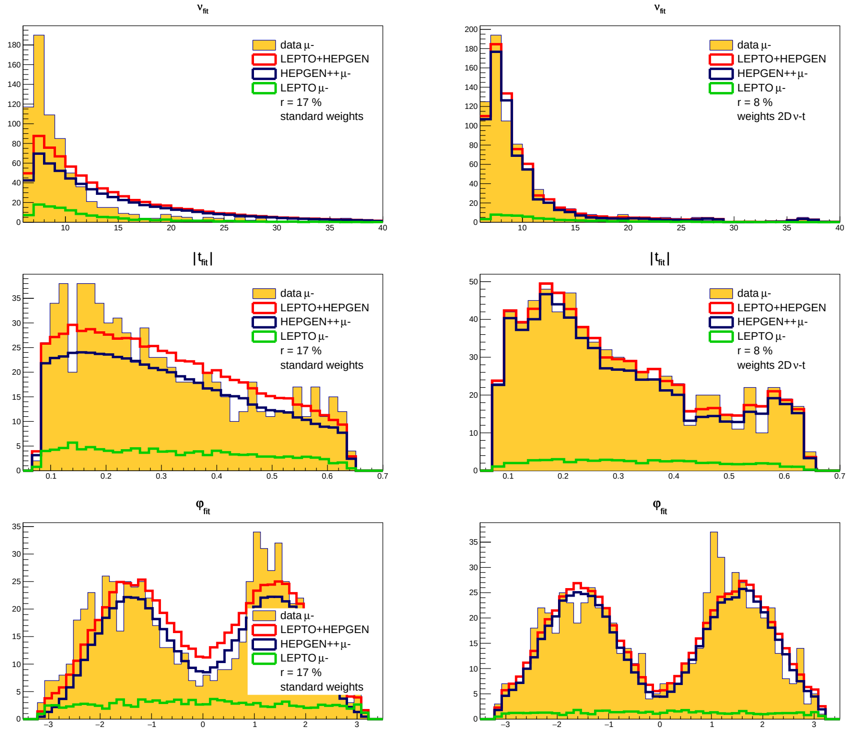

Fig. 18: Distributions of ν (top) and $|t|$ (middle) and ϕ (bottom) before (left) and after (right) re-weighting procedure and new ϕ modulation (with $r_{\mathrm{LEPTO}} = 17\%$ used previously and $r_{\mathrm{LEPTO}} = 8\%$ in the final analysis with still less background).

Scaling the background distribution by the contamination factor r_{LEPTO} and summing it up with the signal component, the obtained total MC distribution can be compared with the experimental data. In Fig.18 (left panels) Monte-Carlo and real data distributions for different exclusive variables are compared. Blue histograms represent HEPGen++ signal distributions, LEPTO background component is

---

[2] used e.g. for COMPASS hadron multiplicity analyses

[3] Geant4 based COMPASS spectrometer simulation tool

[4] Except for the ΔZ_A distribution, which could not be used for the fitting, as both signal and background events originate inside the target, which makes this exclusive variable correlated.

shown in green, while total HEPGen+LEPTO distributions are shown in red. The comparison for ν and $|t|$ distributions reveals clear tensions. In order to fix the tensions, the HEPGen++ weights have been modified via an iterative procedure, which included re-evaluation of r_{LEPTO} fractions and subsequent MC/RD comparisons.

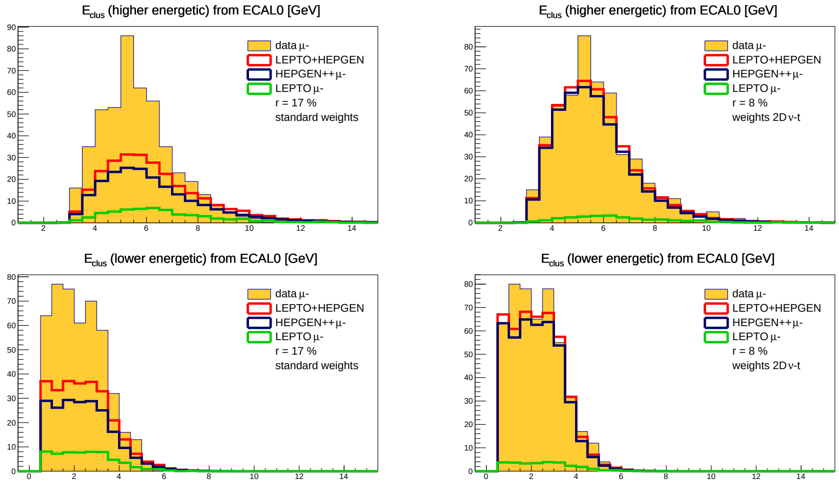

Fig. 19: Energy of clusters in ECAL0 for photon with higher energy (top) and for photon with lower energy (bottom) before (left) and after (right) re-weighting procedure and new ϕ modulation (with $r_{\mathrm{LEPTO}} = 17\%$ used previously and $r_{\mathrm{LEPTO}} = 8\%$ in the final analysis with still less background).

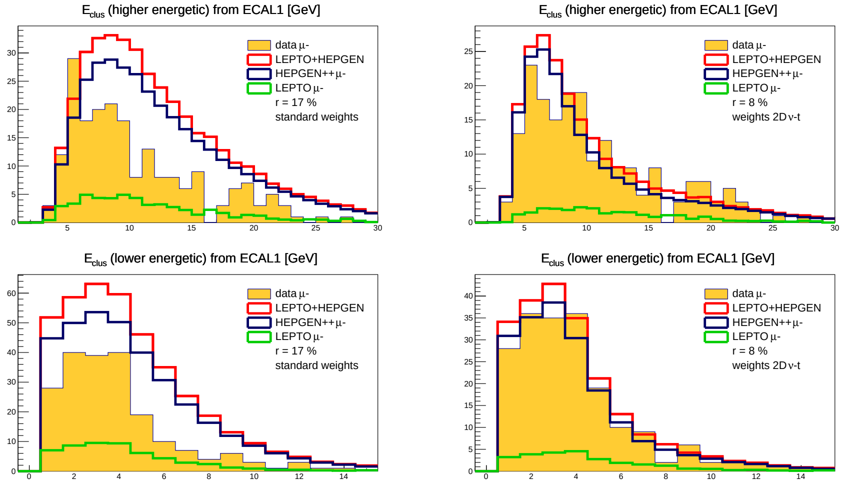

Fig. 20: Energy of clusters in ECAL1 for photon with higher energy (top) and for photon with lower energy (bottom) before (left) and after (right) re-weighting procedure and new ϕ modulation (with $r_{\mathrm{LEPTO}} = 17\%$ used previously and $r_{\mathrm{LEPTO}} = 8\%$ in the final analysis with still less background).

Two re-weighting methods (2D and 1D) have been applied. The 2D method uses two-dimensional MC and RD histograms in ν and $|t|$ to define bin-by-bin weights to improve the agreement between Monte-Carlo and data distributions. In 1D approach, the data is fit by polynomials, which are then used instead of binned histograms, in order to have smooth distributions and avoid over-corrections. As it can be seen in Fig. 18 (right panels) the MC description of the distributions of the two key variables, ν and t, have been significantly improved after re-weighting the generator of the exclusive reaction in HEPGen++. A similar improvement is also obtained for energy of ECAL clusters in ECAL0 and ECAL1 as shown in Figs. 19 and 20. In the current analysis, prior to re-weighting in ν and $|t|$, a better description of the ϕ modulation has been implemented, using the structure-function values measured in the 2016 data analysis instead of the ones obtained from the 2012 data [50]. The resulting improvement is clearly visible in the ϕ_{fit} distribution (last row in Fig. 18).

In conclusion, improving the MC-data agreement by applying the re-weighting procedure in ν and $|t|$ and improving the description of the ϕ modulation, with final choice of the χ^2_{red} (which also affects the signal to background ratio), the r_{LEPTO} values dropped from 35%, to 8%.

3.3.4 Determination of the cross section

For the cross section determination two different kinematic domains are used. First, we used the kinematic domain of the published 2012 data. In the second step, the kinematic domain was enlarged to exploit the enlarged ECAL0 acceptance and the larger data sample for the 2016 data.

Acceptance determination

The phase-space element is denoted by $\Delta\Omega_{nijk} = \Delta|t|_n \Delta\phi_i \Delta Q^2_j \Delta\nu_k$. The acceptance $a(\Delta\Omega_{nijk})$ is calculated in a four-dimensional grid:

- 5 bins in $|t|$: $[0.08, 0.15], [0.15, 0.22], [0.22, 0.36], [0.36, 0.5], [0.5, 0.64]$ (GeV$/c)^2$,
- 8 bins in ϕ: equidistant bins from $-\pi$ to $+\pi$
- 5 bins in Q^2: $[1, 1.5], [1.5, 2.1], [2.1, 3.2], [3.2, 5], [5, 8]$ (GeV$/c)^2$,
- 6 bins in ν: $[6.4, 8.5], [8.5, 10.5], [10.5, 13.9], [13.9, 19.5], [19.5, 26], [26, 40]$ (GeV).

For the acceptance determination, the HEPGen-π^0 MC simulation described in [54, 55] is used. The COMPASS spectrometer acceptance $a_{\Delta\Omega}$ for the phase space element $\Delta\Omega$ is given by:

$$a_{\Delta\Omega} = \sum_{i=1}^{N_{\text{rec}}^{\Delta\Omega}} w_i \Bigg/ \sum_{i=1}^{N_{\text{gen}}^{\Delta\Omega}} w_i \,,$$

where $N_{\text{gen}}^{\Delta\Omega}$ denotes the total number of generated events in the space element $\Delta\Omega$, the $N_{\text{rec}}^{\Delta\Omega}$ represents the reconstructed HEPGen events in the same space element, with the boundaries given by the reconstructed, fitted kinematic variables.

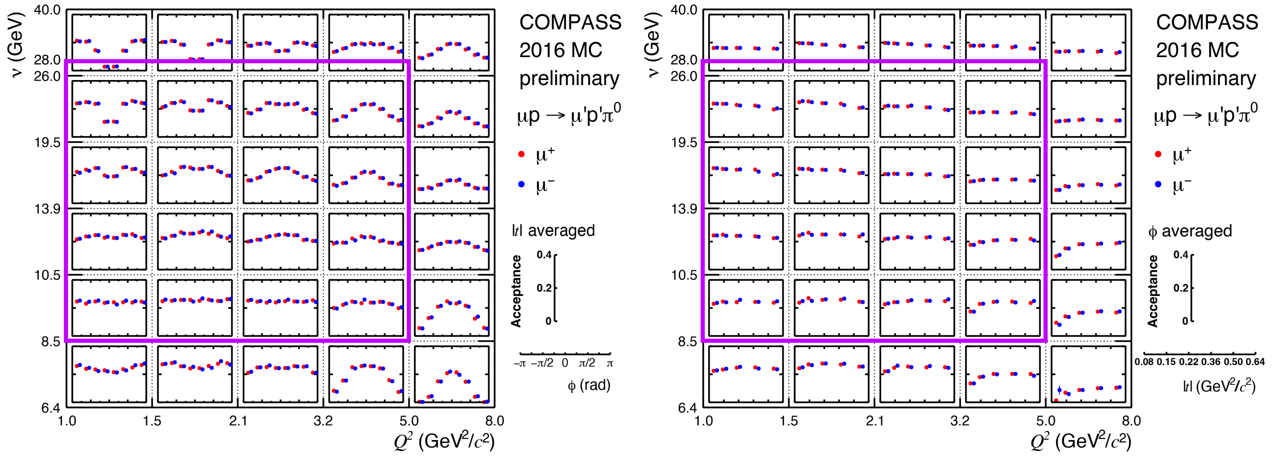

Fig. 21: Acceptance coverage in the current analysis. Only the bins inside the violet boxes were considered in the 2012 pilot Run or in the 2022 analysis. Left panel: Acceptance for the π^0 process shown as a function of Q^2, ν and ϕ for $0.08 < |t| < 0.64$ (GeV$/c)^2$. Each plot in a bin of Q^2 and ν shows the acceptance in 8 equidistant bins of $\phi_{\gamma^*\gamma}$ for μ^+ (in red) and μ^- (in blue) beams. Right panel: Acceptance for the π^0 process shown as a function of Q^2, ν and t for $-\pi < \phi < \pi$. Each plot in a bin of Q^2 and ν shows the acceptance in 5 bins of $|t|$ for μ^+ (in red) and μ^- (in blue) beams.

The acceptance is evaluated individually for each period using dedicated MC simulation. The acceptance corrections used in the cross section determination (see Eq. 14) are done on a period-by-period basis. In Fig. 21 a three-dimensional representation of extracted acceptances is presented. The shown acceptances are extracted from the merged sample of all six periods as a function of ϕ and $|t|$ in Q^2:ν grid. The reduced kinematic domain used with the 2012 pilot Run and for the previous analysis is indicated by a violet rectangle.

In order to show a comparison of the results from the 2016 data with the 2012 results, the binning of the 2012 results had to be used. The corresponding grid used in the analysis of the 2012 data is defined as follows:

- 5 bins in $|t|$: $[0.08, 0.15], [0.15, 0.22], [0.22, 0.36], [0.36, 0.5], [0.5, 0.64]\,(\mathrm{GeV}/c)^2$,
- 8 bins in ϕ: equidistant bins from $-\pi$ to $+\pi$
- 4 bins in Q^2: $[1, 1.5], [1.5, 2.24], [2.24, 3.34], [3.34, 5]\,(\mathrm{GeV}/c)^2$,
- 4 bins in ν: $[8.5, 11.45], [11.45, 15.43],\ [15.43, 20.78], [20.78, 28]\,(\mathrm{GeV})$.

Cross section evaluation

The virtual photon proton cross section is obtained from the measured muon-proton cross section through the relation:

$$\frac{\mathrm{d}\sigma^{\gamma^*\mathrm{p}}}{\mathrm{d}|t|\mathrm{d}\phi} = \frac{1}{\Gamma(Q^2, \nu, E_\mu)} \frac{\mathrm{d}^3\sigma_{\mathrm{T}}^{\mu p}}{\mathrm{d}Q^2\mathrm{d}\nu\mathrm{d}|t|\mathrm{d}\phi}, \tag{11}$$

where the transverse virtual photon flux $\Gamma(Q^2, \nu, E_\mu)$ is given by:

$$\Gamma(Q^2, \nu, E_\mu) = \frac{\alpha_{\mathrm{em}}(1 - x_B)}{2\pi Q^2 y E_\mu} \left[y^2 \left(1 - \frac{2m_\mu^2}{Q^2} \right) + \frac{2}{1 + Q^2/\nu^2} \left(1 - y - \frac{Q^2}{4E_\mu^2} \right) \right], \tag{12}$$

for which the Hand convention [57] is used. Here, m_μ and E_μ denote the mass and energy of the incoming muon, respectively, and α_{em} the electromagnetic fine-structure constant.

The cross section can be evaluated for each beam charge (noted ± in the following) and phase-space segment $\Delta\Omega_{nijk}$ from the data by subtracting the background contributions defined from MC:

$$\left\langle \frac{\mathrm{d}\sigma^{\mu\mathrm{p}\to\mu'\pi^0\mathrm{p}'}}{\mathrm{d}\Omega} \right\rangle_{nijk}^{\pm} = \left\langle \frac{\mathrm{d}\sigma_{\mathrm{data}}^{\mu\mathrm{p}\to\mu'\pi^0\mathrm{p}'}}{\mathrm{d}\Omega} \right\rangle_{nijk}^{\pm} - \left\langle \frac{\mathrm{d}\sigma_{\mathrm{background}}^{\mu\mathrm{p}\to\mu'\pi^0\mathrm{p}'}}{\mathrm{d}\Omega} \right\rangle_{nijk}^{\pm} \tag{13}$$

Considering the yield of each contribution, the virtual photon flux enters as a kinematic prefactor applied on an event by event basis. Finally we obtain:

$$\begin{aligned} \left\langle \frac{\mathrm{d}\sigma^{\gamma^*\mathrm{p}\to\pi^0\mathrm{p}'}}{\mathrm{d}|t|\mathrm{d}\phi} \right\rangle_{nijk}^{\pm} = \frac{1}{\mathcal{L}^{\pm}\Delta t_n \Delta\phi_i \Delta Q_j^2 \Delta\nu_k} \sum_{p\in\mathcal{P}} \left(a_{nijk}^{p,\pm} \right)^{-1} & \left(\sum_{e=1}^{N_{nijk}^{p,\mathrm{data}}\pm} \frac{1}{\Gamma\left(Q_e^2, \nu_e\right)} \right. \\ & \left. - c_{\pi^0}^{p\mathrm{LEPTO}\pm} \cdot (r_{\mathrm{LEPTO}}) \cdot \sum_{e=1}^{N_{nijk}^{p,\pi^0}\pm} \frac{1}{\Gamma\left(Q_e^2, \nu_e\right)} \right) \end{aligned} \tag{14}$$

where $\mathcal{L}$ denotes the luminosity and $\mathcal{P}$ the set of different periods and:

$$\mathcal{L}^{\pm} = \sum_{p\in\mathcal{P}} \mathcal{L}^{p\pm}$$

$$c_{\pi^0}^{p\mathrm{LEPTO}\pm} = \frac{N_{\text{vis. }\pi^0}^{p,\mathrm{data}\pm}}{N_{\text{vis. }\pi^0}^{p,\mathrm{LEPTO}\pm}}$$

The mean cross section in each bin of $(|t|, \phi)$ is constructed as follows:

$$\left\langle \frac{\mathrm{d}\sigma^{\gamma^*\mathrm{p}\to\pi^0\mathrm{p}'}}{\mathrm{d}|t|\mathrm{d}\phi} \right\rangle_{ni}^{\pm} = \frac{\sum_{j,k} \left\langle \frac{\mathrm{d}\sigma^{\gamma^*\mathrm{p}\to\pi^0\mathrm{p}'}}{\mathrm{d}|t|\mathrm{d}\phi} \right\rangle_{nijk}^{\pm} \Delta Q_j^2 \Delta\nu_k}{\sum_j \Delta Q_j^2 \sum_k \Delta\nu_k} \tag{15}$$

The spin-averaged virtual photon cross section is obtained as the average of the two muon beam charges:

$$\left\langle \frac{\mathrm{d}\sigma^{\gamma^* \mathrm{p} \to \pi^0 \mathrm{p}'}}{\mathrm{d}|t|\mathrm{d}\phi} \right\rangle_{ni} = \frac{1}{2} \left(\left\langle \frac{\mathrm{d}\sigma^{\gamma^* \mathrm{p} \to \pi^0 \mathrm{p}'}}{\mathrm{d}|t|\mathrm{d}\phi} \right\rangle_{ni}^{+} + \left\langle \frac{\mathrm{d}\sigma^{\gamma^* \mathrm{p} \to \pi^0 \mathrm{p}'}}{\mathrm{d}|t|\mathrm{d}\phi} \right\rangle_{ni}^{-} \right) \tag{16}$$

In order to study the $|t|$-dependence of the cross section, it can be integrated over the full 2π-range in ϕ:

$$\left\langle \frac{\mathrm{d}\sigma^{\gamma^* \mathrm{p} \to \pi^0 \mathrm{p}'}}{\mathrm{d}|t|} \right\rangle_{n} = \sum_i \Delta\phi_i \left\langle \frac{\mathrm{d}\sigma^{\gamma^* \mathrm{p} \to \pi^0 \mathrm{p}'}}{\mathrm{d}|t|\mathrm{d}\phi} \right\rangle_{ni} \tag{17}$$

Similarly to study the ϕ-modulations of the cross section we determine the $|t|$-average cross section as:

$$\left\langle \frac{\mathrm{d}\sigma^{\gamma^* \mathrm{p} \to \pi^0 \mathrm{p}'}}{\mathrm{d}|t|\mathrm{d}\phi} \right\rangle_{i} = \frac{1}{\sum_n \Delta|t|_n} \sum_n \Delta|t|_n \left\langle \frac{\mathrm{d}\sigma^{\gamma^* \mathrm{p} \to \pi^0 \mathrm{p}'}}{\mathrm{d}|t|\mathrm{d}\phi} \right\rangle_{ni} \tag{18}$$

3.3.5 Results in the kinematic domain of the 2012 data analysis

We recall that the kinematic domain used for the 2012 data analysis and for the previous release of the 2016 data for ICHEP2022 was:

- $8.5\ \mathrm{GeV} < \nu < 28\ \mathrm{GeV}$
- $1\ (\mathrm{GeV}/c)^2 < Q^2 < 5\ (\mathrm{GeV}/c)^2$
- $0.08\ (\mathrm{GeV}/c)^2 < |t| < 0.64\ (\mathrm{GeV}/c)^2$

To be able to compare the results, in the current analysis the cross section was determined in the same kinematic domain.

Figs. 22 and 23 show the results for the averaged differential cross sections as a function of $|t|$ and ϕ. The current results of the 2016 data (in red) are compared with the published results of 2012 data [50] (in blue), and GK'16 model [56] (black line). The current results agree well with the published results within uncertainties, a slightly different $|t|$-shape is observed. As for the 2012 results the prediction does not well describe the observed $|t|$ dependence of the cross section.

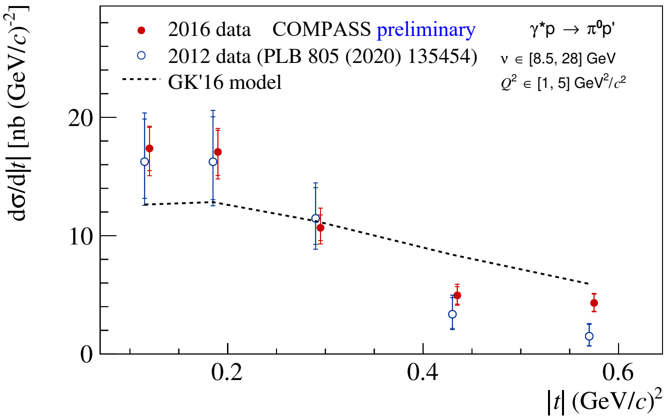

Fig. 22: Differential virtual-photon proton cross-section as a function of $|t|$. Current results of 2016 data (in red) compared with the 2012 data [50] (in blue) and GK'16 model [56] (black line). Both statistical and systematic errors are displayed. Note that for the purpose of the comparison, the small kinematic domain is used: $8.5 < \nu < 28$ GeV, $1 < Q^2 < 5\ (\mathrm{GeV}/c)^2$, $0.08 < |t| < 0.64\ (\mathrm{GeV}/c)^2$.

The ϕ dependence of the spin-independent cross section is fitted according to Eq. 6 using a mean value $\epsilon = 0.997$. The curve is shown in red in Fig. 25 and the results for three structure functions are given in Tab. 5 and are compared to the published results using the 2012 data set. The results agree well within uncertainties.

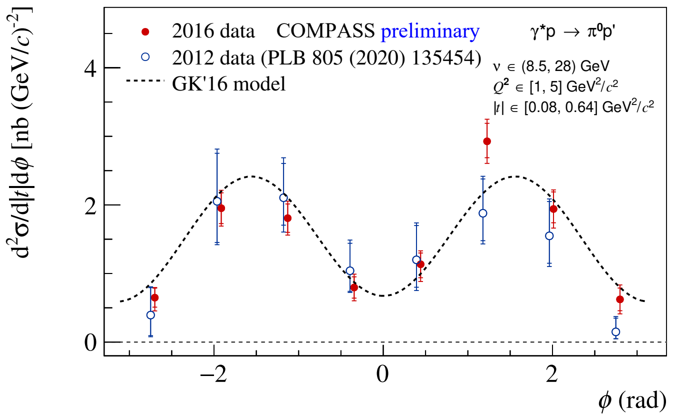

Fig. 23: Differential virtual-photon proton cross-section as a function of ϕ. Results of 2016 data (in red) are compared with the 2012 data [50] and GK'16 model [56]. Both statistical and systematic errors are displayed. Note that for the purpose of the comparison, the small kinematic domain is used: $8.5 < \nu < 28$ GeV, $1 < Q^2 < 5$ (GeV$/c)^2$, $0.08 < |t| < 0.64$ (GeV$/c)^2$.

Table 5: Result for the 3 structure functions in $\frac{\text{nb}}{(\text{GeV}/c)^2}$

	smaller kinematic domain		larger kinematic domain
	2012 data set	2016 data set	2016 data set
$\left\langle \frac{d\sigma_T}{d\lvert t\rvert} + \epsilon\frac{d\sigma_L}{d\lvert t\rvert} \right\rangle$	$(8.1 \pm 0.9_{\text{stat}}{}^{+\,1.1}_{-\,1.0}\big\rvert_{\text{sys}})$	$(9.0 \pm 0.5_{\text{stat}}{}^{+\,1.1}_{-\,1.0}\big\rvert_{\text{sys}})$	$(6.9 \pm 0.3_{\text{stat}}{}^{+\,0.8}_{-\,0.8}\big\rvert_{\text{sys}})$
$\left\langle \frac{d\sigma_{TT}}{d\lvert t\rvert} \right\rangle$	$(-6.0 \pm 1.3_{\text{stat}}{}^{+\,0.7}_{-\,0.7}\big\rvert_{\text{sys}})$	$(-6.4 \pm 0.8_{\text{stat}}{}^{+\,0.3}_{-\,0.3}\big\rvert_{\text{sys}})$	$(-4.5 \pm 0.5_{\text{stat}}{}^{+\,0.2}_{-\,0.2}\big\rvert_{\text{sys}})$
$\left\langle \frac{d\sigma_{LT}}{d\lvert t\rvert} \right\rangle$	$(1.4 \pm 0.5_{\text{stat}}{}^{+\,0.3}_{-\,0.2}\big\rvert_{\text{sys}})$	$(0.5 \pm 0.3_{\text{stat}}{}^{+\,0.7}_{-\,0.4}\big\rvert_{\text{sys}})$	$(0.06 \pm 0.2_{\text{stat}}{}^{+\,0.1}_{-\,0.1}\big\rvert_{\text{sys}})$

3.3.6 *Results in the large kinematic domain and perspectives*

To take in account the larger ECAL0 acceptance and the larger data sample the cross section can also be determined in the larger kinematic domain:

- 6.4 GeV $< \nu < 40$ GeV
- 1 (GeV$/c)^2 < Q^2 < 8$ (GeV$/c)^2$
- 0.08 (GeV$/c)^2 < |t| < 0.64$ (GeV$/c)^2$

The results for the differential virtual-photon proton cross section are presented as a function of $|t|$ in Fig. 24 and of ϕ in Fig. 25. For the first figure data are integrated over the full 2π-range in ϕ, for the second figure data are integrated over the $|t|$-range measured in the COMPASS experiment. The numerical values of the cross section are presented in Table 6 for $|t|$ dependence and in Table 7 for ϕ dependence.

The main contribution to the systematic uncertainties is estimated to come from the evaluation of r_{LEPTO}, the SIDIS background fraction. In Tables 6,7 the estimated systematic uncertainties are quoted along with the cross section values and statistical uncertainties. The systematic uncertainty associated with r_{LEPTO} is labelled as $\sigma_{sys,r_{\text{LEPTO}}}$. Presently the systematic uncertainties originating from kinematic fit and energy thresholds in ECAL0 and ECAL1 are being evaluated. Current estimates are included quadratically in the total systematic error (a weight of 0.7 and 0.3 is given to ECAL0 and ECAL1 contributions, respectively). They can increase or decrease the cross-section values and are marked as $\sigma_{sys,\uparrow}$ and $\sigma_{sys,\downarrow}$, accordingly. Other systematic effects are being investigated (kinematic fit efficiency, ω contribution, diffractive dissociation contribution, radiative corrections, etc.).

Further studies are planned to be carried out on the current, 2016, data set. The cross section is determined for both μ^+ and μ^- beams of opposite polarization. Compared to the equation 6, the complete equation for

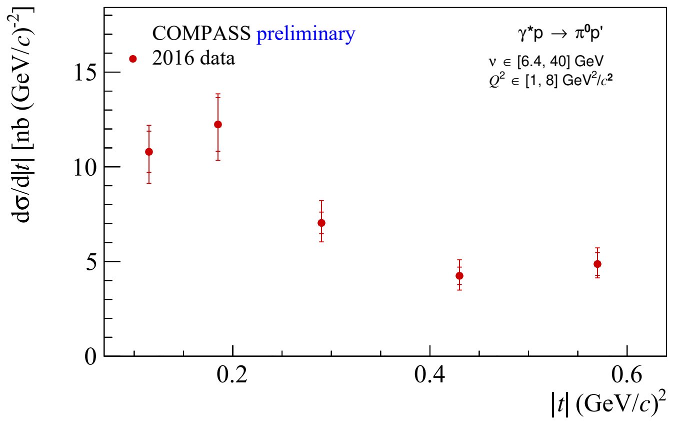

Fig. 24: Differential virtual-photon proton cross section as a function of $|t|$. Data are integrated over the full 2π-range in ϕ. Inner error bars indicate the statistical uncertainties, outer error bars the quadratic sum of statistical and systematic uncertainties. The plot shows the average value of the differential cross section for μ^+ and μ^- using the 2016 data. Results are in the large kinematic domain: $6.4 < \nu < 40$ GeV, $1 < Q^2 < 8\,(\mathrm{GeV}/c)^2$, $0.08 < |t| < 0.64\,(\mathrm{GeV}/c)^2$.

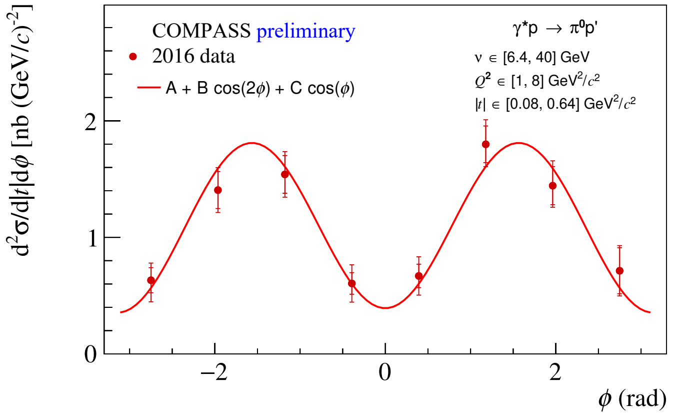

Fig. 25: Differential virtual-photon proton cross section as a function of ϕ. Data are integrated over the $|t|$-range measured in the COMPASS experiment. Inner error bars indicate the statistical uncertainties, outer error bars the quadratic sum of statistical and systematic uncertainties. The plots shows the average value of the differential cross section for μ^+ and μ^- using the 2016 data. The data are fitted with 3 structure functions $\sigma_\mathrm{T} + \epsilon\sigma_\mathrm{L}$, σ_TT and σ_LT Results are in the large kinematic domain: $6.4 < \nu < 40$ GeV, $1 < Q^2 < 8\,(\mathrm{GeV}/c)^2$, $0.08 < |t| < 0.64\,(\mathrm{GeV}/c)^2$.

Table 6: Values in the differential cross section as a function of $|t|$ (units $\frac{\mathrm{nb}}{(\mathrm{GeV}/c)^2}$).

$\lvert t\rvert$ bin	$[0.08, 0.15]$	$[0.15, 0.22]$	$[0.22, 0.36]$	$[0.36, 0.5]$	$[0.5, 0.64]$
$\langle\frac{\mathrm{d}\sigma^{\gamma^* \mathrm{p}\to\pi^0 \mathrm{p}'}}{\mathrm{d}\lvert t\rvert}\rangle$	10.79	12.24	7.04	4.25	4.87
σ_{stat}	1.09	1.42	0.57	0.46	0.60
$\sigma_{sys,r_{\mathrm{LEPTO}}}$	0.65	0.74	0.70	0.43	0.49
$\sigma_{sys,\uparrow}$	0.87	0.87	1.03	0.71	0.62
$\sigma_{sys,\downarrow}$	1.26	1.31	0.82	0.60	0.44

Table 7: Values in the differential cross section as a function of ϕ (units $\frac{\mathrm{nb}}{(\mathrm{GeV}/c)^2}$).

ϕ bin	$[-\pi, -\frac{3\pi}{4}]$	$[-\frac{3\pi}{4}, -\frac{\pi}{2}]$	$[-\frac{\pi}{2}, -\frac{\pi}{4}]$	$[-\frac{\pi}{4}, 0]$	$[0, \frac{\pi}{4}]$	$[\frac{\pi}{4}, \frac{\pi}{2}]$	$[\frac{\pi}{2}, \frac{3\pi}{4}]$	$[\frac{3\pi}{4}, \pi]$
$\langle \frac{\mathrm{d}\sigma^{\gamma^* \mathrm{p} \to \pi^0 \mathrm{p}'}}{\mathrm{d}\lvert t\rvert \mathrm{d}\phi} \rangle$	0.63	1.41	1.54	0.60	0.67	1.80	1.44	0.71
σ_{stat}	0.11	0.16	0.16	0.09	0.10	0.16	0.16	0.20
$\sigma_{sys, r_{\mathrm{LEPTO}}}$	0.08	0.08	0.09	0.10	0.11	0.11	0.09	0.09
$\sigma_{sys,\uparrow}$	0.10	0.11	0.11	0.13	0.13	0.14	0.14	0.11
$\sigma_{sys,\downarrow}$	0.15	0.11	0.11	0.13	0.13	0.11	0.09	0.11

each muon beam charge includes an extra term in $\sin\phi$:

$$\frac{\mathrm{d}^2\sigma^{\leftrightarrows}_{\gamma^* \mathrm{p}}}{\mathrm{d}t\mathrm{d}\phi} = \frac{1}{2\pi}\Big[\frac{\mathrm{d}\sigma_{\mathrm{T}}}{\mathrm{d}t} + \epsilon\frac{\mathrm{d}\sigma_{\mathrm{L}}}{\mathrm{d}t} + \epsilon\cos(2\phi)\frac{\mathrm{d}\sigma_{\mathrm{TT}}}{\mathrm{d}t} + \sqrt{2\epsilon(1+\epsilon)}\cos\phi\frac{\mathrm{d}\sigma_{\mathrm{LT}}}{\mathrm{d}t} \mp |P_l|\sqrt{2\epsilon(1-\epsilon)}\sin\phi\frac{\mathrm{d}\sigma'_{\mathrm{LT}}}{\mathrm{d}t}\Big] \tag{19}$$

The quality of the results should allow us to determine separately for each beam charge the 3 structure functions but also the $\sin\phi$ contribution in order to check the cancellation of this term in the average cross section using μ^+ and μ^- beams.

The 2016 statistics is 2.3 times larger than the 2012 sample. The gain in statistics allows us to study the ν (or x_B) dependence of the cross-section as well as the Q^2 evolution. The final results are being prepared for a release. We underline again that the ECAL0 electromagnetic calorimeter has been enlarged after the pilot 2012 Run to allow to reach smaller ν or x_B. The complete set of data using also the 2017 sample will provide an extra factor 4 in statistics. A first attempt to analyse the 2017 data is now being performed. Studying the pseudo-efficiencies of different detector planes certain alignment issues have been identified and are currently being addressed. Further studies and Monte-Carlo simulations are ongoing.

3.3.7 Status of Deeply Virtual Compton Scattering

The analysis method used for COMPASS DVCS measurements was described in detail in the previous SPSC report [39]. Taking advantage of the new production of the 2016 data and the improvements described in the previous section, a reanalysis of 2016 DVCS data was performed.

In Fig. 26 the ν distribution from experimental data is compared to the MC data. At large ν (small x_B) $80 < \nu < 144$ GeV (see Fig. 26), the exactly calculable Bethe-Heitler (BH) contribution is the only necessary ingredient to reproduce the data. We can observe a good level of agreement between data and the BH MC using HEPGen-BH simulation [54, 55]. The new MC sample incorporates an improved description of the spectrometer, the calorimeters and the recoil proton detector CAMERA. The ratio between the data integrated over $\phi^{\gamma^*\gamma}$ and the MC is updated to the value 98.3 ± 1.0 %.

At small ν (large x_B) $10 < \nu < 32$ GeV (see Fig. 26), the BH contribution decreases significantly, which allows for the determination of the almost "pure" DVCS contribution and the study of its t-dependence and the transverse extension of partons in the proton.

In Fig. 27 (left panel) the $|t|$-dependence of the Virtual-photon proton cross-section $d\sigma/d|t|$ i shown. It can be well described by a single-exponential function $e^{-B|t|}$. In Fig. 27 (right panel) the period by period results are shown, demonstrating a reasonable agreement.

Fig. 28 presents our current result for the B slope together with the previous COMPASS results and those from earlier high-energy experiments that used the same method. The equivalent average squared transverse extension of partons in the proton $\langle b_\perp^2\rangle$ is also indicated.

Note that, the measurements performed by HERA collider experiments H1 [58, 59] and ZEUS [60] in the $x_B/2$ range below 10^{-2} were done at from 2 to 5 times higher Q^2 values compared to COMPASS. The predictions based on models by Goloskov and Kroll (GK) [61–63] and Kumericki-Mueller (KKM15) [64, 65], are shown for two average Q^2 values: COMPASS-like $\langle Q^2\rangle = 1.8$ (GeV/c)^2) and HERA-like $\langle Q^2\rangle = 10.0$ (GeV/c)^2).

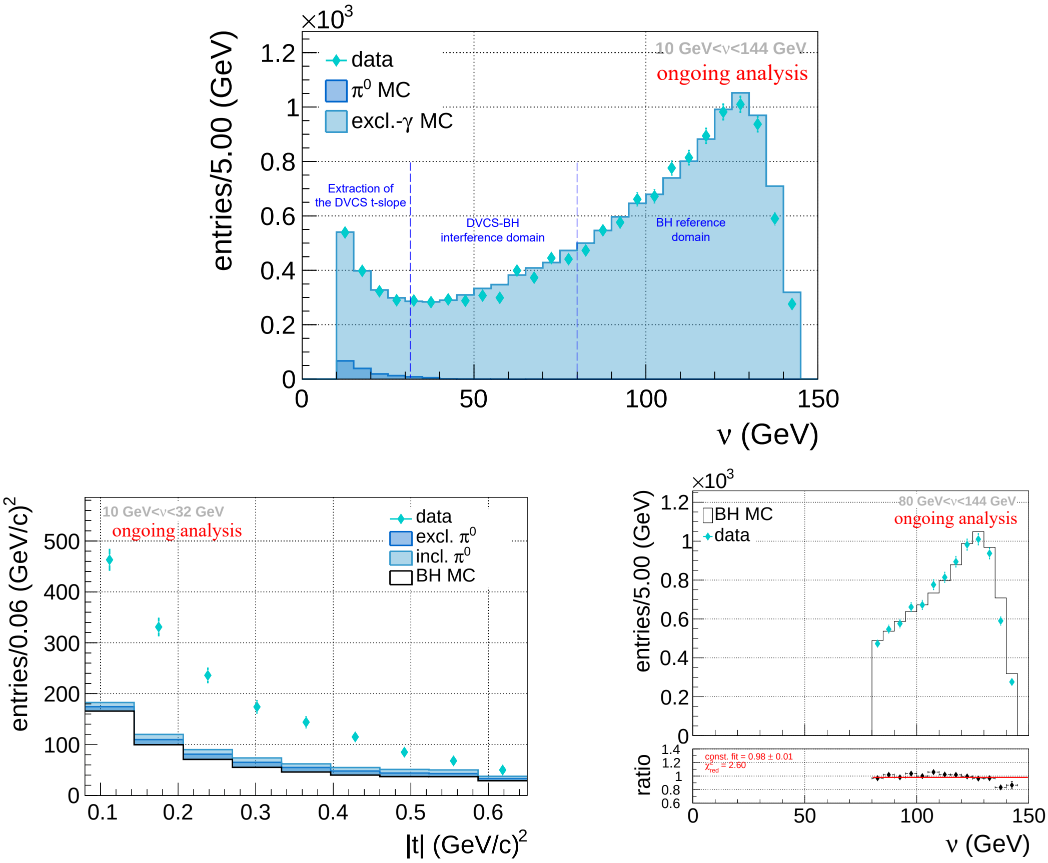

Fig. 26: Top: ν distribution of the data compared to a complete MC including π^0 background when only one π^0 photon decay is detected and the exclusive-single photon process (coherent sum of BH and DVCS). Bottom right: ν distribution of the data at large ν $80 < \nu < 144$ GeV compared to MC including only BH. Bottom left: t distribution of the data at small ν $10 < \nu < 32$ GeV compared to MC including only BH and π^0 background. It remains a significant DVCS contribution to analyse its t-dependence.

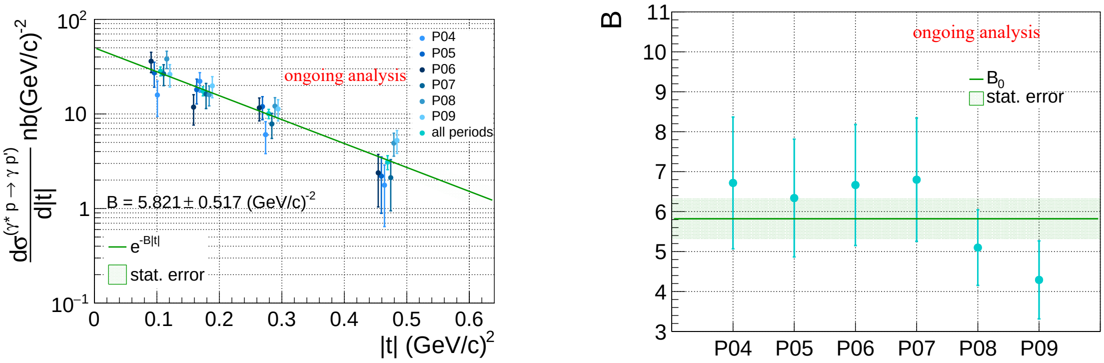

Fig. 27: Left panel: Virtual-photon proton cross-section $d\sigma/d|t|$ evaluated in 4 $|t|$ bins. Only the statistical errors are reported. The observed $|t|$-dependence can be well described by a single-exponential function $e^{-B|t|}$. The 4 data points are fitted using a binned maximum-likelihood method. The results for each of the periods are shown along with the data points averaged over all periods. Right panel: period by period B-slope values. The smooth horizontal green line represents the B-slope for the entire sample, with the light green band indicating the statistical uncertainty.

The results of our two analyses (2022 and 2023) of the 2016 data are compatible while there is a 2 sigma difference between the current result and the one published using the 2012 pilot Run data. Our new value of the t-slope parameter B was obtained with a more advanced analysis method than that of the previous analysis and an improved recoil proton detector CAMERA. The cross check of the new analysis is still ongoing. The result

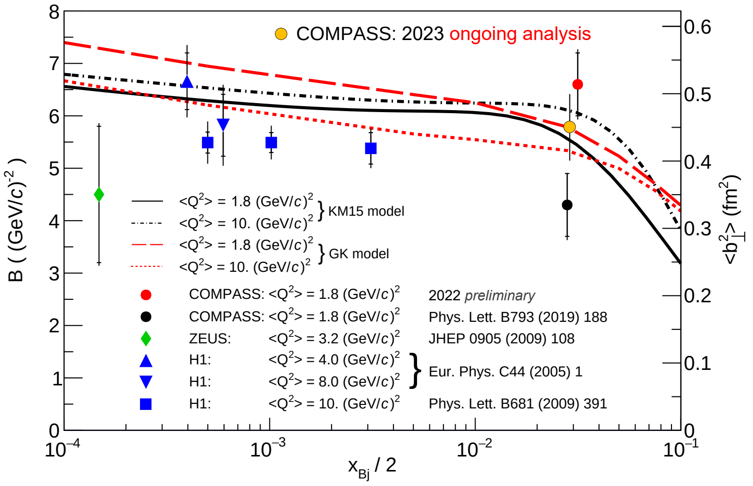

Fig. 28: Results from COMPASS and previous measurements by H1 [58, 59] and ZEUS [60] on the $|t|$-slope parameter B, or equivalently the average squared transverse extension of partons in the proton, $\langle r_\perp^2 \rangle$, as probed by DVCS at the proton longitudinal momentum fraction $x_B/2$. Inner error bars represent statistical and outer ones the quadratic sum of statistical and systematic uncertainties. The black COMPASS point has been obtained using the 2012 pilot Run, while the red and yellow COMPASS points correspond to the 2016 data in the first analysis made in 2022 and in the recent analysis made in 2023, respectively. Predictions of the GK [61–63] and KM15 [64, 65] models are also shown. The red dashed (doted) curves from GK and the solid (dashed-dotted) curves from KM15 are evaluated for Q^2 = 1.8 (10) (GeV/c)^2.

will be further improved by analysing the full 2017 data set, which is 3 times larger than the 2016 analysed data set.

3.3.8 Investigation of ϕ and J/ψ production

In 2021, three new analyses of exclusive vector meson production, namely that of ϕ, J/ψ and ω, have been started using the data from 2016-2017. The motivations behind these analyses, as well as preliminary results on ϕ were reported to the SPSC in 2022 [39].

Since then, while the analysis of ω, which purpose was to improve on the precision of our publication from the 2012 pilot Run [51], was postponed, the other two have been continued. For these, two alternative event selections are now being considered, depending upon whether the information from the recoil detector, CAMERA, is disregarded or not. In the first case, the aim is to cover a wide kinematical domain, unrestricted by the limited range in momentum transfer squared t of CAMERA, for the extraction of the Spin Density Matrix Elements (SDMEs), as was described in [1, 51]. The exclusivity of the selection is then enhanced by a cut on the absolute value of the missing energy:

$$|E_{miss}| \; = \; \left| \frac{M_X^2 - M^2}{2M} \right| \; < \; cut \; , \tag{20}$$

where M_X^2 is the missing mass squared of the final state and M is the proton mass. In the second case, the aim is to determine the absolute cross-section and its dependence upon t. The use of CAMERA, complemented by a kinematically constrained vertex fit where energy-momentum conservation is enforced, allows to suppress dissociative diffraction, *i.e.* the process where a dissociation of the target proton is taking place, and retain only, so-called, elastic diffraction. In fact, dissociative and elastic events were shown to have distinct t dependence in an analysis of exclusive ϕ events at HERA [66]. On the contrary, SDMEs are thought to be less affected by dissociation. This assumption was checked to hold, within experimental uncertainty, for the overlap of two selections, in a preliminary analysis of ϕ events at COMPASS. We intend to double-check it on full statistics.

3.3.9 Exclusive ϕ production

The CAMERA-less analysis of ϕ was redone on the newest production (see Tab. 3) of reconstructed data, with a careful rejection of pathological events (*aimed at enabling a faithful MC simulation*). Preliminary results are shown on Fig. 29. It was checked that they are compatible with those of the previous analysis, reported in [39]. A $\sim$1% gain in statistics, obtained despite the more aggressive rejection policy, illustrates the quality of the new production.

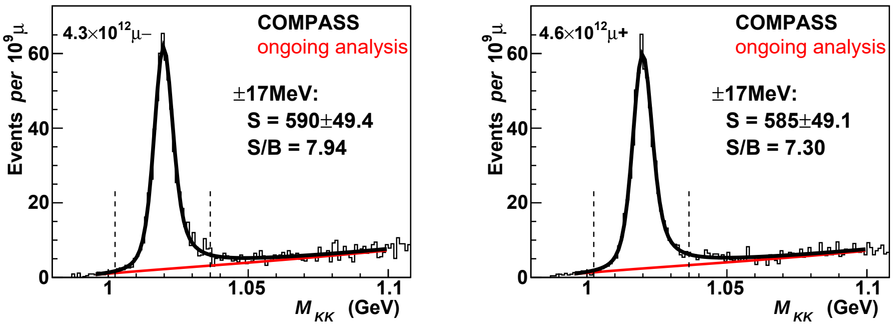

Fig. 29: Selection of exclusive ϕ production. Distribution of the K^+K^- invariant mass for $\mu-$ (*left*) and $\mu+$ (*right*) beam particles. All of the available 2016 statistics is considered. The CAMERA recoil detector is not used, exclusivity being enhanced *via* eq. (20) with $cut = 2.5$ GeV. The distributions are fitted with the relativistic Breit-Wigner describing the natural shape of the ϕ convoluted with a Gaussian describing the response of the experimental apparatus, plus a polynomial background.

3.3.10 Exclusive J/ψ production

Exclusive J/ψ production at COMPASS would provide data to further constrain phenomenological models of GPDs, such as that of Kroll and Goloskokov. Unfortunately, the threshold region, home to a rich physics program, including the search for pentaquark states, and studied at GlueX [67], is beyond our reach.

A preliminary analysis, bearing on 2016 data, was done in 2019. The work was resumed in 2023. Events considered are required to have a topology as that of the process:

$$\mu p \rightarrow \mu' p' J/\psi \rightarrow \mu' p' \mu^+ \mu^- \tag{21}$$

Therefore, they should contain an incident muon track, a scattered muon track and two muon tracks with opposite charges. The two ”decay” muons are identified in our muon-ID system. The rest of the selection is similar to that used for ϕ. Preliminary results are shown on Fig 30, based on the data collected in 2016 and 2017 during 12 periods, each approximately 2 weeks long, *i.e.* approximately 12/13th of the available statistics. Our aim is to extract the t slope, and, if statistics permit, SDMEs.

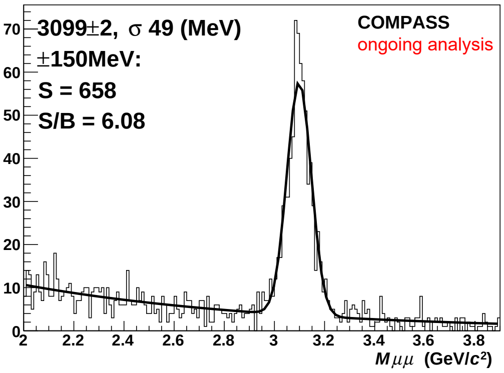

Fig. 30: Selection of exclusive J/ψ production. Distribution of the $\mu^+\mu^-$ invariant mass. Most of the 2016/17 statistics is considered. Exclusivity is ensured by the observation of the full $p\mu\mu^+\mu^-$ final state (*thanks to CAMERA*) and the requirement of energy-momentum conservation. The kinematically constrained vertex fit described in the text is applied.

4 General status of 2015, 2018 data analyses: Drell–Yan and Charmonium studies

The analyses of the COMPASS Drell-Yan data collected in 2015 and 2018 proceed towards producing the final papers. The Drell-Yan transverse spin asymmetries related articles (conventional TSAs and q_T-weighted TSAs) are close to completion, both being at advanced drafting stage.

The cross-section analyses for the Drell-Yan channel in high mass range and for the charmonium production are being finalised. Both studies require careful simulation of the spectrometer and data-taking conditions for precise acceptance evaluation. The first J/ψ cross-section ratio results, namely, the tungsten to aluminium ratio, were released last year in August, while the Drell-Yan cross sections measured in ammonia, aluminium and tungsten were released this year in September.

The study of the angular dependence of the Drell-Yan and J/ψ production processes, often called Unpolarised Asymmetries (UAs), also requires the detailed knowledge of acceptance. The angular dependence relies strongly on the correct description of real data by the Monte Carlo, being tested in the studies done for cross section extraction. The present strategy is to address the remaining issues on the DY and charmonium UAs after the respective TSAs and cross-section analyses are concluded on these common aspects.

Our study dedicated to the double J/ψ production in pion-nucleon interactions has recently been published [4].

4.1 Transverse-spin-dependent azimuthal asymmetries in J/ψ mass range

This work follows the study of the Drell-Yan transverse-spin-dependent azimuthal asymmetries (TSAs) extracted in the high mass range 4.3 < $M_{\mu\mu}$/(GeV/c)^2< 8.5. In order to describe the dimuon production process and the TSAs, we adopt the following standard notations:

P_π, P_N,	4-momenta of the pion, and of the target nucleon, correspondingly
ℓ, $\bar{\ell}$, $q = \ell + \bar{\ell}$,	4-momenta of the lepton, the antilepton and of the virtual photon
S_T,	transverse component of the target polarization
$Q^2 = q^2$,	photon virtuality
$M_{\mu\mu}^2 = Q^2$,	squared invariant mass of the dimuon
q_T,	transverse component of the virtual photon momentum
$x_\pi = q^2/(2P_\pi \cdot q)$,	pion Bjorken variable (often referred to as x_1, x_b)
$x_N = q^2/(2P_N \cdot q)$,	nucleon Bjorken variable (often referred to as x_2)
$x_F = x_\pi - x_N$,	Feynman variable.

The dependence of the cross section on the target spin and on the polar and azimuthal angles of the outgoing leptons is commonly described using the target rest (TF) and the Collins Soper (CS) coordinate systems [68, 69], presented in Fig. 31. When the polarizations of the produced leptons are summed over, the general expression of the cross-section of pion-nucleon lepton-pair production off a transversely polarised nu-

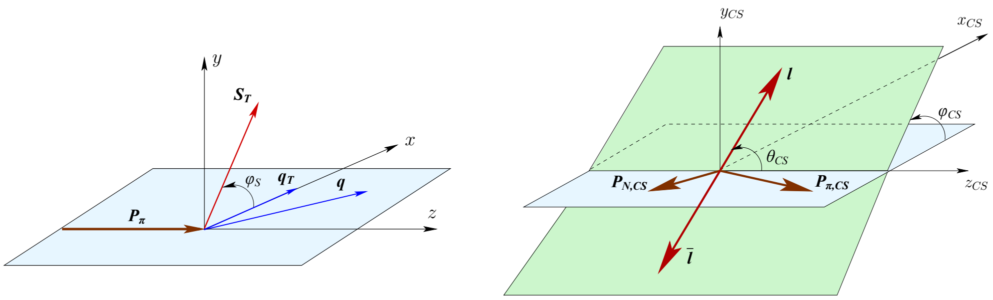

Fig. 31: Reference systems. Left panel: target rest frame. Note that z-axis (x-axis) is chosen along the beam momentum (along q_T). Right panel: the Collins-Soper frame. It is a virtual photon rest frame obtained from the TF frame by boosting first along the z-axis and then along the x-axis so that both the longitudinal and the transverse momenta of the virtual photon vanish.

cleon can be written as follows:

$$
\begin{aligned}
\frac{d\sigma}{dq^4 d\Omega} \propto\ & \hat{\sigma}_U \Bigg\{ 1 + A_U^1 \cos^2\theta_{CS} + \sin 2\theta_{CS} A_U^{\cos\varphi_{CS}} \cos\varphi_{CS} + \sin^2\theta_{CS} A_U^{\cos 2\varphi_{CS}} \cos 2\varphi_{CS} \\
& + S_T \Big[(A_T^{\sin\varphi_S} + \cos^2\theta_{CS} \tilde{A}_T^{\sin\varphi_S}) \sin\varphi_S \\
& + \sin 2\theta_{CS} \left(A_T^{\sin(\varphi_{CS}+\varphi_S)} \sin(\varphi_{CS}+\varphi_S) + A_T^{\sin(\varphi_{CS}-\varphi_S)} \sin(\varphi_{CS}-\varphi_S) \right) \\
& + \sin^2\theta_{CS} \left(A_T^{\sin(2\varphi_{CS}+\varphi_S)} \sin(2\varphi_{CS}+\varphi_S) + A_T^{\sin(2\varphi_{CS}-\varphi_S)} \sin(2\varphi_{CS}-\varphi_S) \right) \Big] \Bigg\}
\end{aligned} \tag{22}
$$

Here q is the four-momentum of the exchanged virtual photon and $\hat{\sigma}_U = \left(F_U^1 + F_U^2\right)$, with F_U^1, F_U^2 being the polarization and azimuth-independent structure functions. The subscript $(U)T$ denotes transverse polarization (in)dependence. The expression contains three unpolarized, i.e. target polarization-independent, and five transverse-target polarization-dependent azimuthal asymmetries (hereafter referred to as UA and TSA, respectively). The asymmetries are defined as ratios of corresponding structure functions to the unpolarized ones ($\hat{\sigma}_U$) and are accessed as the amplitudes of the respective modulations in the azimuthal (polar) angle of the lepton momentum in the Collins-Soper frame, ϕ_{CS} (θ_{CS}), and azimuthal angle of the target spin vector in the target rest frame, ϕ_S [68–70]. All five TSAs are being extracted by COMPASS for different dimuon invariant mass ranges using data collected with transversely polarized proton NH_3 target. The three UAs (often refereed as $\lambda = A_U^1$, $\mu = A_U^{\cos\varphi_{CS}}$, $\nu = 2A_U^{\cos 2\varphi_{CS}}$), in addition to NH_3 target data can also be extracted from data collected with the two nuclear targets (aluminum (Al) and tungsten (W)). Extraction of UAs requires extensive knowledge of the azimuthal acceptance of COMPASS setup and dedicated Monte-Carlo studies. The corresponding analysis for Drell-Yan channel is ongoing (preliminary results have been released in 2021), while J/ψ mass range studies have been started, but are not concluded, yet. In the present analysis for J/ψ TSAs we use $\lambda = A_U^1 = 0$ as an educated guess based on previous measurements done by other experiments, see Fig. 32.

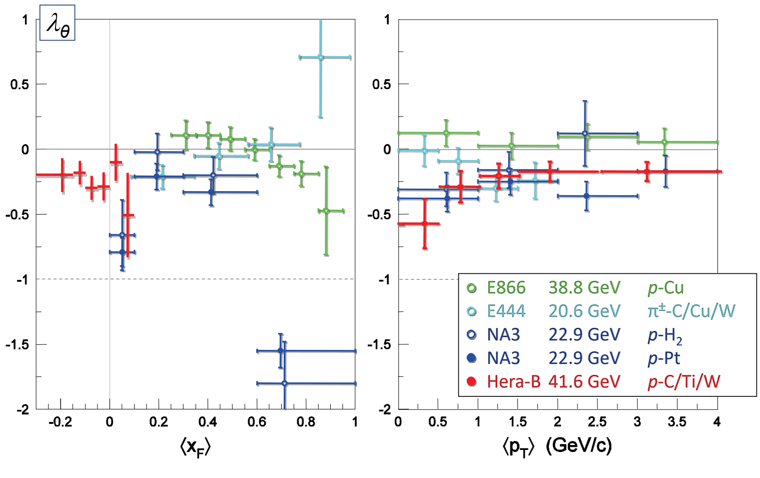

Fig. 32: Collection of λ measurement results for J/ψ production from different experiments.

One of the UAs and two out of five TSAs entering in Eq. 4.1 can be described by contributions from only twist-2 TMD PDFs. These are the $A_U^{\cos 2\varphi_{CS}}$, $A_T^{\sin(2\varphi_{CS}-\varphi_S)}$ and $A_T^{\sin(2\varphi_{CS}+\varphi_S)}$ terms. The $A_U^1 = \left(F_U^1 - F_U^2\right) / \left(F_U^1 + F_U^2\right)$ asymmetry in addition to the twist-2 structure function F_U^1 contains a higher-twist (HT) object F_U^2. At leading order of perturbative QCD, within the twist-2 approximation, $F_U^2 = 0$ and therefore $A_U^1 = 1$. Similarly, the two Sivers components the $A_T^{\sin\varphi_S} = \left(F_{UT}^1 + F_{UT}^2\right) / \left(F_U^1 + F_U^2\right)$ and $\tilde{A}^{\sin\varphi_S} = \left(F_{UT}^1 - F_{UT}^2\right) / \left(F_U^1 + F_U^2\right)$ asymmetries, along with twist-2 F_{UT}^1, contain F_{UT}^2 structure function which vanishes at LO, thus leading to $A_T^{\sin\varphi_S} = \tilde{A}^{\sin\varphi_S}$. Remaining three azimuthal asymmetries, namely $A_U^{\cos\varphi_{CS}}$, $A_T^{\sin(\varphi_{CS}-\varphi_S)}$, $A_T^{\sin(\varphi_{CS}+\varphi_S)}$ are purely 'higher-twist' functions. Assuming $A_T^{\sin\varphi_S} \approx \tilde{A}^{\sin\varphi_S}$ we can re-write the Eq. 4.1 in the following way:

$$\begin{aligned}
\frac{d\sigma}{dq^4 d\Omega} \propto\ & \hat{\sigma}'_U \Big\{ 1 + D_{[\sin 2\theta_{CS}]} A_U^{\cos\varphi_{CS}} \cos\varphi_{CS} + D_{[\sin^2\theta_{CS}]} A_U^{\cos 2\varphi_{CS}} \cos 2\varphi_{CS} \\
& + S_T \Big[D_{[1+\cos^2\theta_{CS}]} A_T^{\sin\varphi_S} \sin\varphi_S \\
& + D_{[\sin 2\theta_{CS}]} \left(A_T^{\sin(\varphi_{CS}+\varphi_S)} \sin(\varphi_{CS}+\varphi_S) + A_T^{\sin(\varphi_{CS}-\varphi_S)} \sin(\varphi_{CS}-\varphi_S) \right) \\
& + D_{[\sin^2\theta_{CS}]} \left(A_T^{\sin(2\varphi_{CS}+\varphi_S)} \sin(2\varphi_{CS}+\varphi_S) + A_T^{\sin(2\varphi_{CS}-\varphi_S)} \sin(2\varphi_{CS}-\varphi_S) \right) \Big] \Big\},
\end{aligned} \tag{23}$$

where $\hat{\sigma}'_U = \left(F_U^1 + F_U^2\right)\left(1 + A_U^1 \cos^2\theta_{CS}\right)$. In analogy to the polarized semi-inclusive deep inelastic scattering (SIDIS) case, we introduced the so-called depolarisation factors defined as: $D_{[f(\theta_{CS})]} = f(\theta_{CS})/(1 + A_U^1 \cos^2\theta_{CS})$. Assuming $A_U^1 = 0$ this simplifies to: $D_{[f(\theta_{CS})]} = f(\theta_{CS})$. During the analysis we encountered problems with unbinned-likelihood fit convergence in specific kinematic bins covering low x_F and low x_π regions. It turned that limiting the fit to only twist-2 asymmetries eliminates convergence problems and stabilizes the fit. Presented in this Report preliminary results were obtained using the following leading order (twist-2) approximation of the expression for the lepton-production cross-section in pion-nucleon interactions:

$$\begin{aligned}
\frac{d\sigma}{dq^4 d\Omega} \propto\ & \hat{\sigma}'_U \Big\{ 1 + \sin^2\theta_{CS} A_U^{\cos 2\varphi_{CS}} \cos 2\varphi_{CS} \\
& + S_T \Big[(1+\cos^2\theta_{CS}) A_T^{\sin\varphi_S} \sin\varphi_S \\
& + \sin^2\theta_{CS} \left(A_T^{\sin(2\varphi_{CS}+\varphi_S)} \sin(2\varphi_{CS}+\varphi_S) + A_T^{\sin(2\varphi_{CS}-\varphi_S)} \sin(2\varphi_{CS}-\varphi_S) \right) \Big] \Big\},
\end{aligned} \tag{24}$$

Within LO QCD parton model framework the $A_U^{\cos 2\varphi_{CS}}$ UA is related to the Boer–Mulders ($h_1^\perp$) TMD PDFs of the proton, while the three TSAs $A_T^{\sin\varphi_S}$, $A_T^{\sin(2\varphi_{CS}+\varphi_S)}$ and $A_T^{\sin(2\varphi_{CS}-\varphi_S)}$ are related to Sivers ($f_{1T}^\perp$), pretzelosity ($h_1^\perp$) and transversity (h_1) TMD PDFs of the proton, respectively [68, 69]. In case of the Sivers asymmetry the proton PDF is convoluted with unpolarized pion PDF. For the other three LO TSAs, respective proton PDFs are convoluted with Boer-Mulders PDF of the pion and thus can be used to study this function further and possibly to determine its sign.

All three aforementioned nucleon TMD PDFs induce analogous twist-2 TSAs in the general expression for the cross section of unpolarized-hadron production in SIDIS of leptons off transversely polarized nucleons [40, 68, 71]. These TSAs were extensively studied by HERMES and COMPASS experiments (see Refs [72],[73] and references therein).

The Sivers function [74] describes the left-right asymmetry in the distribution of unpolarized partons in the nucleon with respect to the plane spanned by the momentum and spin vectors of the nucleon. Within the TMD framework of QCD the two naively time-reversal odd TMD PDFs, *i.e.* the quark Sivers functions $f_{1T}^\perp$ and Boer-Mulders functions $h_1^\perp$, are expected to have opposite sign when measured in SIDIS or DY [75–77]. The sign-change of Sivers TMD PDFs is considered to be a crucial test of QCD. In contrast to the Sivers function, transversity and pretzelosity TMD PDFs are predicted to be genuinely universal, *i.e.* they do not change their sign between SIDIS and DY measurements [78], which is yet another fundamental QCD prediction to be explored.

In various SIDIS and Drell-Yan studies carried out at COMPASS, it is convenient to disentangle four Q^2 or (in case of Drell-Yan) four $M_{\mu\mu} = Q$ dimuon invariant mass-ranges [69, 79]:

i) $1 <$ $M_{\mu\mu}$/(GeV/c)$^2 <$ 2: ”low mass” range, where several dimuon production channels contribute;

ii) $2 <$ $M_{\mu\mu}$/(GeV/c)$^2 <$ 2.5: ”intermediate mass” range, similar to the ”low mass” range;

iii) $2.5 <$ $M_{\mu\mu}$/(GeV/c)$^2 <$ 4.3: ”charmonium (J/ψ and ψ') mass range”;

iv) $4.3 <$ $M_{\mu\mu}$/(GeV/c)$^2 <$ 8.5: ”high mass” range where Drell-Yan channel dominates.

In this analysis we considered only the J/ψ mass range, shrinking it to 2.85 $< M_{\mu\mu}$/(GeV/c)$^2 <$, which corresponds to the J/ψ-peak region in our data. Applying this selection, we exclude ψ' region and reduce the background contamination, which is estimated to be below 8%.

Under certain assumptions (e.g. dominance of the $q\bar{q}$ annihilation process for J/ψ-production in COMPASS kinematics rather than gluon fusion) J/ψ channel can be considered as an alternative way to access quark TMD PDFs and especially to test the sign-change of the Sivers function as proposed in Ref. [80]. Assuming that gluon Sivers contribution, as well as the contribution from J/ψ originating from feed-down decays is small and neglecting related dilution effects, the Authors of Ref. [80] conjectured that the Sivers asymmetry in the J/ψ-peak region can be quite significant at COMPASS kinematics, see Fig. 33.

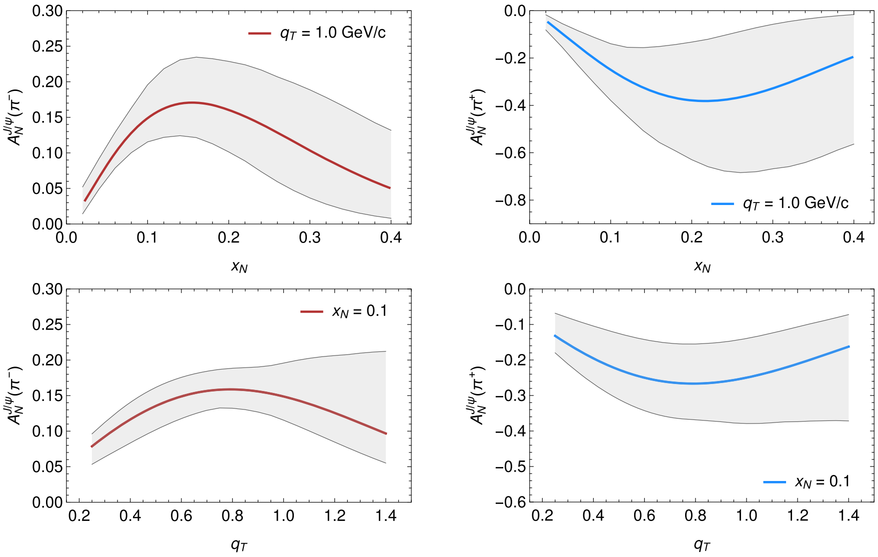

Fig. 33: Model predictions for the J/ψ Sivers asymmetry in COMPASS kinematics [80].

On the other hand, using Color Evaporation Model (CEM) approach the Authors of Ref. [81] suggested that it is rather gg-fusion contribution that dominates in COMPASS kinematics. This makes the interpretation of the TSAs from the COMPASS J/ψ-production data more elaborate. For example, in case of the dominance of gg-fusion, the J/ψ TSA measurements can be used to constrain gluon TMD PDFs, which are still unknown. Large or small, COMPASS J/ψ TSA results play a unique role in hadron spin-structure studies and can be used to study the J/ψ production mechanisms and features. In order to better understand and test the share between different production mechanisms, the information from J/ψ TSAs would need to be confronted with COMPASS λ measurement results for J/ψ production [81, 82].

It is however important to underline, that in this range the requirement of TMD factorization that the transverse momentum of the dimuon has to be much smaller than $M_{\mu\mu}$, is satisfied less strictly compared to the Drell-Yan channel, due to lower $M_{\mu\mu}$.

4.1.1 J/ψ mass range data selection and analysis

The analysis is carried out for the dimuon data collected during Drell-Yan data-takings in 2015 and 2018. For this measurement, the 190 GeV/c π^- beam from the CERN SPS was scattered off the COMPASS transversely polarized NH_3 target with proton polarization $\langle P_T \rangle \approx 0.72$ and $J\psi$ dilution factor $\langle f \rangle \approx 0.15$, where the latter accounts for the fraction of polarizable nucleons in the target and the migration of reconstructed events from other regions into each target cell. The polarized target, placed in a 0.6 T dipole magnet, consisted of two longitudinally aligned cylindrical cells of 55 cm length and 4 cm in diameter, separated by a 20 cm gap. The two cells were polarized vertically in opposite directions, so that data with both spin orientations were recorded simultaneously. In order to compensate for acceptance effects, the polarization was reversed approximately every two weeks. The entire data-taking time of each year was divided into nine periods, each consisting of two consecutive weeks with opposite target polarizations. The proton polarization had a relaxation time of about 1000 hours, estimated from NMR measurements performed for each target cell in each data taking period. A 240 cm long alumina structure with a tungsten core, placed downstream of the target, acted as a hadron absorber and a beam dump. Outgoing charged particles were detected by a system of tracking detectors in the two-stage spectrometer. In each stage, the muon identification was accomplished by a system of muon filters. The trigger required the hit pattern of LAST and OT hodoscope planes to be consistent with at least two muon candidates originating from the target region. For any pair of them, this implies that the laboratory polar angle θ_μ of each candidate lies in the first stage ($25 < \theta_\mu < 160$ mrad), or one candidate lies in the first stage and the other one in the second stage of the spectrometer ($8 < \theta_\mu < 45$ mrad).

Going through the main aspects of the data analysis:

- A basic pre-filtering of the data has been applied before the processing. Short or obviously problematic runs have been excluded from the production run-lists. The final processing of 2015 and 2018 data was carried out at the Frontera supercomputer. Presented results are based on the final production of both 2015 (s2 slot) and 2018 (t8 slot) data samples profiting from all recent reconstruction software (CORAL) developments, alignment and calibration improvements, etc. In particular the analysis of 2018-t2 production data pointed out several problems with P04 period (*e.g.* 30% loss of high-mass statistics compared to t1), hodoscope mapping problems, etc., which were fixed in the t8-slot.

- Data quality and event selection. The data were scrutinized by stability and quality tests via monitoring of various macro, kinematic and angular observables. Spills and runs showing instabilities were filtered into so-called 'bad spill/run' lists and rejected from the analysis. The bad spill and run analyses have been redone for 2015-s2 and 2018-t8 samples separately. Both data sets were treated on the same ground (software, settings, criteria). To large extent the event selection procedure and criteria were the same as the ones used in the published DY 2015 data [83], the main difference being the mass range 2.85 $< M_{\mu\mu}/(\mathrm{GeV}/c)^2 <$ 3.4. The requirement that both muons have momenta larger that 7 GeV/c applied in high-mass Drell-Yan analyses is not applied for this work (based on MC checks). As in all other Drell-Yan analyses the data from the P00 period of 2018, which were taken in unstable conditions, have not been included in the analysis.

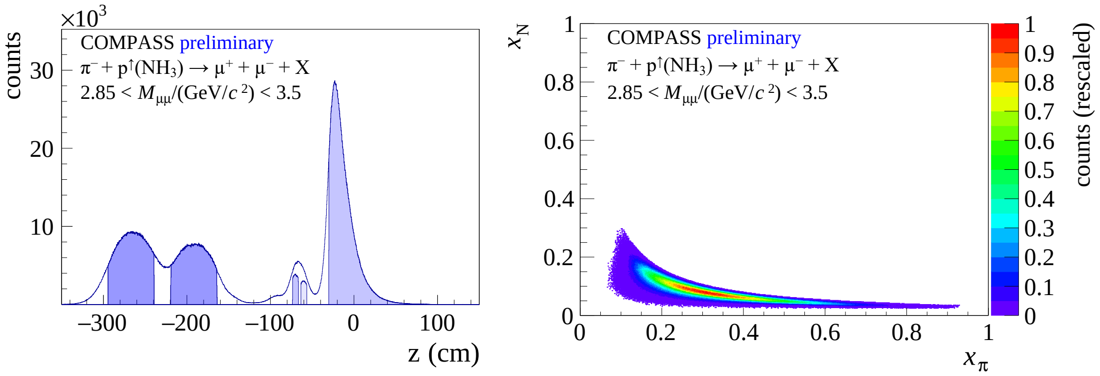

Fig. 34: Vertex Z-position distribution (left) and x_N versus x_π distribution (right panel) for J/ψ mass range.

After all selections, about 1.6×10^6 dimuons remained for the analysis in the 2015 sample and 1.7×10^6 dimuons in the 2018 data set. In Figs. 34–35 various kinematic distributions are shown for merged sample of both years. In Fig. 36 kinematic maps for 2015 and 2018 are compared; they look identical. However, we note that some of the angular correlations look slightly different in 2018 compared to 2015 (e.g. ϕ_{μ^+} vs ϕ_S), which points to minor acceptance differences between the two years. This however is not expected to impact the TSAs.

As it was reported in 2022 annual report [39], in high-mass Drell-Yan analysis several observables including the TSAs have pointed to differences between first (P01-P04) and second (P05-P08) halves of the 2018 data. The J/ψ TSAs results did not show any similar problems. The results from 2015 and 2018 samples are well-compatible and periods compatibility doesn't unveil any significant instabilities within separate years.

- Monte-Carlo, target polarization and dilution factor. For unpolarized analyses of 2018 data extensive Monte-Carlo studies were carried out using samples generated with TGeant COMPASS setup simulation

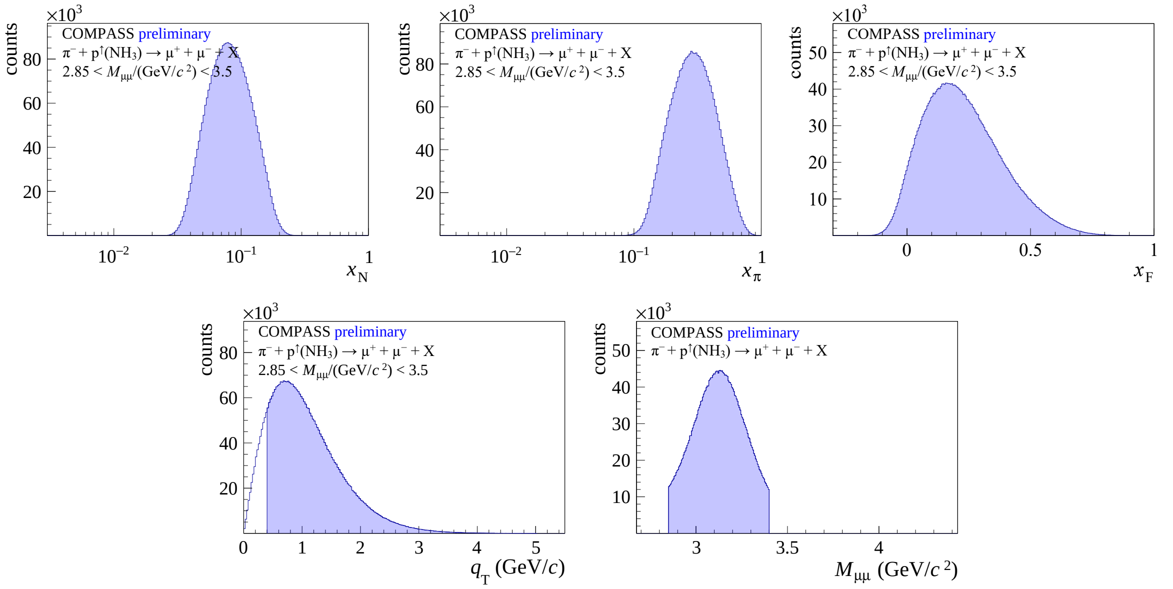

Fig. 35: Kinematic x_N, x_π, x_F, q_T and $M_{\mu\mu}$ distributions for J/ψ mass range.

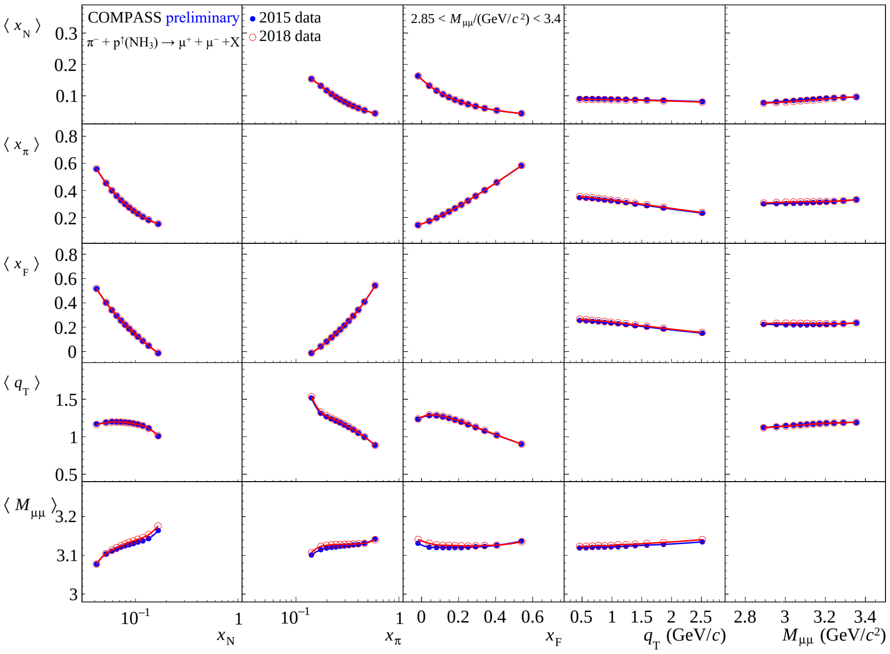

Fig. 36: Kinematic map: J/ψ mass range NH_3 target, 2015 and 2018 data.

tool. Produced 2018 MC sample was used in the TSA analyses in order to: i) determine the resolutions and acceptance for angular and kinematic variables, ii) estimate background contamination, iii) estimate cell-to-cell and "surrounding material"-to-cell event-mixing, iv) estimate the impact of various detector and trigger-slab instabilities at the level of kinematic and angular variables. In Fig. 38 the cell-to-cell and "surrounding material"-to-cell event-mixing is illustrated for different kinematic bins. Mixing fractions are quoted for each kinematic bin and were taken into account in the dilution factor evaluation.

Given that in 2015 the setup was operating in a very similar to 2018-run conditions, the outcome of those studies was applied for both years. The dilution factor and feed-down fraction were calculated within the parton Reggeization approach [84–86], which interpolates smoothly between low and high energies and provides a reasonable description of the J/ψ p_T spectrum. The calculations were done separately for 2015 and 2018 target configurations (packing factors). Average dilution factor values (already corrected for event-mixing) calculated for 2015 and 2018 samples and feed-down coefficients are shown in Fig. 37 as a function of kinematics.

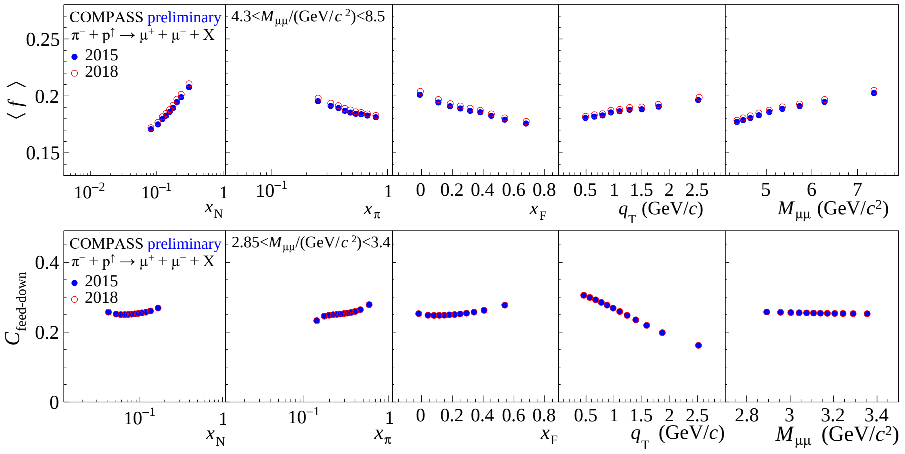

Fig. 37: Top: Average dilution factor values as a function of kinematic variables (2015 and 2018 data). Bottom: feed-down contribution to the J/ψ sample.

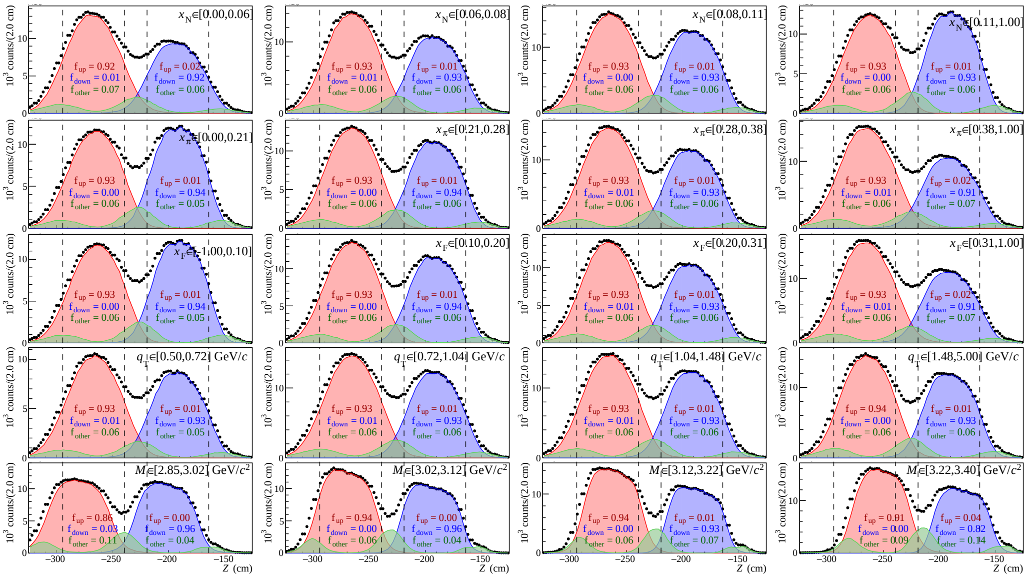

Fig. 38: Reconstructed Z vertex distribution. Different colors indicate different origins.

- Systematic tests. The TSAs resulting from different periods were checked for possible systematic effects. Usually, the largest systematic uncertainty contribution is due to a possible residual variations of experimental conditions within a given period. They are quantified by evaluating various types of false asymmetries. A number of other tests were performed checking the statistical consistency of the data and stability of the obtained results w.r.t. different cuts and selections. Evaluated additive systematic uncertainties amount to 0.7-0.8 $\times\sigma_{stat}$ to both 2015 and 2018 TSAs. The normalization uncertainties originating from the uncertainties on target polarization (3%), dilution factor (10%) and $A_U^1 = 0$ assumption (5%) were taken into account when merging the results from 2015 and 2018.

- Extraction of the asymmetries and evaluation of the systematic uncertainties. Asymmetries were extracted using three methods: 1D "Double Ratio" (1DDR), "Extended Unbinned Maximum Likelihood (UML)" and "Extended Unbinned Maximum Likelihood with event-by-event $f \cdot D_{[f(\theta_{CS})]}$ - weighting" (EWUML) [87]. All three methods yield the same results and no systematic deviations were observed. In both UML approaches all TSAs are extracted simultaneously together with the corresponding co-variance matrices. Using EWUML takes into account kinematic $f \cdot D_{[f(\theta_{CS})]}$ corrections in a most proper event-by-event way and allows to slightly decrease the statistical uncertainties of the TSAs compared to the 1DDR and UML methods. In present analysis the extraction has been restricted only to twist-2 terms in the cross-section Eq. 24. The asymmetries have been extracted separately for the 2015 and 2018 data sets. The combined asymmetries are obtained by evaluating a weighted sum of the results from two years considering the additive and multiplicative systematic uncertainties evaluated separately for each year. The procedure follows the recipe used in SIDIS analyses.

In Figs. 39 the final combined results from two years are presented as a function of kinematic variables. The asymmetries have been extracted in the mass-range between 2.85 (GeV/c)^2 and 3.4 (GeV/c)^2 using EWUML method in bins of x_N, x_π, x_F, q_T and $M_{\mu\mu}$. The systematic point-to-point uncertainties are found to be about 0.7-0.8 times the statistical uncertainties and given in the form of bands. The obtained results suggest that non of the TSAs in J/ψ mass-range exhibits any strong signals or kinematic dependences and all measured TSAs are compatible with zero within available statistical precision.

To summarize, COMPASS performed first ever measurement of TSAs in pion-nucleon interactions in the mass range of J/ψ meson. The fact that the asymmetries are small and compatible with zero within 0.5%-1% statistical precision needs a careful consideration. COMPASS SIDIS TSA measurements at a similar hard scale have shown non-zero effects both for Sivers and Collins asymmetries [79]. Small or zero signal in the pion-nucleon channel may indicate that the production of J/ψ mesons in COMPASS kinematics may indeed go mainly via gluon-gluon channel, as suggested in Ref. [81]. Assuming that gluon TMDs are either small or zero, could then explain our observations. COMPASS results have triggered the attention of phenomenologist working on charmonia TMDs. We plan to start drafting a paper dedicated to J/ψ TSAs after the publication of the results for Drell-Yan channel.

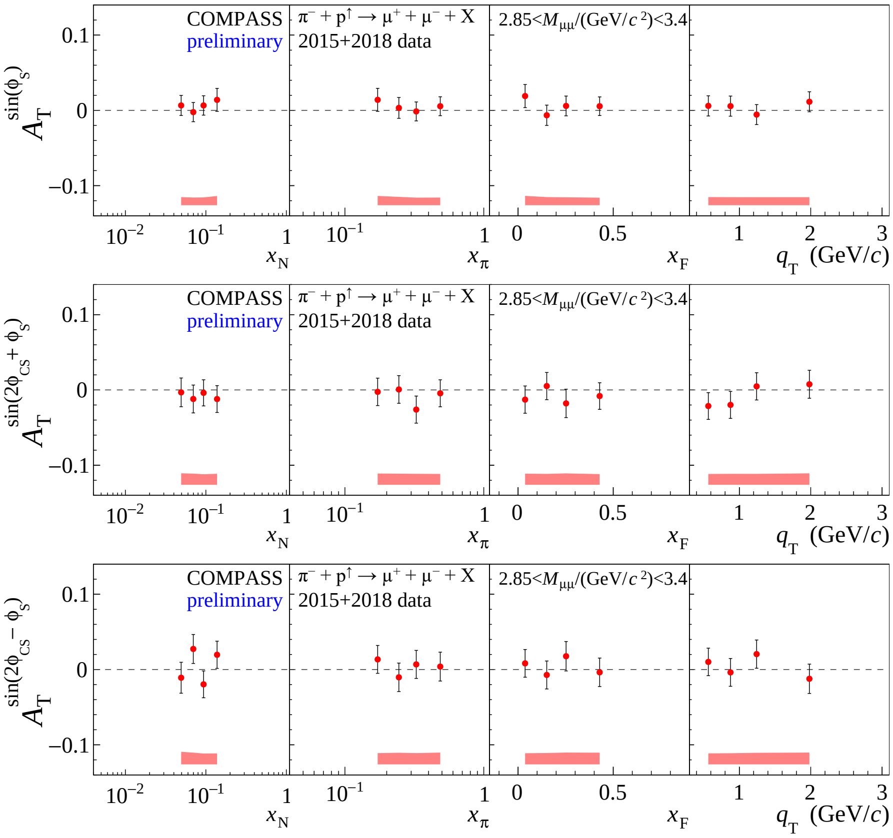

Fig. 39: From top to bottom: kinematic dependence of Sivers, pretzelosity and transversity TSAs.

4.2 J/ψ production cross-section ratios W/Al

The results on J/ψ production cross section measured from the COMPASS data taken in 2018 were released in August 2022. We studied cold nuclear matter (CNM) effects occurring when the charmonium is produced from a nuclear target, evaluating the ratio of J/psi production in tungsten and aluminium targets. The CNM effects may originate from the nuclear modification of the parton distribution functions (nPDF) of the hadronic target (nuclear shadowing, anti-shadowing, or EMC effect) and partonic energy loss in nuclear media. Quarkonia and Drell-Yan cross sections in small systems like hadron-nucleus (hA) collisions are ideal to study CNM effects, via the so-called nuclear modification factor: $R_{hA}(x_F) = \frac{1}{A}\frac{\mathrm{d}\sigma_{\mathrm{hA}}/\mathrm{dx_F}}{\mathrm{d}\sigma_{\mathrm{hp}}/\mathrm{dx_F}}$, the ratio of cross sections between a heavy and a lighter (or proton) targets. This factor is expected to be equal to unity if no nuclear effects are present. Such measurements were performed both in fixed target and in collider experiments, at various collision energies. In COMPASS the nuclear modification factor was studied for J/ψ production in tungsten versus aluminium targets, as a function of Feynman-x and transverse momentum, at $\sqrt{s}$ = 18.9 GeV.

The double differential cross section for J/ψ production decaying to dimuons as a function of x_F and p_T can be written as follows:

$$\frac{\mathrm{d}^2\sigma^{\pi^-\mathrm{A}}}{\mathrm{dx_F dp_T}} = \frac{\mathrm{N}^{\mu^+\mu^-}_{\mathrm{events}}(\mathrm{x_F},\mathrm{p_T})}{\epsilon^{tot}.\mathrm{BR}.\mathcal{L}} \tag{25}$$

where $\mathrm{N}^{\mu^+\mu^-}$ is the number of J/ψ to dimuon events; ϵ^{tot} the acceptance (including geometric acceptance, detector, trigger, and reconstruction efficiencies); BR the branching ratio of the decay J/$\psi \rightarrow \mu^+\mu^-$; and $\mathcal{L}$ the integrated luminosity. The integrated luminosity is obtained according to:

$$\mathcal{L} = N_{\mathrm{beam}} \times \varrho_T \tag{26}$$

with N_{beam} being the number of incident beam particles and ϱ_T the target density.

The observable to study the CNM effects, nuclear modification factor ($R_{\pi^-A}(x_F, p_T)$), can be calculated as the ratio of the cross section of the heavy (A) to the light (B) nuclei:

$$R_{\pi^-A}(A/B) = \frac{\mathrm{N_A}(\mathrm{x_F},\mathrm{p_T})}{\epsilon^A.\alpha^A.L^A_{eff}.\rho^A} / \frac{\mathrm{N_B}(\mathrm{x_F},\mathrm{p_T})}{\epsilon^B.\alpha^B.L^B_{eff}.\rho^B}. \tag{27}$$

where α^i are the beam attenuation factors at the entrance of each of the considered targets; L^i_{eff} are the effective lengths of the target cells (calculated taking into account the pion interaction length in each material); and ρ^i are the density of target materials. Other parameters entering the cross section cancel out in the ratio, thus there is less systematic error affecting the ratio than the cross sections themselves.

In 2018, dimuon events were collected over approximately 20 weeks, combined in 9 periods. The first period P00 is not considered in this analysis, since it suffered from several spectrometer instabilities and no MC samples could be produced to describe them.

The dimuons originate from a 190 GeV negative pion beam interacting in a sequence of cylindrical targets: two long polarized ammonia cells, followed by a small aluminium cell and by a tungsten beam plug whose first part is considered as a nuclear target. In the J/ψ cross section analysis only the 7 cm long Al target and the first 10 cm of tungsten are used. The selected events fired one of the two dimuon trigger systems: LAS-LAS (when both muons are detected by the hodoscopes of the Large Angle Spectrometer); and LAS-OT (one muon detected at large angle, while the other one is seen by the so-called Outer hodoscopes, in the Small Angle Spectrometer of COMPASS). In this analysis initially the two triggers are treated separately, and the results are combined at the end.

To ensure the stability of the spectrometer, a pre-analysis was performed, as described in previous reports [39], and the identified bad spills and runs were rejected. The event selection includes several quality criteria for the reconstructed tracks and validation of the fired trigger, as well as a so-called ”image cut”, that ensures the same acceptance for both charges of muons. A set of requirements is applied to the reconstructed kinematics: $0 < x_F < 0.9$, $p_T < 4$ GeV/c. After these selections, 1.18 million dimuons from W and 0.2 million dimuons from Al with masses $M > 1.5$ GeV/c^2 remain.

The detailed evaluation of the acceptance is required in this analysis. This is done per target, trigger and period. The period dependence is simulated by using trigger efficiency and detector efficiencies which were extracted on a period by period basis [5]. The procedures for detector and trigger efficiencies extraction were described in detail in previous reports. The acceptance is determined in (p_T, x_F) bins, from a dedicated Monte Carlo simulation of the charmonium production process. The process is generated using Pythia 8 and the spectrometer full events simulation is done by the means of TGeant, a Geant4-based COMPASS setup simulation tool. In Figure 40 the acceptance is shown as a function of p_T in bins of x_F, for LAS-LAS trigger (top panel) and LAS-OT trigger (bottom panel), for W (red) and Al target (blue).

---

[5] For the moment, detector efficiency sets corresponding to only two periods were extracted. In this analysis the one obtained from P03 was applied to the simulations of the first four periods, and the one obtained from P08 applied to the last four periods.

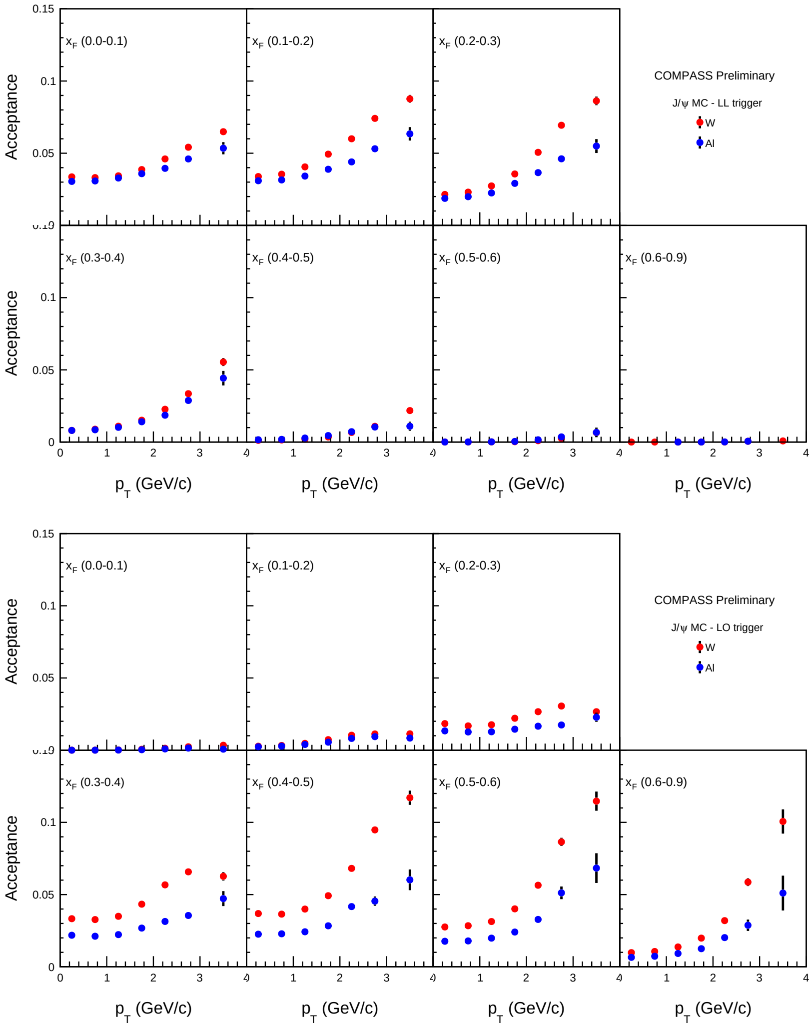

Fig. 40: Acceptance of J/ψ events as a function of p_T and in bins of x_F, for LAS-LAS (top) and LAS-OT (bottom) dimuon triggers. The red points are for W target and blue points for Al target.

Besides the J/ψ, several other physics processes contribute to the dimuon mass spectrum. The combinatorial background from uncorrelated muon pairs also contributes to the measured distribution. Thus, in order to correctly evaluate the number of J/ψ particles in each (p_T, x_F) bin, as required by equation 27, the so-called ”cocktail” fits of the mass spectra are performed. The following physics processes are considered:

- J/ψ production
- $\psi(2S)$ production
- Drell-Yan
- Open-charm semi-leptonic decays

Dedicated Monte Carlo samples corresponding to each of these processes are generated in Pythia 8 and propagated through a Geant4 simulation of the spectrometer, being reconstructed afterwards as in the case of real data. The combinatorial background, is obtained from the real data like-sign muon pairs recorded simultaneously with the opposite-sign muon pairs (since the trigger system does not distinguish between particle charges, both type of pairs are acquired). Since the equal acceptance of both muon charges was ensured by the ”image cut” referred above, a simple geometrical model can be applied to evaluate the combinatorial of opposite-charge muons from the like-sign muon samples:

$$N_{+-}^{comb} = 2\sqrt{N_{++}N_{--}} \tag{28}$$

In the cocktail fit, the real data dimuon mass distribution is fitted using the sum of reconstructed MC samples for the various contributions. In this fit, the normalization for each process enters as a free parameter (except for the combinatorial background, since this contribution is effectively measured from real data). Figure 41 presents an example of the fit method for the case of W target and LAS-LAS trigger, in bins of p_T, for the $0.1 < x_F < 0.2$ range. The real data is shown as the blue histogram, while colored solid curves present the fitted charmonium resonances J/ψ (magenta) and $\psi(2S)$ (green). The red solid line shows the fit function, while the black dotted line shows the summed background contributions.

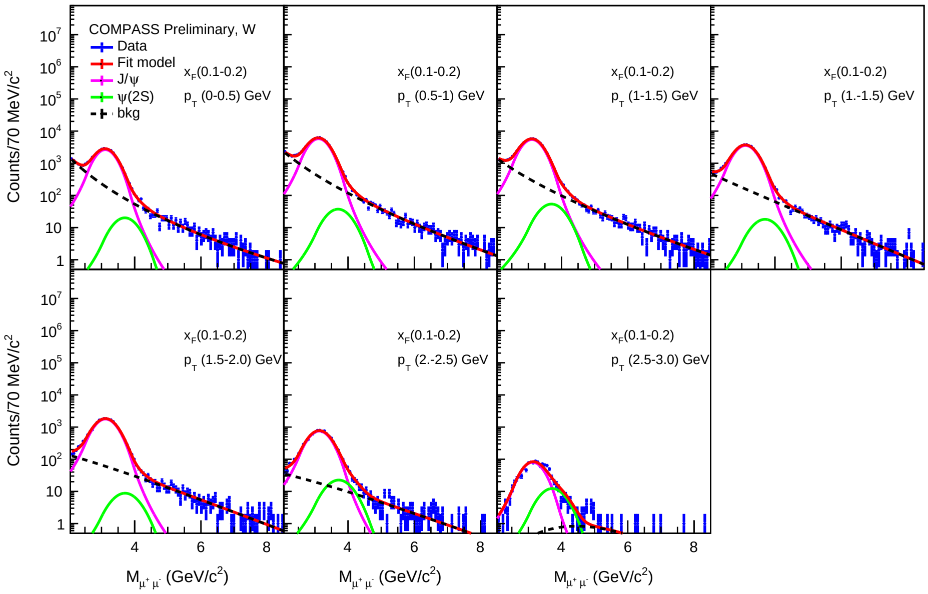

Fig. 41: Example of the fit method to the dimuon mass spectrum, for W target and LAS-LAS trigger, in bins of p_T, for the $0.1 < x_F < 0.2$ range. RD is shown as blue histogram, together with charmonium J/ψ (magenta curve) and $\psi(2S)$ (green curve) contributions. Red solid line shows total fit function, while black dotted line the summed background contributions.

The number of J/ψ particles in each (p_T, x_F) bin is obtained separately per target and trigger from the cocktail fits. When considering the J/ψ events from aluminium, a corrective factor is applied to take into account the contamination of J/ψ events originated in tungsten that are wrongly reconstructed at the aluminium target position. This contamination is due to an event-migration caused by limited vertex Z-position resolution and has strong kinematic dependence. It ranges from 4 to 17% for LAS-OT trigger, and from 1 to 8% for LAS-LAS trigger. The procedure to evaluate this contamination corrective factor is described in last year's SPSC report [39].

The nuclear modification factor $R_{\pi^- A}(W/Al)$ for the ratio W to Al is obtained according to equation 27. A systematic difference between the two triggers is observed, amounting to roughly 5%. Despite a through investigations, the origin of the bias could not be identified. When combining the results from the two triggers, a simple arithmetic mean is used. Other studied sources of systematic uncertainty include the period dependence and the signal extraction method. The total systematic uncertainty on $R_{\pi^- A}(W/Al)$ is estimated to be below 10%.

In Figure 42 the results obtained for the nuclear modification factor are presented in bins of (p_T, x_F), after the two dimuon triggers are combined (the error bars are statistical only). One can observe a suppression at low p_T, that is more prominent at large x_F. These results are qualitatively comparable with those from previous fixed-target experiments E866 and NA3. Since the data from these experiments, as well as from E537 and NA60 (on proton induced J/ψ production) are well described by the partonic energy loss model of Arleo et al [88], these COMPASS results can be interpreted as hint of energy loss effects in cold nuclear matter.

4.3 Drell-Yan cross section

Drell-Yan and deep inelastic scattering are the two main processes giving access to the hadron PDFs that describe the momentum distribution of their constituent quarks and gluons. While proton PDFs are presently known with a good accuracy, the knowledge of pion PDFs is rather scarce. The pion PDFs are being extracted

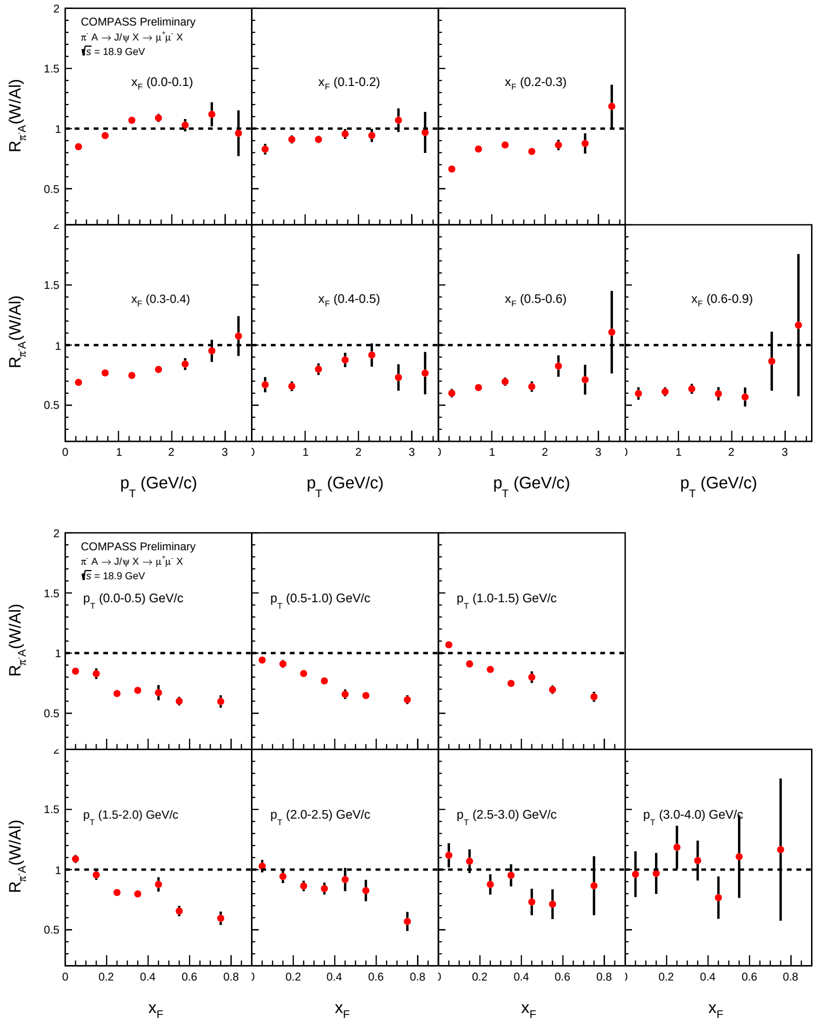

Fig. 42: Nuclear modification factor $R_{\pi^- A}(W/Al)$ in 2D, after combining LAS-LAS and LAS-OT triggers. Only statistical errors are presented.

from pion-induced processes (pion beam collides with fixed nucleon target) like Drell-Yan, J/ψ production, and prompt-γ production. The pion-induced Drell-Yan process is mostly sensitive to the valence quark content in the pion. In COMPASS, a negative pion beam (of purity above 95%) is used, thus in the measured Drell-Yan process there is u-quark dominance.

In parallel with J/ψ analysis, the Drell-Yan high mass range (dimuon with mass $4.3 < M < 8.5$ GeV/c^2) is analysed in order to obtain the differential cross section. The study of Drell-Yan cross section in (M, q_T, x_F) bins is done for all three COMPASS targets (ammonia, aluminium and tungsten).

The cross section is given by $\sigma = N/\mathcal{L}$, where N is the number of measured Drell-Yan events and $\mathcal{L}$ is the luminosity as defined at eq. 26.

Similarly to the J/ψ cross-section analysis, 8 periods from the 2018 data set are analysed (period P00 was excluded, for the reasons mentioned above). The event selection is also very similar to the one used in the J/ψ analysis, but in this case the measurement is done in the ranges $-0.2 < x_F < 0.9$ and $q_T < 3.6$ GeV/c. The total statistics of selected dimuons with $4.3 < M < 8.5$ GeV/c^2 (before purity corrections are applied) in this analysis amounts to 37 thousand from the ammonia target, 6 thousand from the aluminium target and 44 thousand from the tungsten target.

Different processes can yield muon pairs in the final state and can contribute to the dimuon sample. In order to keep a high level of Drell-Yan purity in the sample, the analysis is first restricted to the high mass region ($4.3 < M_{\mu\mu}/(GeV/c^2) < 8.5$), where this process is expected to dominate. In the second step, the purity in this region is evaluated based on the description of the real-data dimuon mass spectrum using a combination of a set of Monte-Carlo samples representing specific dimuon processes and a combinatorial background extracted from real-data like-sign muon pairs, as it was described in the previous sections for the J/ψ analysis.

For each target and in each x_F and q_T bin of the 3D cross-section analysis, a likelihood fit is performed to adjust the normalisation of the various reconstructed Monte-Carlo kinematic distributions to the data. The combinatorial background contribution is kept normalized to unity, as it is obtained from like-sign real data in the same conditions as the opposite sign muon pairs. These cocktail fits to the dimuon invariant mass spectrum are done in the range between 2.4 and 8.5 GeV/c^2.

The migration of events generated in one of the targets that are reconstructed at the position of another one is also taken into account as a contamination contribution, evaluated from Monte Carlo. In particular, it is important for the events in charmonia peak regions. Since mass resolution changes with vertex Z-position the displacement of reconstructed events from downstream locations corresponds to a shift in the resonance peak towards lower masses, while migration from upstream Z_vertex shifts towards higher masses. The contamination in the high mass Drell-Yan due to event migration from one target material into another is evaluated using MC simulations. It amounts to 1.5% in the aluminium (from events generated in tungsten), and 4% in the ammonia mix (from events generated in the Helium volume surrounding the NH$_3$ cells).

Although the Monte-Carlo simulations describe reasonably well the data, the pole position of the charmonia resonances and their mass resolution are not so well reproduced. The mass resolution appears to be overestimated for upstream targets and underestimated for the downstream region. Globally the J/ψ peak in Monte Carlo is found at slightly higher mass compared to RD. In addition, especially in tungsten target, the Monte-Carlo ψ(2S) component is highly suppressed in the fit for many x_F and q_T bins (potentially due to over optimistic resolution in MC).

Fig. 43: Top: "Cocktail fit" to the dimuon invariant mass spectrum, in one kinematic bin for W LAS+LAS on the left and LAS+OT on the right. The values of scaling parameters are given in the plots. Bottom: Purity evaluation based on MC histograms (blue points) and simultaneous fit of MC shapes in blue.

In the cocktail fits to the dimuon mass spectra a cost function is minimized that includes, in addition to the usual likelihood estimator for Poisson distribution, an extra-term to correct for different mass bias in MC as compared to RD. To the bare likelihood, two constraints are imposed, applying: 1) a penalty to the fit whenever the relative contribution of $\psi(2S)$ with respect to J/ψ goes below 2%; and 2) a penalty to the fit whenever the MC fitted in the range $5.5 < M < 8$ GeV/c^2 (where almost pure Drell-Yan is expected) deviates from real data.

The selected starting mass of the cocktail fits is M =2.4 (GeV/c^2), as it was observed it results in reasonable χ^2 values and keeps some sensitivity to open-charm contribution before entering the dominance region of charmonia. The obtained bias parameter is the largest for W target and found to be around 50 MeV/c^2 and the contribution from the penalties to the total χ^2 is at the percent level. The cocktail fit results for two kinematic bins from tungsten target with LAS+LAS and LAS+OT triggers are shown in Fig. 43-top.

Based on the cocktail fit, the purity can be computed as the ratio of Drell-Yan MC component to the sum of combinatorial background and MC components. To remove the fluctuations in the purity evaluation, a simultaneous fit of the purity and MC shape is performed. An example of the final result of the purity for the same two bins of tungsten is shown in Fig. 43-bottom. The purity is rather high for the ammonia target (usually higher than 90% for masses above 4.3 GeV/c^2) and slightly worse for LAS+OT as compared to LAS+LAS triggers. The tungsten target is the one with largest contamination and only for $M > 5.5$ GeV/c^2 the purity of 90% or higher is reached.

The high mass Drell-Yan events acceptance is evaluated in four-dimensions: target position along beam direction Z_{vtx}, dimuon mass $M_{\mu\mu}$, Feynman-x x_F, and dimuon transverse momentum q_T. It is defined as follows :

$$\frac{d\varepsilon_{Acc}}{dZ_{vtx}dM_{\mu\mu}dx_F dq_T} = \frac{dN_{rec}^{MC}\left(Z_{vtx}, M_{\mu\mu}, x_F, q_T\right)}{dN_{gen}^{MC}\left(Z_{vtx}, M_{\mu\mu}, x_F, q_T\right)} \tag{29}$$

where $\frac{d\varepsilon_{Acc}}{dZ_{vtx}dM_{\mu\mu}dx_F dq_T}$ is the 4-dimensional acceptance. N_{gen}^{MC} is the number of generated high mass Drell-Yan events from Pythia8, in a given kinematic bin, but without the impact of experimental conditions. N_{rec}^{MC} is the number of reconstructed events in the equivalent kinematic bin, but evaluated from reconstructed variables. The acceptance of LAS+LAS and LAS+OT events is calculated separately. The acceptance as defined above includes the effects of detector and trigger efficiencies. While it is approximately constant with M and with q_T, it varies significantly in the x_F range considered, as can be seen in figure 44 for the case of the ammonia target.

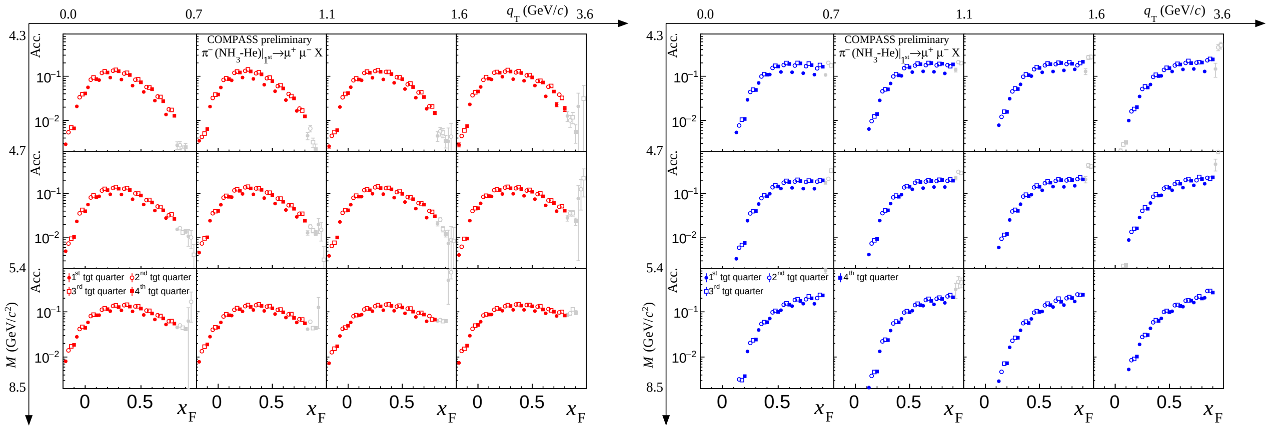

Fig. 44: Acceptance for Drell-Yan events in the mass range $4.3 < M < 8.5$ GeV/c^2 originated from the ammonia target, for LAS+LAS trigger (left) and LAS+OT trigger (right).

In order to obtain the cross sections, beam flux and integrated luminosity are evaluated. The beam flux is calculated using the random trigger events, from the beam tracks reconstructed at the experiment's beam telescope. The average beam intensity during the 2018 Run is 55 MHz. In this analysis only spills with intensity between 45 and 65 million particles per second are considered. The beam flux distribution is shown in fig. 45-left. The integrated luminosity accumulated over the 8 periods of data-taking included in the analysis is shown in fig. 45-right. The integrated luminosity amounts to roughly 4 fb^{-1} for tungsten target, 2 fb^{-1} for the (ammonia+helium) two cells, and 0.5 fb^{-1} for the aluminium target.

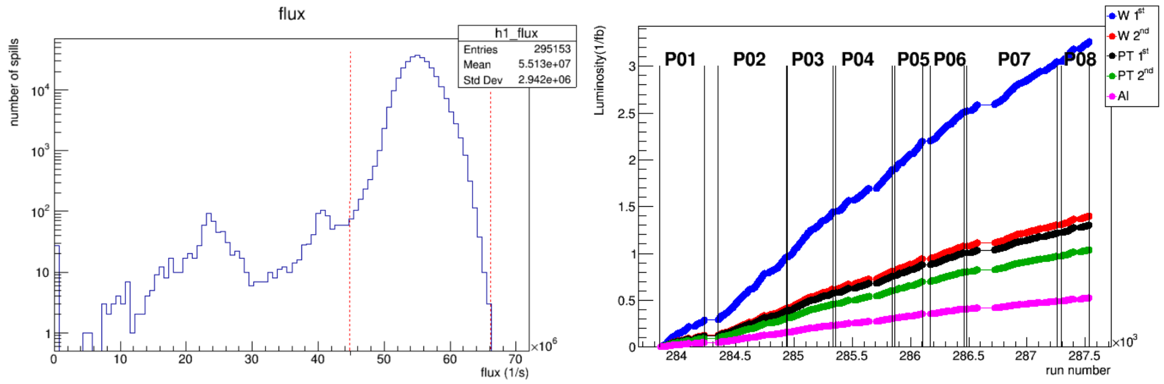

Fig. 45: Beam flux distribution (left) and integrated luminosity along the 2018 Run, per target (right).

The collected data is limited by an average DAQ lifetime of 0.86 . The Veto lifetime, reflecting the fact that a signal from the Veto hodoscopes located at the beam telescope was included in anti-coincidence to the dimuon physics triggers, is also considered. The Veto hodoscopes identify events where muons from beam decays traversing along the beamline (and off the beam spot) occur. The average veto lifetime relevant for LAS+LAS events is 0.74, while for LAS+OT events is 0.67 .

The cross section is evaluated in 3D, 2D and 1D, as a function of the variables x_F, M and q_T. The analysis is done separately for the two dimuon triggers, LAS+LAS and LAS+OT, that can be considered to a large extent independent measurements. The results are compatible between the two triggers, except for the tungsten target, where the LAS+OT cross section is systematically lower with respect to the LAS+LAS one, by 10-20%. As for the J/ψ analysis, it was not possible to identify any of the two triggers as the faulty one, thus the final results are obtained from the arithmetic mean of the two, and a systematic uncertainty related to trigger, amounting to half the difference between measurements, is assigned.

The two polarized target cells are combined evaluating the weighted mean of the two cells results, in order to give a measurement of the Drell-Yan cross section from the unpolarised (since polarisation averaged) ”ammonia + helium” mix.

Figure 46 shows an example of the 3D Drell-Yan cross section per nucleon obtained, in this case from the ammonia target, in bins of mass and q_T, as a function of x_F. The error bars in the points represent the statistical errors, while the bands at each point are the total uncertainties, with statistical and systematic errors added in quadrature. The dominant systematic uncertainties are the ones related to process purity evaluation, and from the acceptance evaluation (specially in the limits of the x_F range considered).

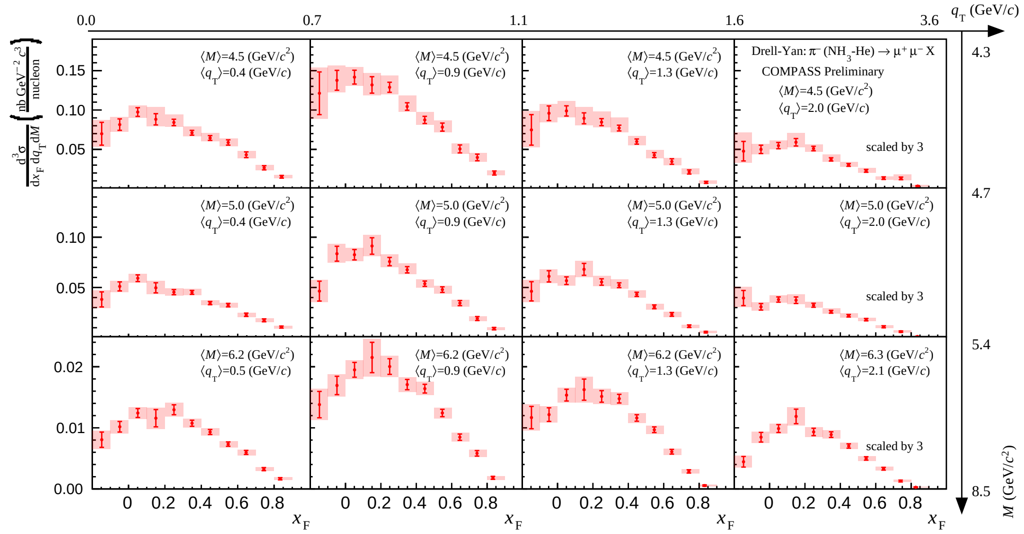

Fig. 46: Three dimensional cross section of DY process as a function of x_F in bins of $(M,\ q_T)$ for ammonia+liquid helium. The vertical lines represent the statistical uncertainties while the shaded areas account for the total uncertainties.

The COMPASS Drell-Yan cross-section results can be compared with those published by past experiments E615 at FermiLab [89] and NA10 at CERN [90]. These experiments used tungsten targets, and similar negative pion beam momenta, of 252 GeV/c in the case of E615, and 194 GeV/c in the case of NA10. Figure 47 shows the comparisons of Drell-Yan cross section from the W target as function of x_F in several $\sqrt{\tau}$ bins ($\sqrt{\tau} \equiv M/\sqrt{s}$) between COMPASS (red points) and E615 or NA10 (blue points) experiments. The scaling factor $M^3/\sqrt{s}$ is applied in order to take into account the different beam energies. In general, COMPASS results are in good agreement with both NA10 and E615 ones, given the systematic and statistical uncertainties. In the comparison to E615, the normalisation of COMPASS data is always higher at the range $0.23 < \sqrt{\tau} < 0.32$ (lower mass bins), but it is at the same level for $0.32 < \sqrt{\tau} < 0.42$ (higher mass region). Comparing to NA10 data, the normalisation is at the same level for all the $\sqrt{\tau}$ bins. These results are not surprising, given the discrepancy reported since long between the results from those two past experiments, at the level of 20%.

The ratio of Drell-Yan cross sections between heavy and light nuclear targets provides an access to cold nuclear effects. Among these, parton energy loss predicts a significant drop of the ratio at very large x_F; while due to Cronin effect the ratio is expected to exhibit a mild increase towards large q_T.

The cross-section ratios for different targets are shown in Fig. 48. Part of the systematic uncertainties are expected to cancel out in the ratio, especially those related to the luminosity and to the acceptance. But since the most significant ones are either from purity or from trigger incompatibility, a large fraction of the systematic uncertainty is expected to propagate to the cross section ratio. The process purity uncertainty is considered to mainly come from the extraction method itself and therefore to be correlated for the various targets. For that reason, the difference of the relative uncertainty of the purity is taken as a systematic uncertainty on the ratio. Concerning the systematics associated to the trigger discrepancy, since it is of unknown origin, the relative systematic uncertainty from each target involved in the ratio is added in quadrature. Given the current size of the systematic uncertainties, the results are mostly insensitive to any nuclear effects.

When Drell-Yan event takes place in a cold nuclear medium, initial state multiple scattering occurs, leading to the so-called Cronin effect. As a net effect, the dimuon q_T distributions appear broader when measured

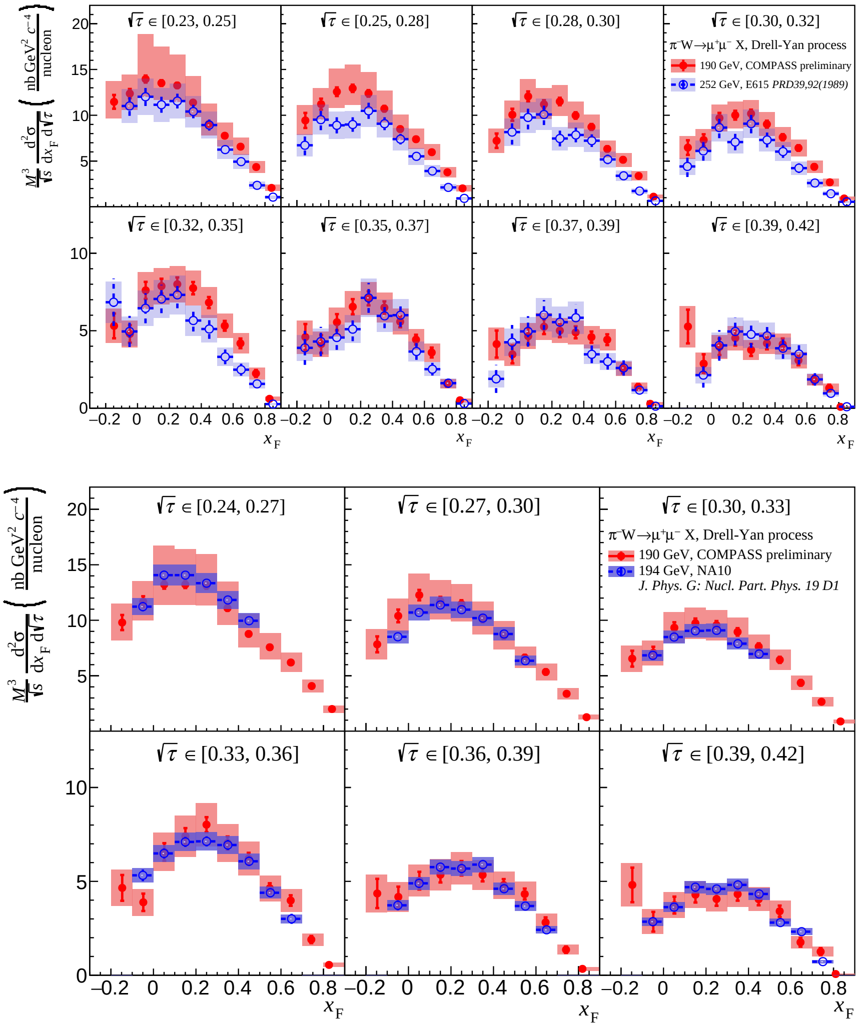

Fig. 47: 2D Drell-Yan cross section measurement from W target as function of x_F in different $\sqrt{\tau}$ bins. Top: COMPASS (red, 190 GeV) versus E615 (black, 252 GeV). Bottom: COMPASS (red, 190 GeV) versus NA10 (black, 194 GeV). The band shows the total uncertainties (systematics are 6.5% for NA10 [91] and 16% for E615 [92]).

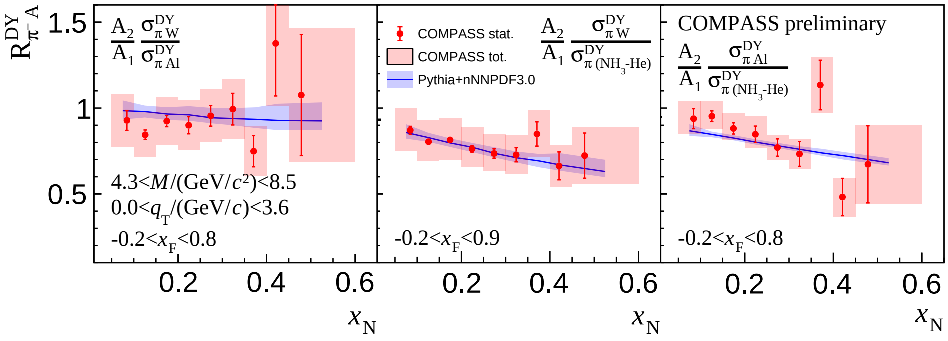

Fig. 48: Ratios of 1D Drell-Yan cross sections between different targets, as a function of x_N. The error bars at the points are the statistical uncertainties while the shaded bands show the total uncertainties. The blue curve shows the theory expectation using nuclear PDFs from nNNPDF 3.0.

from heavier targets as compared to lighter ones. The average ${q_T}^2$ gives a measure of this broadening. The

Drell-Yan cross section distribution as a function of q_T is fitted with a Kaplan function of the form:

$$\frac{1}{2q_T}\,\frac{d\sigma}{dq_T} \;=\; p_0\,\left(1+\frac{q_T^2}{p_1^2}\right)^{-6}. \tag{30}$$

The $\langle q_T^2 \rangle$ is then given by:

$$\langle q_T^2\rangle \;=\; \frac{1}{\int \frac{d\sigma}{dq_T}dq_T}\int q_T^2\,\frac{d\sigma}{dq_T}dq_T \;=\; \frac{p_1^2}{4} \tag{31}$$

Figure 49 presents the average q_T^2 for ammonia and tungsten targets, as a function of x_F. It is clearly larger for the heavier target than for the lighter one.

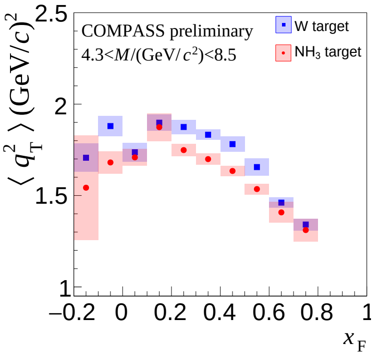

Fig. 49: $\langle q_T^2\rangle$ of PT cells and W target as a function of x_F.

The Drell-Yan cross section results from COMPASS were first presented at conferences during the month of September 2023. The corresponding paper is being prepared.

4.4 q_T-weighted Drell-Yan TSAs

The spin-dependent asymmetries in both SIDIS and Drell-Yan processes involve convolution integrals of TMD functions over intrinsic quark transverse-momenta, k_T. The transverse momentum of the Drell-Yan dilepton evolves from the sum of the individual transverse momenta of the annihilating quark and antiquark that originate from the colliding hadrons. In the context of the observed asymmetries, this leads to a convolution integral involving the associated quark PDFs. In order to de-convolute the encoded TMD obejcts from the asymmetry data, in various phenomenological extractions it is necessary to make model dependent assumptions on a specific functional form (commonly a Gaussian function), to characterize the inherent k_T^2 dependence of the PDFs. More than twenty five years ago an alternative method was proposed to extract k_T^2 integrated transverse moments of the TMDs without making any assumption on the functional form of the transverse-momentum dependence [93–95]. The method, suggests measuring the so-called hadron transverse momentum (or dilepton transverse momentum, in case of Drell-Yan) weighted asymmetries, instead of the conventional ones. Defining the appropriate weights for the asymmetries, the convolution integrals transform into products of k_T^2 moments of the TMDs, which makes the interpretation of the weighted asymmetries notably straightforward. COMPASS published the results for the measurement of P_T-weighted Sivers asymmetries in SIDIS back in 2018 [96].

For the Drell-Yan case we define the weighted transverse spin asymmetries (wTSAs) using appropriate powers of the dilepton's transverse momentum q_T. In the context of the TMD approach, The weighted Sivers asymmetries can be written as:

$$A_{\mathrm{T}}^{\sin\phi_S \frac{q_T}{M_{\mathrm{p}}}} = -2\frac{\sum_q e_q^2\left[f_{1,\pi}^{\bar{q}}(x_\pi)\,f_{1\mathrm{T}}^{\perp(1)q}(x_N)+(q\leftrightarrow\bar{q})\right]}{\sum_q e_q^2\left[f_{1,\pi}^{\bar{q}}(x_\pi)\,f_{1,\mathrm{p}}^{q}(x_N)+(q\leftrightarrow\bar{q})\right]}, \tag{32}$$

while and for transversity wTSA we have:

$$A_{\mathrm{T}}^{\sin(2\phi-\phi_S)\frac{q_T}{M_\pi}} = -2\frac{\sum_q e_q^2\left[h_{1,\pi}^{\perp(1)\bar{q}}(x_\pi)\,h_{1,\mathrm{p}}^{q}(x_N)+(q\leftrightarrow\bar{q})\right]}{\sum_q e_q^2\left[f_{1,\pi}^{\bar{q}}(x_\pi)\,f_{1,\mathrm{p}}^{q}(x_N)+(q\leftrightarrow\bar{q})\right]}, \tag{33}$$

where the sums over quarks and antiquarks q; e_q are the fractional electric quark charges; $M_{\pi,p}$ are the pion and proton masses; and $f^{(n)}$ or $h^{(n)}$ are the n-th k_T^2-moments of the TMD PDFs.

In 2017 the COMPASS Collaboration released preliminary results based on 2015 DY data and in 2019 this was complemented by adding a portion of 2018 data. The current analysis is based on the complete sample of 2015 + 2018 data, like for the conventional TSAs. The Sivers and transversity wTSAs are shown in Fig. 50. Presented results were released in June 2023.

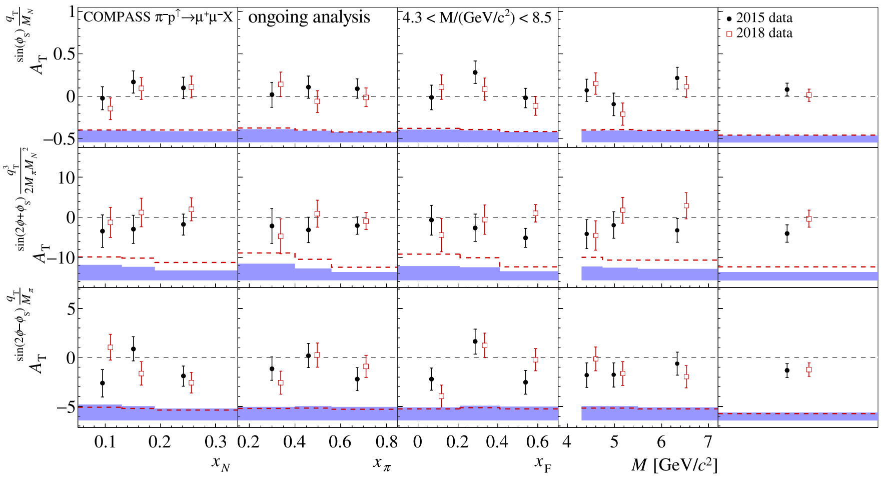

Fig. 50: The q_T-weighted transverse spin asymmetries from the 2015 and 2018 datasets. Systematic uncertainties are denoted by the bands at the bottom.

Drell-Yan wTSAs obtained from the 2015 and from the 2018 data sets are found to be compatible, which allowed to determine the combined asymmetries, as illustrated in Fig. 51.

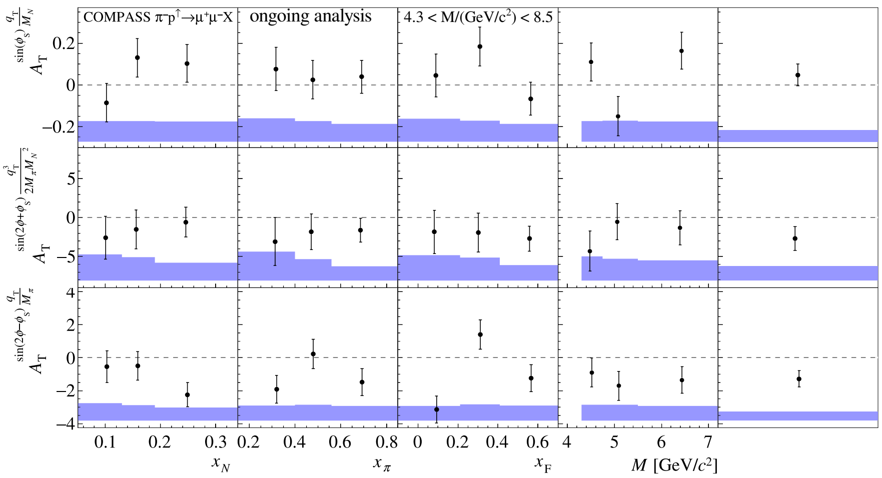

Fig. 51: The q_T-weighted transverse spin asymmetries from the 2015 and 2018 datasets combined. Systematic uncertainties are denoted by the bands at the bottom.

Presently, systematic tests are ongoing, in view of releasing results on pretzelosity-induced wTSA as well. After that, we plan to extract the first moments of the Sivers and Boer-Mulders functions and publish the results (the paper-draft is in an advanced state).

4.5 Other analyses

Other Drell-Yan and charmonium-related ongoing analyses had less relevant progress in the past year, mostly due to established priorities. The final results from the conventional Drell-Yan TSAs that were released in 2021 are being prepared for publication. While the drafting of the paper is well-advanced, the estimation of background level affecting the Drell-Yan mass range is still being worked on, as explained above. We explore a possibility to enlarge the mass range for TSA analyses to 4.0 GeV/$c^2 < M_{\mu\mu} <$ 9.0 GeV/c^2compared to our previous publication [83], where stricter requirements on the invariant mass range were applied: 4.3 GeV/$c^2 < M_{\mu\mu} <$ 8.5 GeV/c^2. At lower masses the background contamination is defined by the contributions from $\psi\prime$, J/ψ, semi-muonic open-charm decays and combinatorial background, while the region above 9.0 GeV/c^2contains Υ-resonances. Based on Monte-Carlo studies, the background contribution in the enlarged mass range was estimated to be about 12%, while with previous selection we were below 4-5% contamination [83]. In the first mass bin (4.0 GeV/$c^2 < M_{\mu\mu} <$ 4.36 GeV/c^2) the estimated background fraction is about 30%. It rapidly drops to 6% in the next mass bin (4.36 GeV/c^2 $< M_{\mu\mu} <$ 5.12 GeV/c^2). As a function of other kinematic variables (x_π, x_N, x_F and q_T) the contamination stays around or below 10%. The $\psi\prime$ contribution, is the closest to the selected lower mass limit. Ongoing COMPASS TSA extractions carried out for lower mass regions indicate that in $\psi\prime$, J/ψ and in the intermediate mass intervals the asymmetries are small and compatible with zero within 0.5%-2% statistical precision. Given this, the background contamination in high mass range can be treated as an extra dilution effect. The corresponding weighting factors have been evaluated on an event-by-event basis and included in an overall dilution factor. This change marginally increases the statistical precision of the results and doesn't change qualitatively the TSA results.

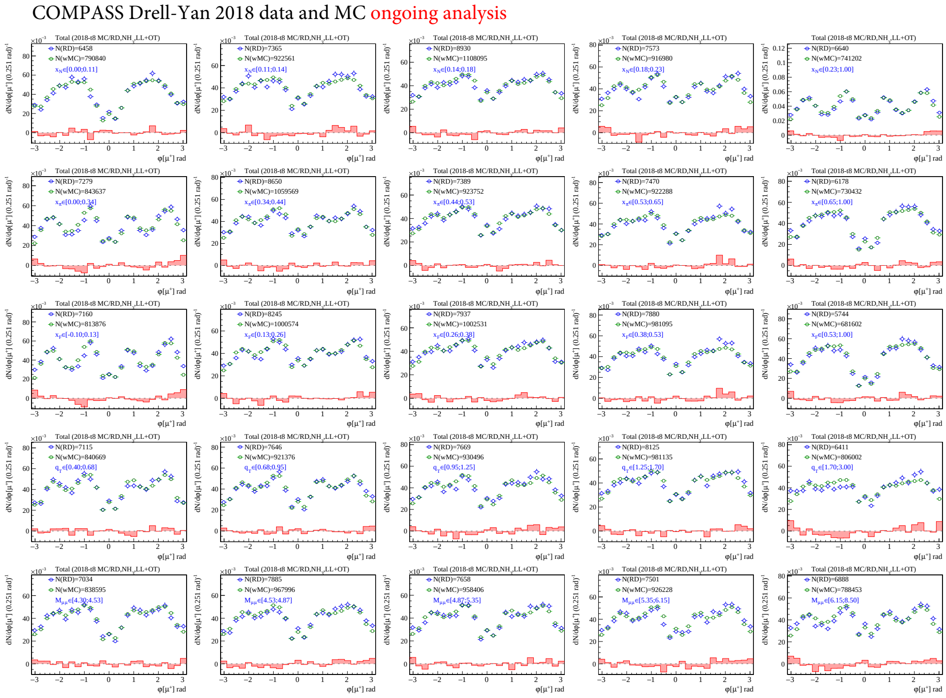

Fig. 52: Drell-Yan 2018 dimuon data comparison with MC: laboratory ϕ-distribution for μ^+ in different kinematic bins. Blue (green) histograms correspond to the real data (normalized MC) distributions, while red histograms show the difference between the two.

The study of the angular dependence of the Drell-Yan and charmonium production, the so-called unpolarised asymmetries are two analyses presenting slow but steady progress. Common issues being addressed in the multidimentional cross-section analyses will bring improvements also to the UA case. The agrement between 2018 data and corresponding Monte-Carlo is being tested and verified in each kinematic bin for angular observables, which may be less critical for the azimuth-independent cross-section studies. In Fig. 52 and example of such a study carried out for ϕ-distribution for μ^+ in different kinematic bins is shown for dimuon sample originating from the NH$_3$ target cells. The overall agreement is satisfactory, but certain regions require a deeper investigation.

Finally, studies on the impact of COMPASS Drell-Yan cross-section results to the global analyses for pion PDF/TMD extraction are being pursued. Two approaches are followed, either using the open source xFitter [97] tools for inclusion of new data to the global fits, or using the MAP (Multi-dimensional Analyses of Partonic distributions) collaboration approach [98] of TMDs extraction. Both are still at a preliminary stage. For this reason, no further details on this promising work are given at this stage.

5 General status of Transverse-spin studies and 2022 data analyses

Several transverse spin related analyses based on COMPASS 2010 proton SIDIS data are still running. Our results on transverse-spin-dependent azimuthal asymmetries of pion and kaon pairs produced in muon-proton and muon-deuteron SIDIS and Collins and Sivers transverse-spin asymmetries in inclusive muoproduction of ρ^0 mesons have recently been published [2], [3]. The description of the measurements was already present in last year's status report [39]. The measurement of the Collins and Sivers asymmetries for ρ^0 production is the first such measurement of a kind and it provides important input for the growing interest towards TMD effects related to vector mesons. The publication of the results for the transverse spin asymmetries for pairs of identified hadrons was expected since some time, and the data have already been used in global analyses. Several activities based on 2010 data have been postponed giving a priority to 2022 data analyses. This concerns several unpublished measurements, in particular: multi-D measurements of transverse spin asymmetries, the measurement of g_2 and the measurement of dihadron Collins and Sivers asymmetries for same-charge pairs (h^+h^+ and h^-h^-). These analyses are planned to be finalised in parallel with the corresponding studies carried out on the 2022 data.

Starting from July 2022, the analysis activities gradually focused on the 2022 data. In parallel to the Run, we started to work on dedicated online data quality tests, first detector alignments, and analysis of small processed data samples. Soon after the end of the Run in November, the systematic work has started on various data preparation, processing and analysis aspects, including: detector calibrations, alignment campaigns, detector performance tests, data quality and stability studies. It was confirmed that the collected data are of a good quality and there are no critical issues that could potentially affect physics results for Collins and Sivers asymmetries. By May 2023, the entire 2022 data sample has been processed with necessary detector calibrations and a reasonable alignment. All required inputs for asymmetry extractions have been delivered (target polarizations, target composition and related dilution factor calculations). The event selection procedures used for 2010 proton data analyses have been revised and adapted to the 2022 sample. The data quality tests have been accomplished and potentially unstable data (about 18% of the total set) was rejected from the overall sample. The asymmetries have been extracted along with a number of systematic tests performed to ensure the stability of the physics results. First encouraging results for Collins and Sivers asymmetries have been presented at the SPIN-2023 conference [99].

As a conclusion, the 2022 Run was a success, and the first physics results have been obtained in a less than one year interval. The corresponding paper is in preparation with the aim to submit it by the end of 2023.

5.1 Introduction: SIDIS cross-section

Hadron leptoproduction in Semi-Inclusive Deep Inelastic Scattering (SIDIS) is the $l\,P \to l'\,h\,X$ process with lepton l scattering off a nucleon P, where l' is the outgoing scattered lepton, h is the detected hadron and X denotes the undetected remainders. As a coordinate system the γ^*N target rest frame is chosen. It is a right-handed coordinate system defined by the lepton transverse momentum direction ($\hat{x}$ axis), virtual photon direction ($\hat{z}$ axis) and respective normal vector ($\hat{y}$ axis). The schematic picture of the SIDIS framework is shown in Fig. 53 (left panel).

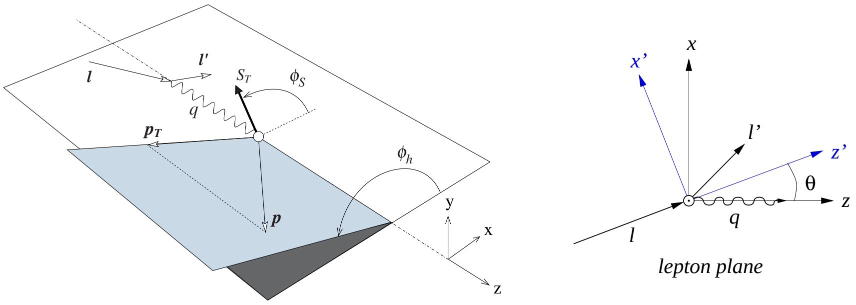

Fig. 53: Left panel: SIDIS process framework and definition of azimuthal angles ϕ_h and φ_S. Right panel: Transition from γ^*N to ℓN (lab) system.

Adopting standard SIDIS notations (see Refs. [71], [40]), the variables used to describe the process are the following ones:

M, m	target nucleon and incoming lepton masses
$P = (M, 0)$	4-momentum of the target nucleon
$l = (E, \mathbf{l}), l' = (E', \mathbf{l}')$	4-momentum of incoming and scattered leptons
$q = l - l'$	4-momentum of the virtual photon (γ^*)
$Q^2 = -q^2$	Negative squared 4-momentum transfer (photon virtuality)
$\nu = \frac{P\cdot q}{M} \overset{lab}{=} E - E'$	Energy of the virtual photon
$y = \frac{P\cdot q}{P\cdot l} \overset{lab}{=} \frac{\nu}{E}$	Fractional energy of the virtual photon
$x = q^2/(2P \cdot q)$	Bjorken scaling variable
$W^2 = (P + q)^2$	Squared invariant mass of the photon-nucleon system
$p = (E, \mathbf{p})$	4-momentum of the final state hadron
p_T	transverse component of the hadron momentum in the $\gamma^* N$ system
$z = \frac{P\cdot p}{P\cdot q} \overset{lab}{=} \frac{E}{\nu}$,	Fractional energy of the observed final state hadron
S_T, P_T (S_L, P_L)	transverse (longitudinal) target polarization in $\gamma^* N$ and lab systems
λ	longitudinal beam polarization

In the experiment, the target is polarized in the lab frame and thus the longitudinal or transverse polarizations (P_L and P_T) are defined with respect to the laboratory $\hat{z}$-axis (*lepton beam* direction) while, for the theoretical description of $\gamma^* p$ subprocess, the *virtual photon* momentum serves as a natural basis. The key difference is that while the values of P_L and P_T are determined by the experimental setup and are fixed, the S_L and S_T depend on the kinematics of each given event. In COMPASS kinematics, laboratory longitudinal P_L and transverse P_T polarizations are very close to S_L and S_T defined in $\gamma^* N$ system. The conversion from $\gamma^* N$ to ℓN (lab) system is illustrated in Fig. 53 (right panel). As one can see, the two coordinate systems are related via a rotation about $\hat{y}$ axis by the θ-angle [100]. Applying the aforementioned transition to the $\gamma^* N$ system, leads to a non-zero longitudinal component of the target polarization which, in turn, induces two new modulations in the cross-section and a mixing of longitudinal and transverse spin dependent amplitudes [100]. The size of those contaminations is defined by the value of $sin(\theta)$ factor, which is rather small in COMPASS kinematics and so the contaminations are mostly negligible. In the current analysis we neglect those effects and adopt the standard SIDIS cross-section and the set asymmetries.

In the $\gamma^* N$ system, the SIDIS cross-section for transversely (w.r.t. lepton beam) polarized target, in a single photon exchange approximation, can be written in a following model-independent way [71], [40]:

$$
\begin{aligned}
\frac{d\sigma}{dx\,dy\,dz\,p_T^h\,dp_T^h\,d\phi_h\,d\psi} &= 2\left[\frac{\alpha}{xyQ^2}\frac{y^2}{2(1-\varepsilon)}\left(1+\frac{\gamma^2}{2x}\right)\right]\left(F_{UU,T}+\varepsilon F_{UU,L}\right) \\
\times\Bigg\{ & 1+\sqrt{2\varepsilon(1+\varepsilon)}A_{UU}^{\cos\phi_h}\cos\phi_h+\varepsilon A_{UU}^{\cos(2\phi_h)}\cos(2\phi_h)+\lambda\sqrt{2\varepsilon(1-\varepsilon)}A_{LU}^{\sin\phi_h}\sin\phi_h \\
&+S_L\left[\sqrt{2\varepsilon(1+\varepsilon)}\sin\phi_h A_{UL}^{\sin\phi_h}+\varepsilon\sin(2\phi_h)\,A_{UL}^{\sin(2\phi_h)}\right] \\
&+S_L\lambda\left[\sqrt{1-\varepsilon^2}A_{LL}+\sqrt{2\varepsilon(1-\varepsilon)}\cos\phi_h A_{LL}^{\cos\phi_h}\right] \\
&+S_T\Big[A_{UT}^{\sin(\phi_h-\phi_S)}\sin(\phi_h-\phi_S)+\varepsilon A_{UT}^{\sin(\phi_h+\phi_S-\pi)}\sin(\phi_h+\phi_S-\pi)+\varepsilon A_{UT}^{\sin(3\phi_h-\phi_S)}\sin(3\phi_h-\phi_S) \\
&\qquad+\sqrt{2\varepsilon(1+\varepsilon)}A_{UT}^{\sin\phi_S}\sin\phi_S+\sqrt{2\varepsilon(1+\varepsilon)}A_{UT}^{\sin(2\phi_h-\phi_S)}\sin(2\phi_h-\phi_S)\Big] \\
&+S_T\lambda\Big[\sqrt{\left(1-\varepsilon^2\right)}A_{LT}^{\cos(\phi_h-\phi_S)}\cos(\phi_h-\phi_S) \\
&\qquad+\sqrt{2\varepsilon(1-\varepsilon)}A_{LT}^{\cos\phi_S}\cos\phi_S+\sqrt{2\varepsilon(1-\varepsilon)}A_{LT}^{\cos(2\phi_h-\phi_S)}\cos(2\phi_h-\phi_S)\Big]\Bigg\}
\end{aligned}
$$

where $\varepsilon = (1 - y - \frac{1}{4}\gamma^2 y^2)/(1 - y + \frac{1}{2}y^2 + \frac{1}{4}\gamma^2 y^2)$ is the ratio of longitudinal and transverse photon fluxes and $\gamma = 2Mx/Q$. The angles ϕ_h and ϕ_S are the azimuthal angles of the produced hadron and of the nucleon spin, correspondingly, see Fig. 53 (left panel)). The $A_{XY}^{w(\phi_h,\phi_S)}$ target longitudinal- and transverse-spin-dependent asymmetries (LSAs and TSAs, respectively) are defined as the amplitudes of the azimuthal modulations $w(\phi_h, \phi_S)$ divided by the effective proton polarization($f \cdot \langle S_T \rangle$)[6] and corresponding depolarization factor [7]. The asymmetries are described as ratios of the corresponding structure functions to the unpolarized one $A_{XY}^{w_i(\phi_h,\varphi_S)} \equiv F_{BT}^{w_i(\phi_h,\varphi_S)}/F_{UU}$. Here, the subscript X stands for the lepton polarization (either U-unpolarised, or L-longitudinal), while Y indicates the target polarization state (U-unpolarised, L-longitudinal and T-transverse). The target transverse polarization dependent part of this general expression contains eight azimuthal modulations in the ϕ_h and ϕ_S. Five TSAs which depend only on S_T are referred to as Single-Spin Asymmetries (SSA). The other three depend both on S_T and λ beam longitudinal polarization and are known as Double-Spin Asymmetries (DSA).

Four TSAs marked in red in Eq. 5.1 originate from the structure functions which are at leading order (LO) in an expansion in Q^{-1}. Within the leading order QCD parton model approach they can be interpreted as convolutions of leading-twist (twist-2) TMD PDF and FFs:

$$
\begin{aligned}
&A_{UT}^{\sin(\phi_h-\varphi_S)} \propto f_{1T}^{\perp q} \otimes D_{1q}^{h}, \quad A_{UT}^{\sin(\phi_h+\varphi_S)} \propto h_1^{q} \otimes H_{1q}^{\perp h}, \\
&A_{UT}^{\sin(3\phi_h-\varphi_S)} \propto h_{1T}^{\perp q} \otimes H_{1q}^{\perp h}, \quad A_{LT}^{\cos(\phi_h-\varphi_S)} \propto g_{1T}^{q} \otimes D_{1q}^{h}
\end{aligned}
\tag{34}
$$

The first two are the Collins and Sivers asymmetries, which have been measured by HERMES and COMPASS (see Refs. [101–103] and references therein). They are followed by the $A_{UT}^{\sin(3\phi_h-\varphi_S)}$ LO SSA related to $h_{1T}^{\perp q}$ (pretzelosity) PDFs and $H_{1q}^{\perp h}$ Collins FF and the Kotzinian-Mulders $A_{LT}^{\cos(\phi_h-\varphi_S)}$ LO DSA providing access to the g_{1T}^{q} Kotzinian-Mulders (worm-gear-T) parton distribution functions.

The remaining four asymmetries are the so-called "higher-twist" (HT) effects. Corresponding structure functions contain terms at sub-leading order in Q^{-1} which involve a mixture of twist-two and, induced by quark-gluon correlations, twist-three parton distribution and fragmentation functions [104][105].

As discussed in the Addendum to the COMPASS-II proposal [106], the goal of the 2022 data taking was to increase the size of the deuteron data-sample in order to make it comparable with the proton one collected by COMPASS in 2010. Proton data gave rise to a number of publications, in particular on the measurements of transverse spin asymmetries, see e.g. Ref. [73, 102, 103]. The aim of collecting the same amount of data as in the 2010 proton Run, was to measure deuteron TSAs with a superior statistical accuracy (a factor of 0.6 times the statistical uncertainties of the 2010 proton asymmetries) [106]. This, in particular, will bring a significant improvement for the evaluation of the tensor charge of the u and d quarks.

The COMPASS 2022 Run was highly successful. Compared to the projections presented in the proposal, in 2022 we collected significantly higher statistics, though with a lower target polarisation. This two factors nearly compensated for each other, and the present statistical uncertainties align well with the estimations quoted in the Addendum [106].

5.2 Data sample and event selection

COMPASS 2022 SIDIS data-taking was performed using 160 GeV/c longitudinally polarized μ^+ beam impinging on three longitudinally aligned cylindrical (3 cm ⌀) ^{6}LiD target cells (30 cm long upstream and downstream cells and 60 cm long central cell). Neighboring cells were polarized oppositely in transverse direction w.r.t. the beam axis. The polarizations were periodically reversed simultaneously for all three cells (most of the times once every two weeks). The spectrometer and target systems were prepared for physics data-taking in about 1.5 months during the commissioning phase and the data collected between 07 June 2022 and 09 November 2022 (about 22 weeks) were taken in stable conditions, as required by the TSA physics analyses. The data-taking and beam-time sharing schedule closely followed the proposal worked out by the COMPASS collaboration for a synergistic usage of the M2 beamline by COMPASS as the main user and NA64μ, MUonE, and AMBER experiments as alternating users (see the pie-chart in Fig. 54). The COMPASS physics data-taking was divided into 10 "periods", normally formed as two coupled neighboring weeks of data-taking ("sub-periods") separated

---

[6] the dilution factor f describes the fraction of polarizable material in the target and $\langle P_T \rangle$ is the average measured polarization

[7] In Eq. 5.1 depolarization factors are the ε-dependent coefficients standing in front of the asymmetries. We denote them as $D(\epsilon)$

by a polarization reversal. A special care was taken during the data taking to guarantee that the spectrometer was stable during each given period. Acceptance variations between the coupled sub-periods of a given period are a potential source of systematic biases at the level of the asymmetries.

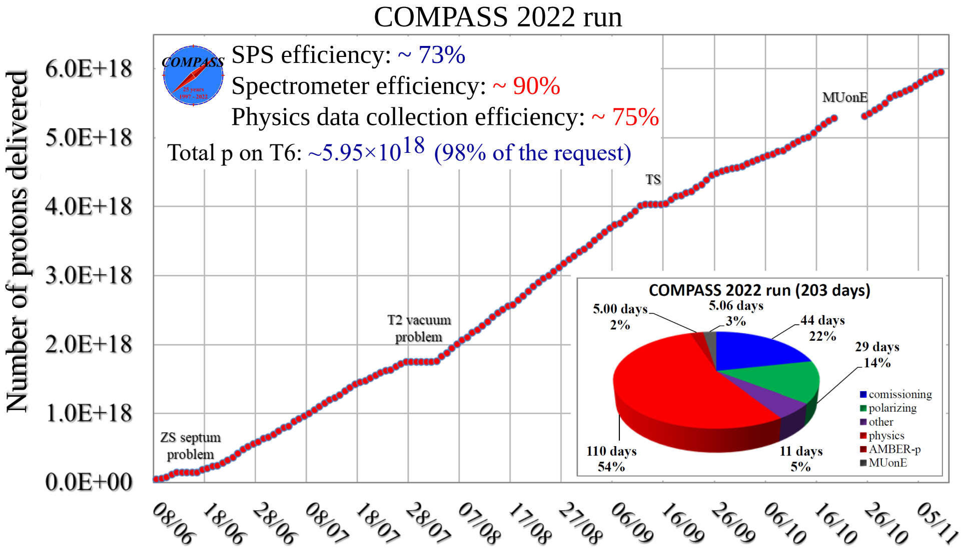

Fig. 54: Cumulative distribution of the number of the protons delivered to T6 production target and pie-chart illustrating the composition of the 2022 data-taking. Bottom panel: Performed physics data collection schedule. The $+-+$ and $-+-$ polarization configurations are indicated by red and blue boxes correspondingly.

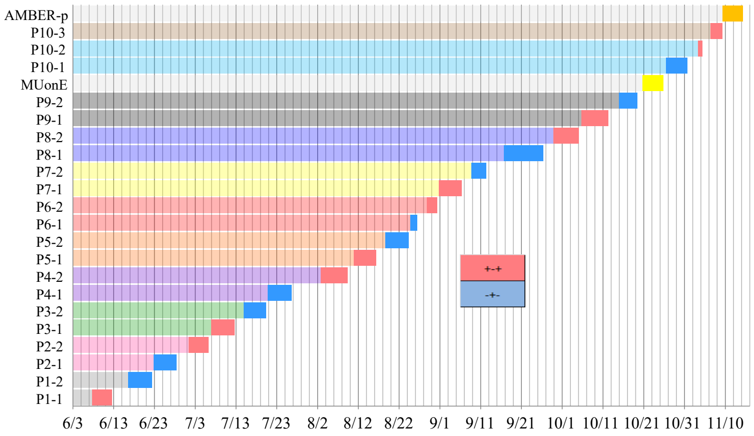

Fig. 55: Performed physics data collection schedule. The $+-+$ and $-+-$ polarization configurations are indicated by red and blue boxes correspondingly.

The analysis was carried out on the full 2022 sample (W01–W10 periods). The current iteration of the data-production is characterized by an improved alignment (e.g. for Straw03 and MuonWall-1 planes) and application of bad channel-cluster rejection. The bad channel-cluster rejection procedure is implemented at the most basic level of data-reconstruction (right after the decoding of detector digits) and is meant to equalize the acceptance conditions between two sub-periods, by rejecting previously identified unstable detector-channel clusters. Unstable or problematic detector channel clusters and hot/missing channels are identified within the scope of the dedicated study that was one of the first stability tests performed while the data were still being collected. Technical channel-profile histograms stored for each detector plane were checked on a run-by-run basis for each data-taking period, and problematic cases were analyzed and listed.

The detector alignment procedure was done with several iterations, making corrections based on the available detector survey information and was repeated e.g. when improved/updated detector calibrations were becoming available, or when specific issues were spotted. The quality of the alignment was controlled by the alignment responsible, using available tools (DPS - detector performance study framework, alignment monitoring framework, hit-residual distributions for detectors etc.). Additionally, alignment quality has been checked looking at the detector pseudo-efficiencies, plain-by-plain hit-residual distributions (on a run-by-run basis) and averaged detector-by-detector hit distributions. The overall quality of the alignment is considered to be reliable and sufficient for the TSA analyses. Known alignment problems (e.g. tensions between MicroMega planes and large area trackers) are currently being addressed and are expected to improve the reconstruction efficiency in the Large Angle Spectrometer in next productions.

Performed data-collection schedule and a pie-chart detailing the share between different stages of the Run are shown in Fig. 55. In particular, one can distinguish short AMBER and MUonE data-taking periods as well as the polarization loss incident in W10 period (the latter is the reason why there are 3 sub-periods marked in W10).

5.2.1 Spill-by-spill and run-by-run data quality and stability monitoring

One of the first checks applied to the reconstructed data is the spill-by-spill monitoring of the stability of a set of macro-variables related to various data-quality aspects such as: the reconstruction performance, the stability of various elements of the setup, data acquisition stability, trigger rates, etc. The aim of the tests is to monitor the global quality of the data, to check the data stability in each given period and to identify potential problems that could introduce systematic differences between the coupled sub-periods. Assuming that the setup and the data-acquisition conditions were stable during the given period of data taking, the chosen variables should be constant in time. A spill is chosen as a time unit[8]. The spill by spill stability checks were performed employing a standalone software package that was developed, used and evolved in the course of various SIDIS and Drell-Yan COMPASS analyses.

In parallel to the bad spill analysis, the data stability has been studied on a run-by-run basis[9]. A set of (in total about 50) relevant variables including:

- kinematic variables such as: x, y, z, p_T, x_F, Q^2, etc.;
- momentum components for the beam particle, scattered muon, produced hadrons and virtual photon;
- laboratory azimuthal and polar angles for the beam particle, scattered muon, produced hadrons and virtual photon as well as physics angles (φ_S, ϕ_h, etc.);
- X, Y and Z coordinates (positions) for the primary interaction vertices and secondary vertices;
- muon and hadron track χ^2, vertex χ^2, average number of hits per track, etc.;

are being monitored and checked for instabilities. This is done separately for each variable, by comparing the mean values and the shapes of the corresponding distributions from all runs in a given period. The run-by-run mean values are monitored separately for each period, comparing the sub-periods with opposite spin configurations. A run is marked as ”bad” if the mean value of a given observable is more than 5 standard deviations away from the overall mean evaluated over the sub-period with opposite spin configuration. Comparison of the shapes of the distributions is done for each pair of runs in the given period using unbinned-Kolmogorov test (UKT) and ”binned” χ^2 and ”ratio fit” tests. Those runs which were found to be incompatible with most of the runs in a given period (yielding p-values close to zero) are marked as bad. These checks were done using event samples build for the entire kinematic range and for various sub-ranges (e.g. for $z > 0.2$ or $x > 0.032$), as well as for different triggers. No significant and systematic differences were found between the results obtained for different samples. While many variables were monitored for instabilities, not all of them were included in the final evaluation of the ”bad” runs. For example, various beam track instabilities and beam momentum variations that can be partially induced by e.g. the thermal effects in the Beam Telescope (BT) detectors, are not affecting the TSA amplitudes under discussion. Final rejection lists are based on SIDIS kinematic variables, vertex Z-position, azimuthal angles (lab and physics) and momentum components of the scattered muon, produced hadrons and virtual photon. This information is then coupled to the results obtained from detector hit-profile monitoring and COMPASS LogBook in order to identify the reason of each instability. Studies have shown that

---

[8] In 2022 SPS slow extracted proton spill (or flat-top), duration within an SPS super-cycle was 4.8 s.

[9] in this context, run is a data sample consisting of up to 200 consecutive spills

spill-by-spill analysis removes most of the problematic data and run-by-run "mean value" monitoring rejects few percent of data if applied after. An example of run-by-run "mean value" monitoring plots illustrating the impact of bad-spill and ban-run rejections is shown in Fig. 56. If the shape-analysis is applied after the bad spill and bad run "mean value" rejections, the impact is found to be marginal (of order of 1%).

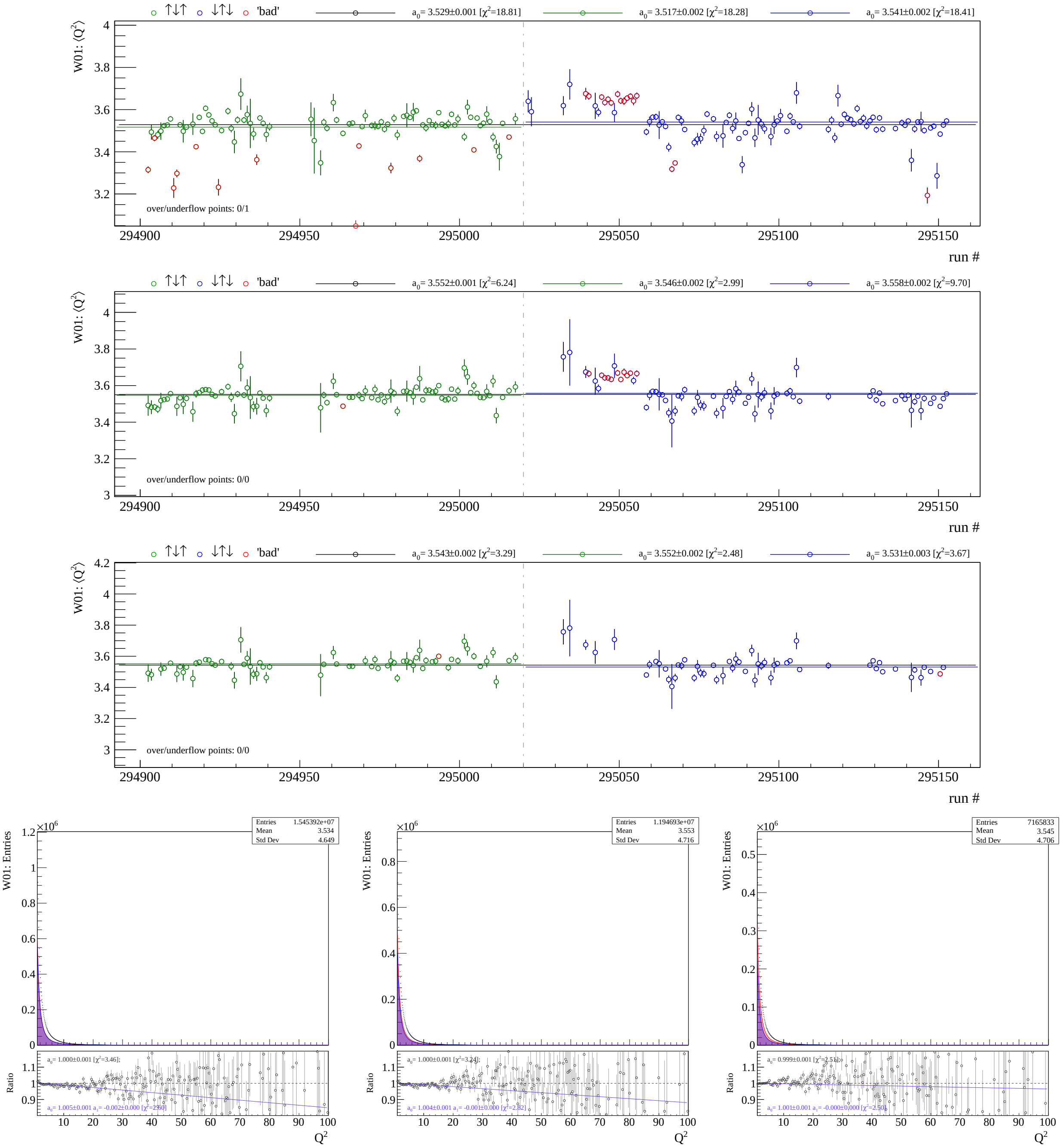

Fig. 56: An example of "bad-run" stability plots: W01 period, Q^2 distribution. Top panel - no bad spill/run rejection applied. Second panel - only bad spill rejections are applied. Third panel - both bad spill and bad run rejections are applied. The "bad" runs are marked in red. The "low-Q^2" bad runs visible in the top panel correspond to Muon Wall-1 station LV-power supply problem that took place during W01 period, while "high-Q2 island" in the beginning of the second sub-period corresponds to PA04 HV issue affecting all planes of the chamber, which resulted in strong reduction of its efficiency. Bottom panel: the Q^2 distribution in the full W01 period (black histogram) and in the sub-periods (red and blue histograms). The sub-period ratio histograms are shown in the bottom sub-pads. From left to right panel: the effect of the "bad spill/run" rejection on distributions and the ratio.

The stability of the K^0 peak position and its width, as well the K^0 production rate (number of K^0 mesons normalized to the number of primary vertices) are one of the standard run-by-run data-stability monitoring tools used in COMPASS SIDIS analyses. In Fig. 57 the K^0 mass peak position shift w.r.t. the nominal PDG mass is shown on a run-by-run basis. There's an overall shift of about 1 MeV w.r.t. the PDG value. The shift remains the same within the periods, which is the most important observation (variations within a period, would be an indication of acceptance variations). However, the shift value slightly changes from one period to another in some cases. The K^0-stability analysis is ongoing and was not yet accomplished at the time of the release. However, it was checked, that after application of bad spill and run filtering, the rejection rate from K^0-stability test is very marginal and insignificant.

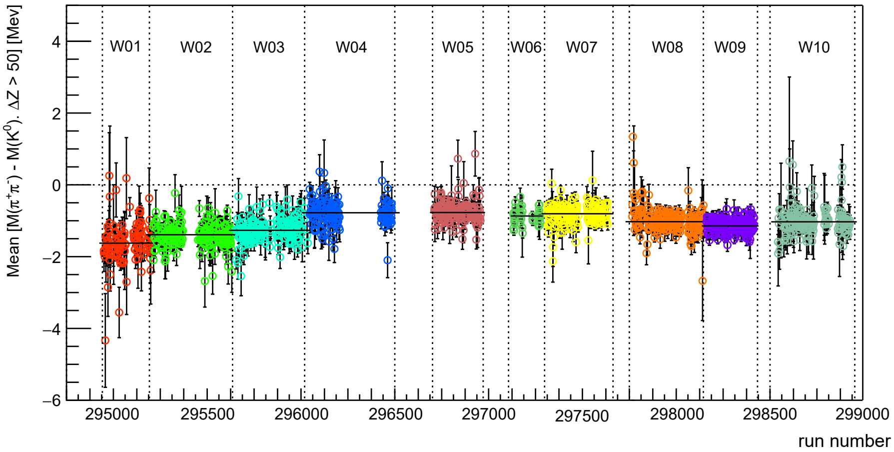

Fig. 57: Monitoring plot for the K^0 mass peak position shift w.r.t. the nominal PDG mass.

The rejection rate with final bad-spill/run lists is at the level of 18% of the total 2022 statistics. It was, however, tested that the rejection doesn't have a significant effect at the level of asymmetries and doesn't bias the physics results.

The stability of the data is checked also at the level of the (sub-)periods. This is done in particular within the ”bad run” analysis framework. For example, in Fig. 56, the plots in the bottom panel illustrate the Q^2 distribution in the full W01 period (black histogram) and in the sub-periods (red and blue histograms). The sub-period ratio histograms are shown in the bottom sub-pads. In Fig. 56 one can in particular see the effect of the ”bad spill/run” rejection on the slope of the ratio histogram (from left to right). A bulk of irregularities is being removed after the filtering and the ratio is stabilizing.

Several other studies are ongoing to tackle alignment issues and detector instabilities. For instance, the so-called hit-residual stability analysis is being performed for all detector planes and allows one to pin down alignment tensions and hardware instabilities. The pseudo-efficiency analysis is being done in parallel for all detectors. Also in this case a particular attention is driven to the sub-period stability, by checking the ratio of the plane-by-plane 2D pseudo-efficiency plots between the two sub-periods of each given period. Another test aiming to identify detector instabilities and alignment issues is the detector hit count study. The normalized detector-hit counts for all planes are checked to be stable within a given period. With this tool, one can disentangle single or multiple planes that have lower hit counts in the given sub-period and can identify the differences between two sub-periods of a given period. Such studies are crucial for testing the alignment and for general understanding of the impact of detector instabilities and related systematics at the level of TSAs.

5.2.2 *Event selection and kinematic distributions*

Due to the similarity of the setups, the event selection procedure used for 2022 data closely resembles the one used for COMPASS 2010 proton analyses. Below the main aspects of the event-selection requirements are listed.

1. Only reconstructed primary vertices with an incoming and outgoing muon tracks and at least one additional associated spectrometer track (hadron candidate) are considered. The vertices are checked to be inside the target volume and to satisfy certain quality criteria (reasonable χ^2, etc.). A dedicated study has been carried our to determine target positions and cuts:

- The upstream cell: $Z \in (-64.9, -34.8)$ cm
- The central cell: $Z \in (-29.7, 0.25, 30.2)$ cm, here $Z = 0.25$ indicates the center of the cell
- The downstream cell: $Z \in (35.2, 65.2)$ cm

The target density plots with clearly visible cells are shown in Fig. 58. A radial cut $R < 1.3$ cm has been applied in order to guarantee that the vertices were reconstructed in the polarized medium.

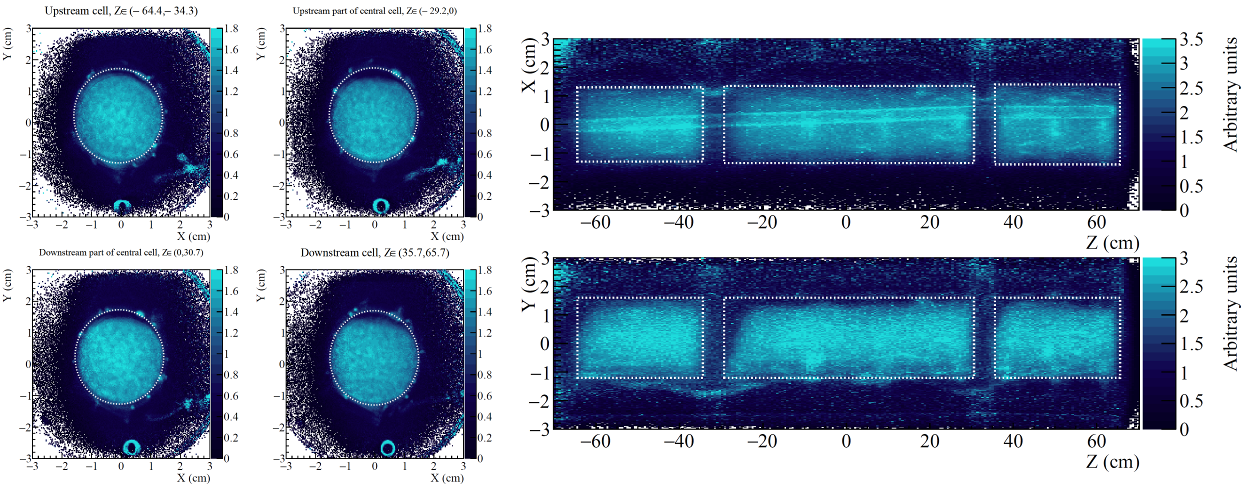

Fig. 58: Target density distribution plots.

2. The reconstructed beam momentum was required to be between 140 and 180 GeV/c and the beam track was checked to satisfy standard quality requirements. In order to equalize the beam flux over the target cells, it was checked that the beam track crossed the most upstream and most downstream surfaces of the cells and crossed the whole target length.
3. The scattered muons have been selected requiring that corresponding tracks crossed at least 30 radiation lengths in the spectrometer. The events with more than one scattered muon candidate have been rejected along with the events where hadron tracks crossing the central hole in the absorbers could be identified as muons. The tracks were checked to have reasonable reduced χ^2 and to have the first recorded hit upstream of SM1 magnet.
4. hadron track candidates were required to satisfy standard quality criteria and to have accumulated less than 10 radiation lengths crossed in the spectrometer. In addition, hadron tracks were checked not to have hits associated in the detector planes located after the Muon Filter-2.
5. Events with recorded “Missing SrcID” errors on key detectors (MicroMegas, Muon Wall 1, MWPCs, etc.) were rejected. Depending on the period, this rejection removes from 6% to 0.5% of the data (overall rejection is below 3%).
6. The kinematic cuts consisted of DIS cuts and hadron cuts. The asymmetries and tests were performed for three hadron z selections: $z > 0.1$ or $z > 0.2$ (current fragmentation regime) and $0.1 < z < 0.2$. Basic requirements ensuring the DIS regime are: $Q^2 > 1$ (GeV/c)^2 and $W > \sqrt{10}$ GeV/c^2 (for $z > 0.1$ and $0.1 < z < 0.2$ ranges[10]) or W >5 GeV/c^2 (for $z > 0.2$ range[11]). Sufficient azimuthal angle resolution was imposed applying $p_T > 0.1$ GeV/c cut on transverse momentum of hadrons. We rejected the events with poorly reconstructed virtual-photon energy ($y > 0.1$) and events with large electromagnetic radiative corrections ($y < 0.9$). Basic kinematics limits on Bjorken x variable ($0.003 < x < 1.0$) have been applied.

After all selections about 100×10^6 (220×10^6) charged hadrons remain for the analysis in the $z > 0.2$ ($z > 0.1$) range. In Fig. 59 the distributions for all main kinematic variables and for azimuthal angle of the

---

[10] as in the ”SIDIS-in-Drell-Yan hard scales” analysis from Ref. [79]

[11] as in the ”conventional’ TSA analysis, see e.g. Ref. [102]

hadrons in the lab ,$\phi_{h,lab}$, are shown. In Fig. 60 the so-called map of kinematic correlations is shown for the events after all selections. This kind of information is particularly useful for calculating the model predictions.

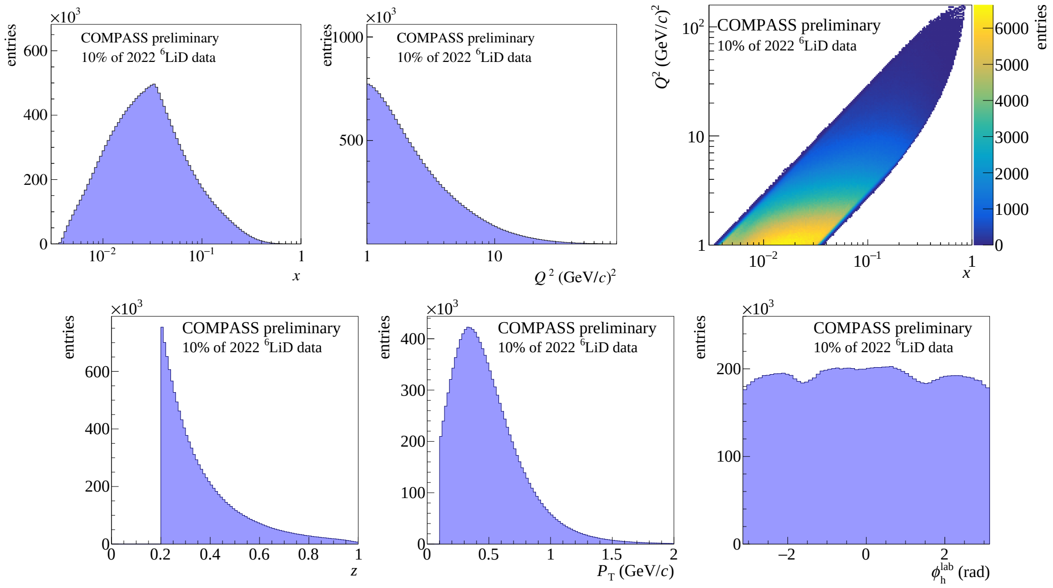

Fig. 59: Top panels, from left to right: DIS x-Bjorken, Q^2 and x:Q^2 event distributions. Bottom panels, from left to right: hadron z, p_T and $\phi_{h,lab}$ distributions.

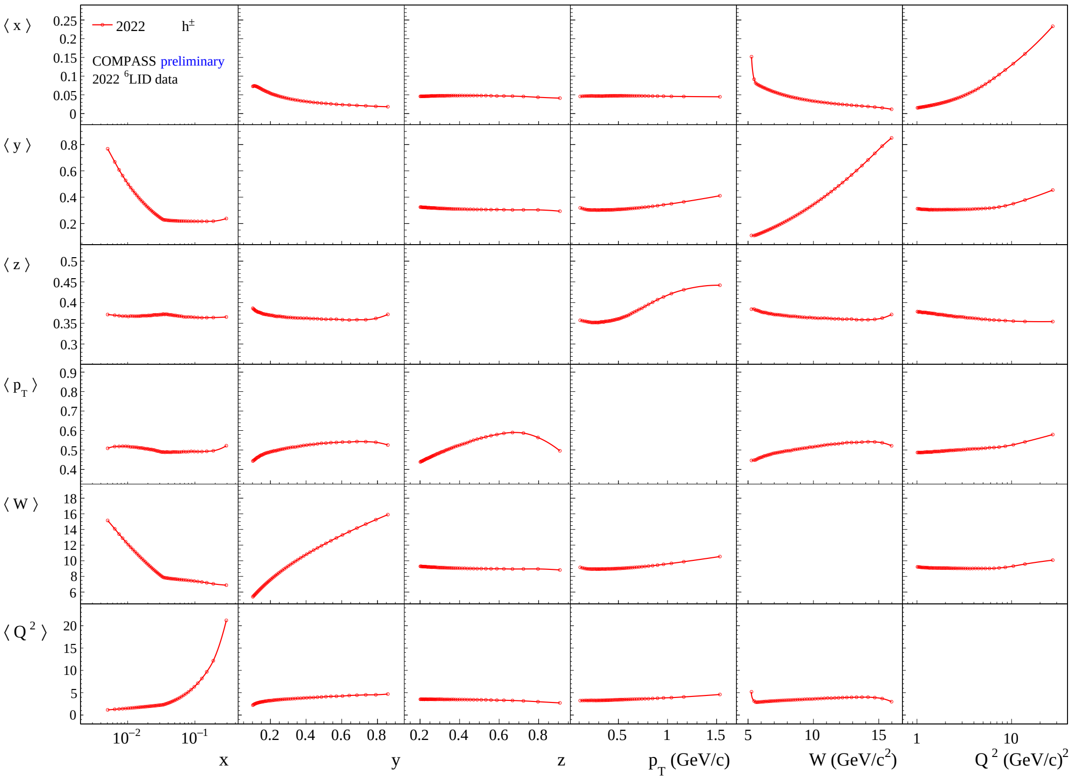

Fig. 60: The ”kinematic map” showing the dependence of averaged kinematic variables.

5.3 Asymmetry extraction

The TSAs are being extracted using an Extended Unbinned Maximum Likelihood (UML) estimator [107]. All eight TSAs and their correlation matrices are being extracted simultaneously. The asymmetries are evaluated separately for positive and negative hadrons in kinematic bins of x, z, p_T or W integrating over all the other variables (one dimensional apparoach). The fitting function is defined by the following EUML-expression in ϕ_h and φ_S:

$$\mathcal{L} = \prod_{c=1}^{n_{cell}} \left\{ \left(e^{-I_c^+} \prod_{n=1}^{N_c^+} P^+(\phi_{hn}, \phi_{Sn}; a_c^+, \vec{A}) \right)^{\frac{\bar{N}}{N_c^+}} \left(e^{-I_c^-} \prod_{m=1}^{N_c^-} P^-(\phi_{hm}, \phi_{Sm}; a_c^-, \vec{A}) \right)^{\frac{\bar{N}}{N_c^-}} \right\}, \tag{35}$$

where $P^\pm(\phi_h, \varphi_S; a_c^\pm, \vec{A})$ is the probability density function, $\sigma(\phi_h, \varphi_S; \vec{A})$ denotes the cross section with $\vec{A}$ as vector of asymmetries defined as:

$$\begin{aligned} P^\pm(\phi_h, \varphi_S; a_c^\pm, \vec{A}) &= a_c^\pm(\phi_h, \varphi_S) \cdot \sigma^\pm(\phi_h, \varphi_S; \vec{A}), \\ \sigma^\pm(\phi_h, \varphi_S; \vec{A}) &= 1 \pm \sum_{i=1}^{8} \langle P_T \rangle f D(y)^{w_i(\phi_h, \varphi_S)} A_{BT}^{w_i(\phi_h, \varphi_S)} \end{aligned} \tag{36}$$

Here $I_c^\pm = \int\int d\phi_h\, d\varphi_S P^\pm(\phi_h, \varphi_S; a_c^\pm, \vec{A})$ is the probability density normalisation coefficient corresponding to the expected number of hadrons, $a_i^\pm(\phi_h, \varphi_S)$ involves the unpolarised cross section, the luminosity and the acceptance seen by hadrons produced in target cell c. The average number of hadrons per kinematic bin is given as $\bar{N}$, while $N_c^\pm$ stands for the number of hadrons with spin up or spin down for target cell c. Number of cells n_{cell} is set to four, following the convention for splitting the central cell into to sub-cells.

The fitting function Eq. 35 is built of $2 \times n_{cell}$ products corresponding to hadrons samples coming from all cells acquired with two (up and down) target spin orientations. Each contribution is weighted with powers of $\bar{N}/N_c^\pm$ in order to account for unbalanced statistics. With series of studies it was proven that within available statistical accuracy and for the given size of the amplitudes, functional form of the acceptance (f.i. Fourier series) has a negligible effect on the extracted TSAs. Hence constant $a_c^\pm$ free parameters are used in the fit, in order to account for unpolarized part and different luminosity in the two sub-periods with opposite target polarisation.

In the UML fit, instead of maximizing the likelihood product, the negative log-likelihood is minimized. The results obtained by UML technique are being traditionally compared to the ones obtained using the 1D Quadruple Ratio method. The asymmetries obtained with the two methods were found to be well compatible and there are no evidences of possible biases. While all eight SIDIS TSA were extracted from the data, for the moment we focus on detailed analysis of Collins and Sivers terms only.

In the asymmetry extraction we used final target polarization values provided by the target group. The average polarization in 2022 was above 40%. In Table 8 the average polarization values per cell are listed for each per period.

sub-period	W01-1	W01-2	W02-1	W02-2	W03-1	W03-2	W04-1	W04-2	W05-1	W05-2	W06-1	W06-2	W07-1	W07-2	W08-1	W08-2	W09-1	W09-2	W10-1	W10-2	W10-3
configuration	+-+	-+-	-+-	+-+	+-+	-+-	-+-	+-+	+-+	-+-	-+-	+-+	+-+	-+-	-+-	+-+	+-+	-+-	-+-	+-+	+-+
upstream cell	39.3	-43.3	-41.3	42.1	39.4	-43.8	-41.4	40.7	40.5	-42	-42.7	39.7	39.4	-39.4	-46.2	39.2	39.2	-43.4	-42.6	40.2	39.6
central cell	-40.6	44.7	43.7	-41.4	-40.5	43.2	42	-41.2	-42.2	43.2	42.5	-37.7	-38.6	41	44.9	-38.7	-39.6	44.9	44.7	-40.3	-36.4
downstream cell	42.8	-42.7	-41.7	44.2	42.7	-42.8	-42.6	42.3	41.6	-41.6	-42.3	40.9	40.5	-39.4	-46.8	40.5	40.2	-41.9	-41.9	42.1	40.8

Table 8: The average polarization values per cell and per period.

The average dilution factor was evaluated to be about 0.35. In Figs. 61 and 62, the kinematic dependences of the dilution and depolarization factors are shown as extracted from the data (with the binning used for asymmetry extraction). The correction for f, $D(\epsilon)$ and target and beam (only for DSAs) polarizations is done using the average value of the product $\langle f \cdot D \cdot P_T \rangle$ (or $\langle f \cdot D \cdot P_T \cdot \lambda \rangle$ for DSAs) evaluated in each kinematic bin for each period.

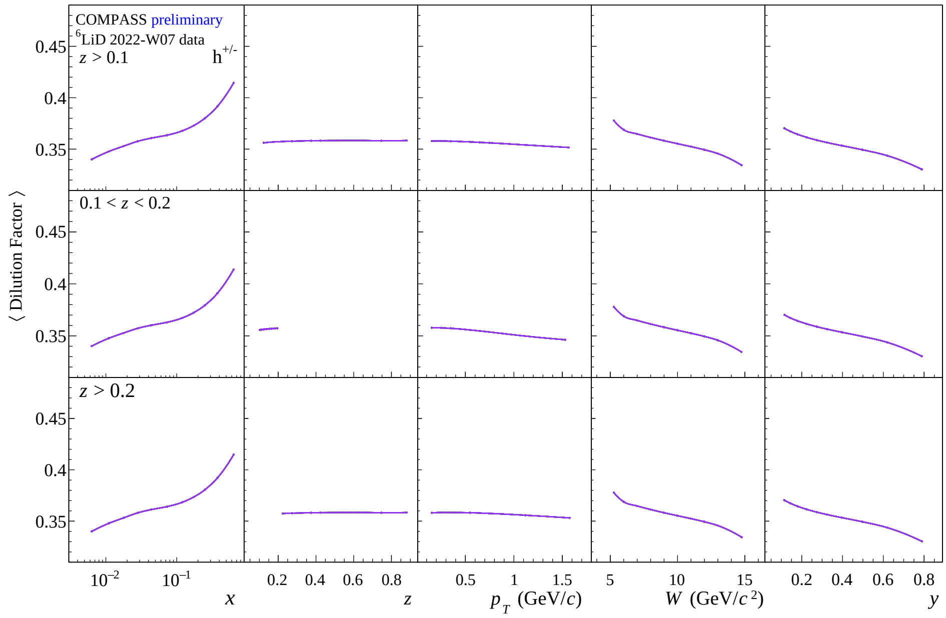

Fig. 61: The kinematic dependence of the dilution factor in the 3 z-ranges.

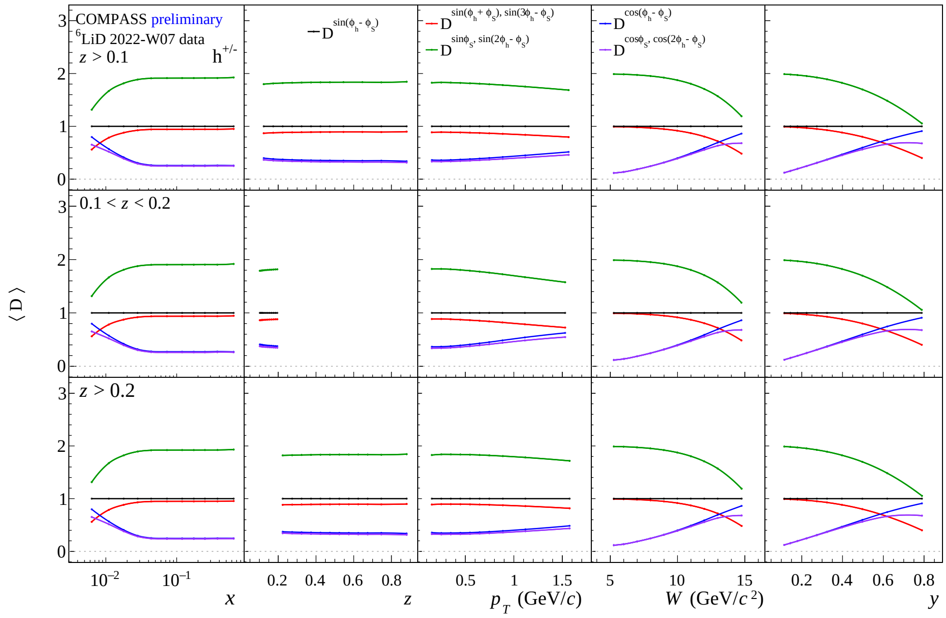

Fig. 62: The kinematic dependence of the depolarization factors in the 3 z-ranges.

5.4 Evaluation of systematics uncertainties

A number of tests have been carried out to check the stability of the physics results. Performed systematic studies and the framework used to evaluate the systematic uncertainties closely resemble the methods and techniques applied for 2010 proton TSAs [79, 101–103]. At first, the impact of the data stability rejections ("bad spill" and "bad run" rejections) was evaluated. Despite the significant number of rejected events (about 18%) no significant changes were observed for the TSAs. Next, the stability of the results across the data-taking has been checked in order to identify possible period to period differences. The compatibility of the results from different time-intervals was checked by comparing the period-by-period asymmetries in different kinematic bins. For Collins and Sivers asymmetries, beside few outlaying points, the results from different periods were found to be well compatible. Some period-to-period instabilities were observed for e.g. $A_{LT}^{cos\phi_S}$TSA. This asymmetry is the most sensitive one to the acceptance variations in the ϕ_S angle distribution. Those variations can be caused, in particular, by instabilities in the incoming or scattered muon detection systems (beam telescope, trigger hodoscopes, trigger-system, muon identification systems, etc.). The latter observation is further confirmed checking the period compatibility pulls, see Fig. 63. Collins and Sivers terms look relatively stable, while there are some indications of tensions (e.g. wider pulls) for the $A_{LT}^{cos\phi_S}$ and less prominently for the $A_{LT}^{sin\phi_S}$ and $A_{LT}^{cos(\phi_h-\phi_S)}$ TSAs, which are also sensitive to ϕ_S-acceptance variations and instabilities (though, to a less extent).

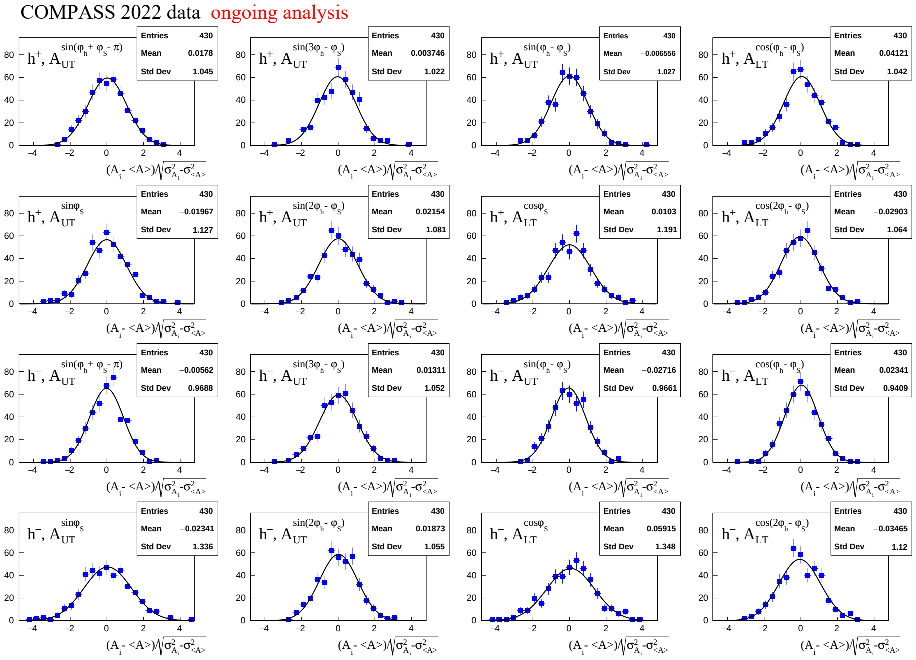

Fig. 63: Period compatibility pulls: results from different periods are compared with the weighted average over the full year. The number of entries in the histograms corresponds to the number of kinematic bins.

One of the key studies used to evaluate systematic uncertainties associated to the TSAs is based on the study of so-called false asymmetries. The data from the upstream and downstream cells in two sub-periods were combined in a way that physics amplitudes cancel, and the estimator remains sensitive only to the modulations induced by the acceptance-variations. Similar false asymmetries were built combining the events from the two halves of the central cell. The false asymmetries are expected to be zero for the Collins, Sivers and other modulations if the acceptance-variations are absent, or cancel out between the cells and sub-periods. It was verified that, indeed, Collins and Sivers false asymmetries appear to be small and well compatible with zero. Some outlying points could be a result of fluctuations or small residual systematic effects in specific kinematic bins.

However, it is important to note that, *per se* small and compatible with zero false asymmetries do not fully guarantee that the physics results are not biased. The false asymmetries are sensitive to specific acceptance variations, which may, or may not contribute to the physics TSAs. For the same reason, non-zero false asymmetries do not necessarily lead to problems at the level of the TSAs. On the other hand, accessing exact acceptance variations that would contribute to the physics amplitudes is impossible since they are indistinguishable and inseparable from the physics signal. Thus, detecting evidences of indirectly related acceptance variations remains the only way to estimate possible systematic biases from the collected data. Due to the complexity of the problem, the information from different tests (period compatibility of TSAs, various false asymmetries, stability of kinematic distributions, etc.) needs to be carefully studied and combined in order to form a comprehensive understanding of the robustness of the physics results.

Another test aiming to identify possible systematic biases is the so-called righ-left-top-bottom (RL-TB) test. For the RL-TB study the TSAs extracted from four sub-samples, corresponding to different spectrometer-acceptance regions over the laboratory azimuthal angle of the scattered muon, are checked to be compatible. The ”Right” and ”Left” samples are defined by only the events with scattered muons falling into the ”Right” and ”Left” hemispheres of the scattered muon acceptance, correspondingly. The ”Top” and ”Bottom” samples are defined analogously. It is expected that ’R-L’ and ’T-B’ TSAs are compatible. For Collins and Sivers asymmetries the outcome of the test was quite reasonable and no critical problems were detected. The effects of possible false asymmetries and 'R-L' and 'T-B" differences affecting the TSAs as well as period-by-period incompatibilities of the results are quantified following the same recipes as for 2010 proton data. The results are summarized in Tab. 9. Since the results from different tests may be correlated, we take the maximal value from all tests as an estimate of the systematic uncertainty. Estimated average systematic uncertainties are about 0.5 times the statistical ones for Collins and Sivers asymmetries.

Collins										
charge	h^+					h^-				
variable	x	z	p_T	W	max	x	z	p_T	W	max
$\sigma_{sys}/\sigma_{stat}$(FA)	0.52	0.42	0.47	0.43	**0.52**	0.44	0.36	0.37	0.4	**0.44**
$\sigma_{sys}/\sigma_{stat}$(RL)	0.41	0.42	0.39	0.42	**0.42**	0.36	0.42	0.42	0.35	**0.42**
$\sigma_{sys}/\sigma_{stat}$(TB)	0.39	0.37	0.44	0.46	**0.46**	0.42	0.37	0.46	0.46	**0.46**
Total $\sigma_{sys}/\sigma_{stat}$ (max)	**0.52**									
Sivers										
charge	h^+					h^-				
variable	x	z	p_T	W	max	x	z	p_T	W	max
$\sigma_{sys}/\sigma_{stat}$(FA)	0.5	0.41	0.5	0.42	**0.5**	0.52	0.49	0.51	0.51	**0.52**
$\sigma_{sys}/\sigma_{stat}$(RL)	0.41	0.47	0.41	0.5	**0.5**	0.24	0.45	0.45	0.38	**0.45**
$\sigma_{sys}/\sigma_{stat}$(TB)	0.4	0.36	0.41	0.36	**0.41**	0.38	0.32	0.44	0.37	**0.44**
Total $\sigma_{sys}/\sigma_{stat}$ (max)	**0.52**									

Table 9: Summary table for evaluated from RLTB and FA tests systematic uncertainties presented in terms of statistical uncertainties.

5.5 Results for TSAs

In this section we present current results obtained for Collins and Sivers TSAs using full 2022 sample. In Figs. 64 and 65 the 2022 results are compared with COMPASS old deuteron measurements of 2002-2004 [101].

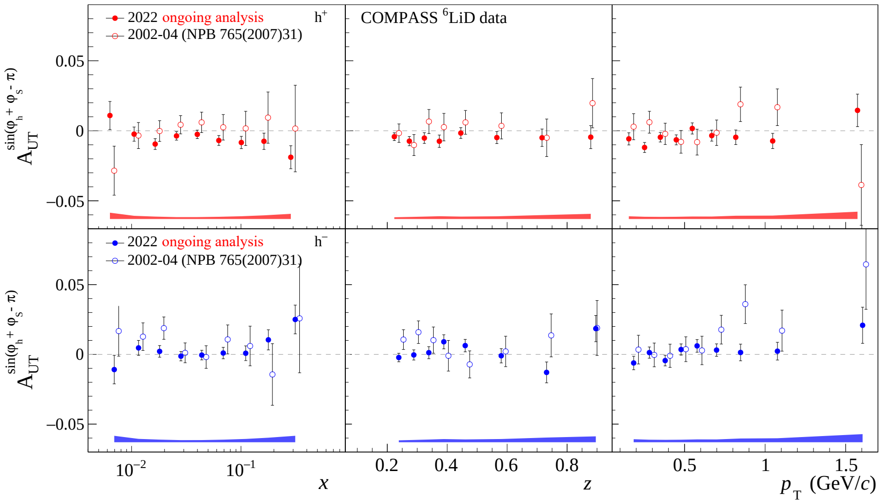

Fig. 64: Collins asymmetry: old deuteron results [101] and current results for 2022 data.

Obtained data is highly precise and matches our estimations done at the time of the proposal [106]. The statistical precision is much higher compared to the old data and is sufficient to distinguish tiny effects even in bins of Bjorken-x above 0.1, at the periphery of COMPASS phase-space coverage, where the statistics is relatively small. In particular, there appears to be a non-zero trend both for positive and negative hadrons at large x for Collins asymmetry (see Fig. 64). New COMPASS data will play a particularly crucial role to constrain d-quark transversity TMD PDF and will remain unique SIDIS deuteron measurements for next decades to come. Observed trends are in agreement with the model predictions, tuned on COMPASS proton/deuteron data [108], as demonstrated in Fig. 66.

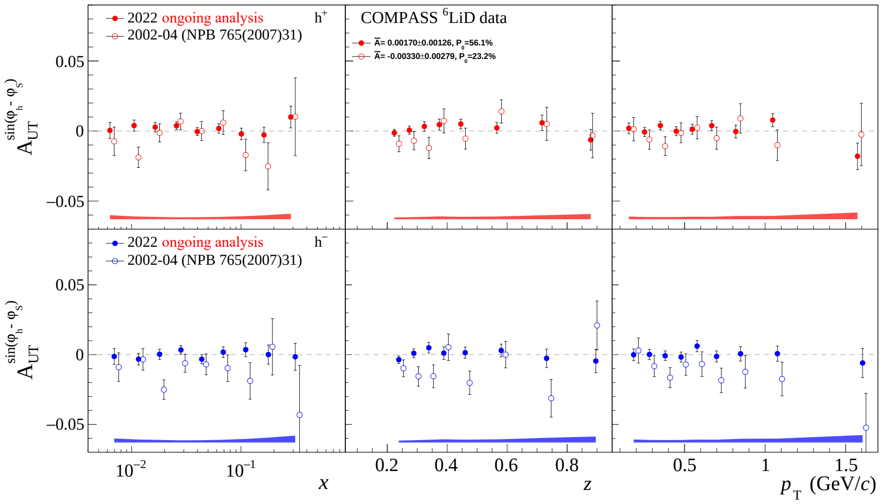

Fig. 65: Sivers asymmetry: old deuteron results [101] and current results for 2022 data.

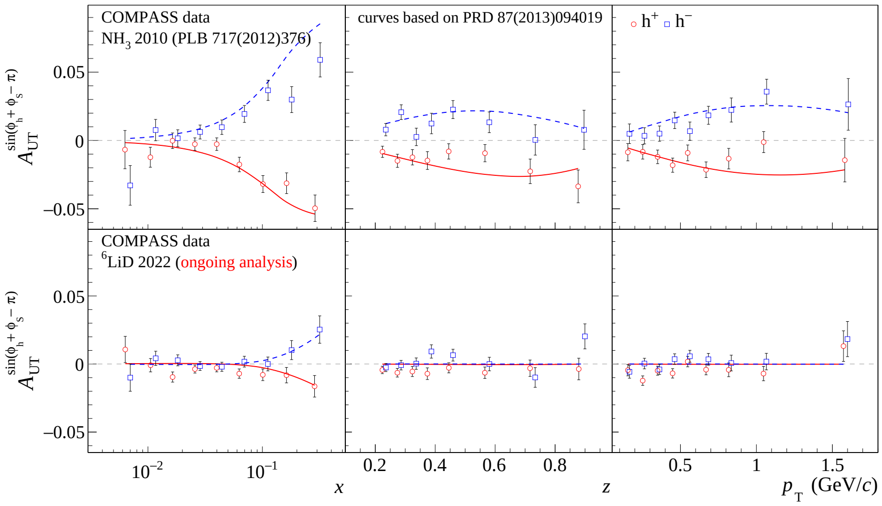

Fig. 66: COMPASS results for Collins asymmetry for proton [109] and results of the ongoing analysis of deuteron 2022 data are compared with model prediction curves based on Ref. [108]. The theoretical calculations qualitatively describe the x-dependence of the data.

The results for the Sivers TSAs do not seem to exhibit any statistically significant trends, see Fig. 65. The asymmetries appear to be small and compatible with zero within the uncertainties. Still, these data is important to further constrain the Sivers TMD PDFs.

In Fig. 67 we present the 2022 results for the Kotzinian-Mulders asymmetry and compare them with model curves evaluated based on Ref. [110]. The predictions are in agreement with out data-points, but the statistical precision of the measurement is not sufficient to make solid conclusions. However, the asymmetry tends to be positive at large x, both for positive and negative hadrons, which is in agreement with the expectations. Due to a lack of deuteron data, these results will be unique to constrain the Kotznian-Mulders TMD PDF, as suggested in Refs. [111, 112].

When the pending alignment issues are solved, we expect to gain some events in the large-polar-angle segments of the spectrometer. This may particularly affect the high x-range and further increase the statistics. Note that in August, we released and have shown at conferences only the results from half of the 2022 statistics, while in this report we presented the current status of the analysis for the entire 2022 sample.

Finally we present also the very first look at the dihadron asymmetries from 2022 deuteron data. In Fig. 68 and **??** the results of our first exploratory extraction are presented for dihadron and single-hadron ”Collins-like” and ”Sivers-like” TSAs extracted using the entire 2022 sample of oppositely charged hadron pairs. As one could expect, the trend seen at large x for the single-hadron Collins asymmetry is reflected also in the dihadron

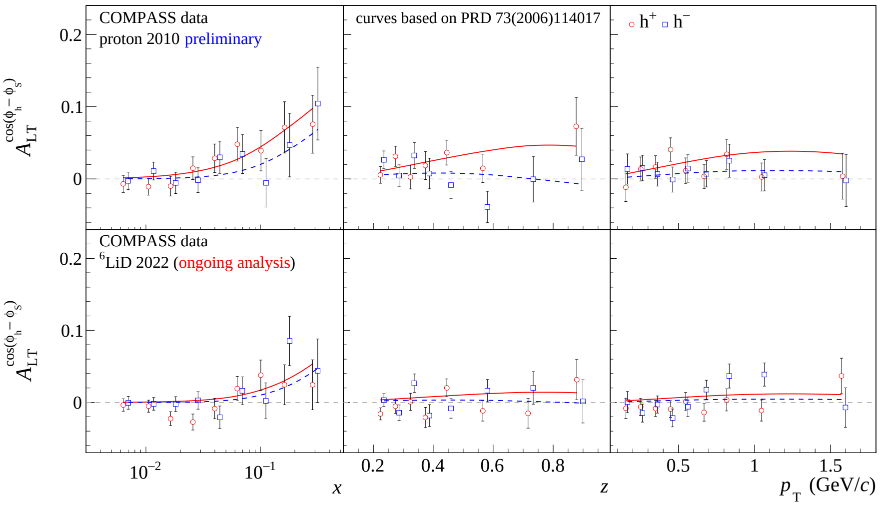

Fig. 67: Current COMPASS results for Kotzinian-Mulders asymmetry for proton target and results of the ongoing analysis of deuteron 2022 data. Theoretical curves are based on Ref. [110]. The theoretical calculations qualitatively describe the x-dependence of the data.

sample. The Sivers-like asymmetry doesn't exhibit any clear trends.

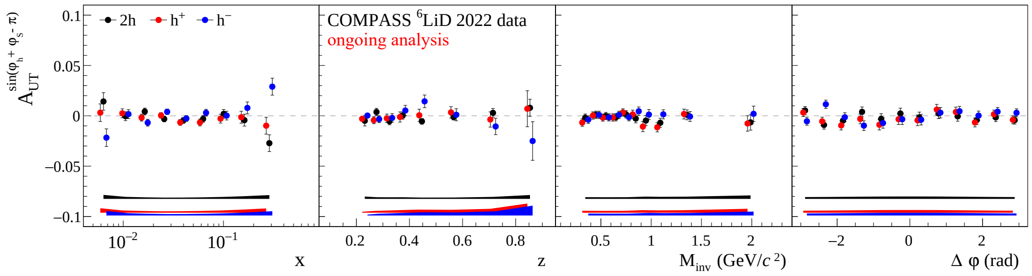

Fig. 68: Collins asymmetry: old deuteron results [101] and current results for 2022 data.

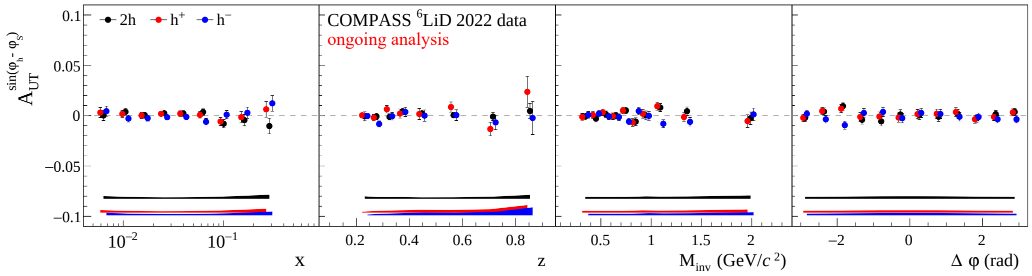

Fig. 69: Sivers asymmetry: old deuteron results [101] and current results for 2022 data.

To summarize, COMPASS 2022 data analysis is running in full swing and we have obtained first very exciting and promising results. The first article based on 2022 data is currently being drafted and is planned to be submitted by the end of 2023.

6 General status of COMPASS hardware

The COMPASS spectrometer setup used for the 2022 SIDIS Run on transversely polarised ^{6}LiD is depicted in Fig 70. The detector setup configuration is identical to the 2021 one, apart from a new GEM station included in 2022. The spectrometer performance in 2022 has been characterized by a stable DAQ and detector operation resulting in a overall spectrometer efficiency slightly above 90%. The detector interventions needed to keep the COMPASS apparatus fully operational were mostly caused to the aging of the spectrometer component like the low voltage power supply systems. The fast and effective interventions of detector experts present on site strongly reduced the impact on the detector data and minimized the beam-time loss.

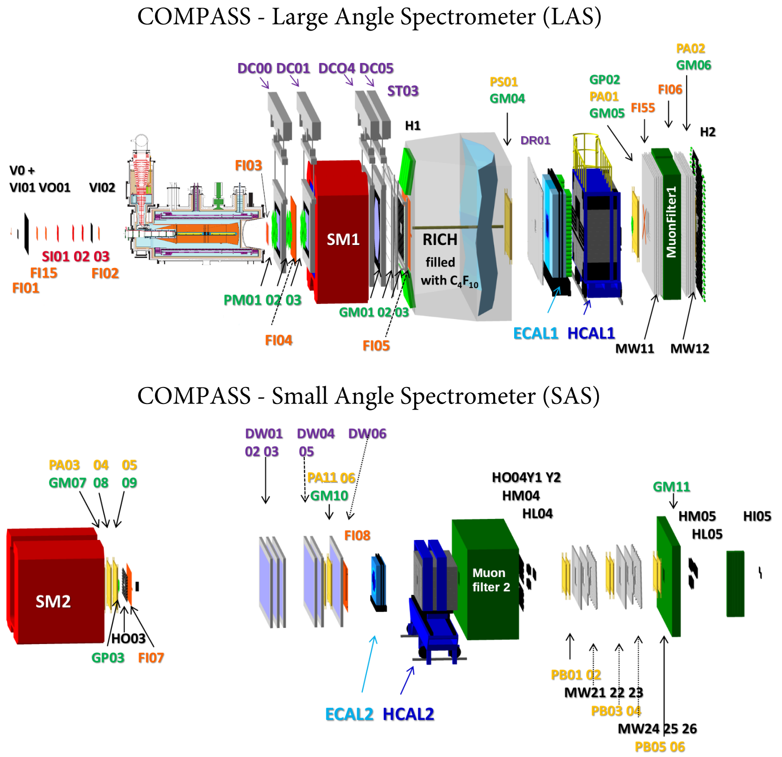
COMPASS - Large Angle Spectrometer (LAS)

COMPASS - Small Angle Spectrometer (SAS)

Fig. 70: The 2022 setup for the SIDIS transverse deuteron Run.

6.1 Polarized Target

In 2022 the COMPASS polarised target (PT), after the 2021 ^{3}He recovery line reinforcement, was for the first time operated with a system of 3 independent Gunn Diode (GD) devices. This approach has granted the possibility to fine tune the microwave frequency and power independently for each target cell, i.e. the Upstream the Central and the Downstream one during the (Dynamic Nuclear Polarization) DNP, resulting in a more homogeneous polarization level of the target material. The possibility to remotely monitor and control the GD allowed for a larger expert support from abroad. The PT pre-cooling was started on the beginning of March and the target material was loaded on 22 of March, in order to start the DNP optimization at the end of April. A polarization value averaged over the tree cells slightly larger that 40% could be obtained in 2.5 days of DNP. The PT material polarisation was lost twice during the data taking: on Friday August 26 due to the overheating of a ^{3}He pump and on Friday September 4 due to a human mistake caused by CERN cryo-operators during a cryogenic routine check.

6.2 Silicon Tracker

During the 2022 Run the silicon tracker cooling system was operated smoothly. The UV-B plane of the SI03 station cooling suffered from some cooling issues due to blockages of the capillary lines, most likely caused by a water polluting the circuit. A procedure based on heating and cooling cycles was rapidly elaborated to guarantee the nominal detector operation. As in 2021 the optimization of the operational parameters of the cooling procedure, the liquid nitrogen refilling pressure ranges and the resource shared with the PT helium liquifier, granted the stability of the detector operation.

6.3 GEMs

The 8 COMPASS standard GEM and the 2 Pixel GEMs stations operated normally during the 2022 Run. Unfortunately only one of the tree initially foreseen new GEM stations was installed in the COMPASS setup. A dedicated structure has been positioned after the second bending magnet SM2. The GEM station was installed only during the very last part of the 2022 Run. The main problems, partly not solved, included the communication loss with the APV FEE a noise level higher than expected forcing to operate the detector at very high thresholds, and firmware issues that resulted in the first latency scan taken only on November 4th.

6.4 MultiWire Proportional Chamber PB05 and PA05

The COMPASS MWPC detectors have been characterized by a good overall efficiency and stability during the whole operation period. About 100 channels of the PA04V plane have been affected repeatedly by FEE contact problems at the detector interface that could be temporarily fixed. The MWPCs PA06V1 plane experienced similar problem but the position of the electronic cards prevented any intervention. The PA05 MWPC station has been operated with the new iFTDC readout fully integrated in the COMPASS DAQ.

6.5 RICH-1

The RICH-1 detector gas radiator procured and cleaned in 2021 has granted a smooth detector operation for the entire 2022. The maintenance of the HV system as well as the refurbishment of the FEE cooling system components resulted in a fast commissioning and effective operation of the RICH-1, thanks also to the deuterium light source system installed in 2021 inside the RICH-1 vessel.

6.6 RICH WALL

The RW detector started to present data stream instability at the beginning of 2022 while commissioning. The detector was included in the COMPASS DAQ on May 30 for the start of the data taking. Part of the data stream was affected by errors traced back to the SrciD 432. On August 8 the readout of the whole detector stopped completely. Several FEE modules were exchanged, the grounding scheme was improved as well as new data cables were deployed with no success. The RW had to be excluded from the data taking and was connected to a local PC for parallel tests to investigate the source of the problem. No solution was found in time for the 2022 data taking.

6.7 Muon WALL 1 and 2

The Muon Wall 1 detector has suffered from several failures of the low voltage FEE power supply system. Three (out of in total 6) customized LV-crates have failed during the month of August 2022 requiring a delicate and complex intervention for their replacement. All the detector planes were normally operated, except of MW1Y4 plane which was affected by a larger noise than in the initial optimal configuration. Thanks to an improved grounding scheme the noise level was kept at a reasonable values.

On October 14, the Muon Wall 2 detector plane 2X was affected by very large noise level preventing the detector operation. The investigation of the problem, complicated by the scarce accessibility of the detector subsystems resulted in the identification and subsequent isolation of 5 broken tubes recovering the detector operation on October 25.

6.8 Trigger hodoscopes

The trigger system was stable and fully operational during the whole Run. After the major refurbishment in 2021, the H1 hodoscope station was highly efficient. In 2021-2022 a bulk of new PMTs was purchased in order to replace the faulty ones of the e.g. HO3 system. Due to general delivery delays the exchange of PMTs could not be performed entirely during the commissioning phase and some components were exchanged during the technical stops in the course of the Run.

6.9 DAQ

The COMPASS DAQ system was operated in fully stable conditions during the whole data taking. Further optimization of the DAQ system was necessary due to an improved spectrometer trigger timing configuration that resulted in a 5.2 Gb/spill DAQ data load, which was at the limit of the DAQ capacities. This occurred e.g. during short SPS supercycle periods (24BP, 28.8s) and high beam intensity of about 140 units on T6. New multi-threading routines have been implemented to the readout software resulting in a more efficient data processing increasing the maximum data load per spill size to 6.5 GB/spill. Several monitoring tools, extracting at each spill for each detector the data event size transferred, were further implemented guaranteeing a global control on the detector operational status.

6.10 Services

The 888 services for cooling and ventilation were in stable and operating mode since the beginning of March. All safety procedures were respected and no critical problems were faced during the entire data taking. Few temporary low pressure events affected the raw water distribution. A dedicated cleaning of the rack cooling radiator was performed to improve the heating exchange efficiency before the data taking start.

Flammable gases were made available in early May and all detectors have been progressively switched to the nominal flammable gas mixture with no issues.

Thanks to the support from the TE-CRG a degradation of the PT isolation vacuum in the distribution box was identified and timely fixed.

As in 2021 the COMPASS spectrometer detectors employing CF_4 were operated with a higher fraction of recirculated gas, in order to face the consequence of the CERN-wide gas shortage, sparing approximately 40% w.r.t. the nominal data taking configurations. With the support of EP-DT gas chromatography was performed to evaluate the gas quality of the CF_4 based detector gas mixtures. No major issues were detected apart from a large oxygen contamination of the MWPC detectors, requiring a more frequent O_2 filter exchange.

7 Hardware transfer to the AMBER experiment

The COMPASS (NA58) Experiment was approved by the CERN Research Board for a last data taking Run at the SPS in 2022 (RB240 – 16-Mar-2022). The AMBER experiment approved by the CERN Research Board for a first data taking Run at the SPS, in the beam-line used by COMPASS so far, in 2023 (RB235 – 02-Dec-2020) intends to reuse a large fraction of the COMPASS apparatus thanks also to the fact that a large fraction of member institutions of the COMPASS (NA58) Collaboration owning equipment are also member institutions of the AMBER (NA66) Collaboration; The COMPASS and AMBER collaborations have signed the agreement on the transfer of equipment and responsibility between the COMPASS (NA58) and the AMBER (NA66) Collaborations.

A dedicated survey carried out among the two collaborations allowed to identify the hardware components intended to be reused and those that on the contrary had to be disposed. The COMPASS spectrometer and dedicated detectors as well as related equipment and materials have been transferred to AMBER with an exception of two items, which are a subject to different agreements:

- The agreement between AMBER and CEA/Saclay relative to the CEA/Saclay Drift Chambers DC0, DC1 and PMM stations since the institution is not a member of the AMBER collaboration.
- the agreement between COMPASS and AMBER relative to the target material, not needed for the AMBER phase-1 program.

8 Publications and presentations at conferences

Publications

1. Double J/ψ production in pion-nucleon scattering at COMPASS ,
   PLB 838 (2023) 137702, CERN-EP-2022-073
2. Collins and Sivers transverse-spin asymmetries in inclusive muoproduction of ρ^0 mesons ,
   PLB 843 (2023) 137950, CERN-EP/2022-234
3. Spin Density Matrix Elements in Exclusive ρ^0 Meson Muoproduction
   EPJC (2023) 83 924, CERN-EP-2022-231
4. Transverse-spin-dependent azimuthal asymmetries of pion and kaon pairs produced in muon-proton and muon-deuteron semi-inclusive deep inelastic scattering
   PLB 845 (2023) 138155, CERN-EP/2022-292

Presentations at Conferences:

60 presentations at conferences and workshops between July 2022 and October 2023.

References

[1] G. D. Alexeev et al. [COMPASS], Spin density matrix elements in exclusive ρ^0 meson muoproduction, *Eur. Phys. J. C* **83** (2023) 924. [doi:10.1140/epjc/s10052-023-11359-4].

[2] [COMPASS], Transverse-spin-dependent azimuthal asymmetries of pion and kaon pairs produced in muon-proton and muon-deuteron semi-inclusive deep inelastic scattering, *Phys. Lett. B* **845** (2023) 138155. [doi:10.1016/j.physletb.2023.138155].

[3] G. D. Alexeev et al., Collins and Sivers transverse-spin asymmetries in inclusive muoproduction of ρ0 mesons, *Phys. Lett. B* **843** (2023) 137950. [doi:10.1016/j.physletb.2023.137950].

[4] G. D. Alexeev et al. [COMPASS], Double J/ψ production in pion-nucleon scattering at COMPASS, *Phys. Lett. B* **838** (2023) 137702. [doi:10.1016/j.physletb.2023.137702].

[5] M. Hoferichter, B. Kubis, and D. Sakkas, Extracting the chiral anomaly from $\gamma\pi \to \pi\pi$, *Phys. Rev.* **D86** (2012) 116009. [doi:10.1103/PhysRevD.86.116009].

[6] D. Ecker. Testing Predictions of the Chiral Anomaly in Primakoff Reactions at COMPASS. In *20th International Conference on Hadron Spectroscopy and Structure*, (2023). [doi:10.48550/arXiv.2310.09138].

[7] W. A. Smith et al. [JPAC], Ambiguities in Partial Wave Analysis of Two Spinless Meson Photoproduction, arXiv:2306.17779 (2023).

[8] E. Barrelet, A New Point of View in the Analysis of Two-Body Reactions, *Nuovo Cim. A* **8** (1972) 331–371. [doi:10.1007/BF02732655].

[9] S. U. Chung, Techniques of amplitude analysis for two pseudoscalar systems, *Phys. Rev.* **D56** (1997) 7299–7316. [doi:10.1103/PhysRevD.56.7299].

[10] J. Beckers, F. Kaspar, and J. Knollmüller. Progress in the partial-wave analysis methods at COMPASS. (2023). [doi:10.48550/arXiv.2311.00449].

[11] D. Spülbeck. Exotic Meson candidates in COMPASS data. In *17th International Workshop on Meson Physics*, (2023). [doi:10.48550/arXiv.2310.20370].

[12] C. Adolph et al. [COMPASS], Observation of a New Narrow Axial-Vector Meson a_1(1420), *Phys. Rev. Lett.* **115** (2015) 082001. [doi:10.1103/PhysRevLett.115.082001].

[13] G. D. Alexeev et al. [COMPASS], Triangle singularity as the origin of the a_1(1420), *Phys. Rev. Lett.* **127** (2021) 082501. [doi:10.1103/PhysRevLett.127.082501].

[14] C. Adolph et al. [COMPASS], Resonance production and $\pi\pi$ s-wave in $\pi^- + p \to \pi^-\pi^-\pi^+ + p_{\text{recoil}}$ at 190 GeV/c, *Phys. Rev. D* **95** (2017) 032004. [doi:10.1103/PhysRevD.95.032004].

[15] B. Guegan, J. Hardin, J. Stevens, and M. Williams, Model selection for amplitude analysis, *JINST* **10** (2015) P09002. [doi:10.1088/1748-0221/10/09/P09002].

[16] K. A. Bicker. *Model Selection for and Partial-Wave Analysis of a Five-Pion Final State at the COMPASS Experiment at CERN.* PhD thesis, Technische Universität München, (2016). URL `https://cds.cern.ch/record/2215512/`. CERN-THESIS-2016-102.

[17] O. Drotleff. *Model selection for partial-wave analysis of* $\pi^- + p \to \pi^-\pi^+\pi^- + p$ *the COMPASS experiment at CERN.* PhD thesis, Technische Universität München, (2015). URL `https://wwwcompass.cern.ch/compass/publications/theses/2015_dpl_drotleff.pdf`.

[18] F. Kaspar, Application and Verification of Model-Selection Techniques for Diffractively Produced Three-Pion Final States, Master's thesis, Technische Universität München, (2017).

[19] S. Wallner. *Exploring the Strange-Meson Spectrum with COMPASS in the Reaction* $K^- + p \to K^-\pi^-\pi^+ + p$. PhD thesis, Technische Universität München, (2022). URL `https://cds.cern.ch/record/2802793`. CERN-THESIS-2021-292.

[20] T. A. Enßlin, M. Frommert, and F. S. Kitaura, Information field theory for cosmological perturbation reconstruction and nonlinear signal analysis, *Phys. Rev. D* **80** (2009) 105005. [doi:10.1103/PhysRevD.80.105005].

[21] M. Selig, M. R. Bell, H. Junklewitz, N. Oppermann, M. Reinecke, M. Greiner, C. Pachajoa, and T. A. Ensslin, NIFTY - Numerical Information Field Theory. A versatile PYTHON library for signal inference, *aap* 554:A26. [doi:10.1051/0004-6361/201321236].

[22] T. Steininger, J. Dixit, P. Frank, M. Greiner, S. Hutschenreuter, J. Knollmüller, R. Leike, N. Porqueres, D. Pumpe, M. Reinecke, M. v Sraml, C. Varady, and T. Ensslin, NIFTy 3 - Numerical Information Field Theory - A Python framework for multicomponent signal inference on HPC clusters, arXiv:1708.01073 (2017).

[23] P. Arras, M. Baltac, T. A. Ensslin, P. Frank, S. Hutschenreuter, J. Knollmueller, R. Leike, M.-N. Newrzella, L. Platz, M. Reinecke, et al., Nifty5: Numerical information field theory v5, *Astrophysics Source Code Library* (2019).

[24] A. J. Woss, J. J. Dudek, R. G. Edwards, C. E. Thomas, and D. J. Wilson, Decays of an exotic 1^{-+} hybrid meson resonance in QCD, arXiv:2009.10034 (2020).

[25] M. Lu et al. [E852], Exotic meson decay to $\omega\pi^0\pi^-$, *Phys. Rev. Lett.* **94** (2005) 032002. [doi:10.1103/PhysRevLett.94.032002].

[26] P. Haas. Non-strange light-meson spectroscopy at COMPASS. In *20th International Conference on Hadron Spectroscopy and Structure*, (2023). [doi:10.48550/arXiv.2310.09148].

[27] M. Ablikim et al. [BESIII], Dalitz Plot Analysis of the Decay $\omega \to \pi^+\pi^-\pi^0$, *Phys. Rev. D* **98** (2018) 112007. [doi:10.1103/PhysRevD.98.112007].

[28] W. E. Cleland et al., Resonance production in the reaction $\pi^\pm p \to K^0_S K^\pm p$ at 30 and 50 GeV$/c$, *Nucl. Phys. B* **208** (1982) 228–261. [doi:10.1016/0550-3213(82)90115-8].

[29] R. L. Workman et al. [Particle Data Group], Review of Particle Physics, *PTEP* **2022** (2022) 083C01. [doi:10.1093/ptep/ptac097].

[30] S. Wallner. Strange-Meson Spectroscopy at COMPASS. In *18th International Conference on Hadron Spectroscopy and Structure* (11, 2019). [doi:10.1142/9789811219313_0019].

[31] C. Daum et al. [ACCMOR], Diffractive Production of Strange Mesons at 63 GeV, *Nucl. Phys. B* **187** (1981) 1–41. [doi:10.1016/0550-3213(81)90114-0].

[32] S. Wallner. Strange-Meson Spectroscopy with COMPASS. In *20th International Conference on Hadron Spectroscopy and Structure*, (2023). [doi:10.48550/arXiv.2310.09249].

[33] D. Ebert, R. N. Faustov, and V. O. Galkin, Mass spectra and Regge trajectories of light mesons in the relativistic quark model, *Phys. Rev. D* **79** (2009) 114029. [doi:10.1103/PhysRevD.79.114029].

[34] C. Adolph et al. [COMPASS], Resonance production and $\pi\pi$ S-wave in $\pi^- + p \to \pi^-\pi^-\pi^+ + p_\text{recoil}$ at 190 GeV$/c$, *Phys. Rev. D* **95** (2017) 032004. [doi:10.1103/PhysRevD.95.032004].

[35] C. Adolph et al. [COMPASS], Multiplicities of charged pions and charged hadrons from deep-inelastic scattering of muons off an isoscalar target, *Phys. Lett. B* **764** (2017) 1–10. [doi:10.1016/j.physletb.2016.09.042].

[36] H. Spiesberger, HERACLES and DJANGOH : Event Generation of ep Interactions at HERA Including Radiative Processes (Version 1.6) (2005). URL `http://wwwthep.physik.uni-mainz.de/~hspiesb/djangoh/djangoh.html`.

[37] M. Stolarski. COMPASS results on pion and kaon multiplicities from proton target. talk at the workshop "MENU2023", Mainz, Germany, 15–20 October 2023, (2023). URL `https://indico.him.uni-mainz.de/event/171/contributions/1409/`.

[38] C. Adolph et al. [COMPASS], Multiplicities of charged kaons from deep-inelastic muon scattering off an isoscalar target, *Phys. Lett.* **B767** (2017) 133–141. [doi:10.1016/j.physletb.2017.01.053].

[39] The COMPASS Collaboration, Compass status report 2022, *CERN-SPSC-2022-027 ; SPSC-SR-317* (2022). URL `https://cds.cern.ch/record/2811279`.

[40] A. Bacchetta, M. Diehl, K. Goeke, A. Metz, P. J. Mulders, and M. Schlegel, Semi-inclusive deep inelastic scattering at small transverse momentum, *JHEP* **02** (2007) 093. [doi:10.1088/1126-6708/2007/02/093].

[41] C. Adolph et al. [COMPASS], Measurement of azimuthal hadron asymmetries in semi-inclusive deep inelastic scattering off unpolarised nucleons, *Nucl. Phys.* **B886** (2014) 1046–1077. [doi:10.1016/j.nuclphysb.2014.07.019].

[42] J. Agarwala et al. [COMPASS], Contribution of exclusive diffractive processes to the measured azimuthal asymmetries in SIDIS, *Nucl. Phys. B* **956** (2020) 115039. [doi:10.1016/j.nuclphysb.2020.115039].

[43] L. Polano, Measurements of Azimuthal Asymmetries in SIDIS, Master's thesis, University of Trieste, (2023).

[44] The COMPASS Collaboration, Compass status report 2021, *CERN-SPSC-2021-019, SPSC-SR-294* (2021). URL `https://cds.cern.ch/record/002770989`.

[45] A. Moretti [COMPASS], Azimuthal asymmetries in unpolarized semi-inclusive deep inelastic scattering at COMPASS, *Nuovo Cim. C* **44** (2021) 61. [doi:10.1393/ncc/i2021-21061-2].

[46] A. Moretti [COMPASS], Azimuthal asymmetries and transverse momentum distributions of charged hadrons in muon-proton deep inelastic scattering, *Int. J. Mod. Phys. A* **37** (2022) 2240005. [doi:10.1142/S0217751X2240005X].

[47] K. Charchula, G. A. Schuler, and H. Spiesberger, Combined QED and QCD radiative effects in deep inelastic lepton - proton scattering: The Monte Carlo generator DJANGO6, *Computer Physics Communications* **81** (1994) 381. ISSN 0010-4655. [doi:https://doi.org/10.1016/0010-4655(94)90086-8].

[48] J. Matousek. Unpolarised Semi-Inclusive DIS at COMPASS. talk at the workshop "SPIN2023", Durham (NC), USA, 24–29 September 2023, (2023). URL `https://indico.jlab.org/event/663/contributions/13275/`.

[49] R. Akhunzyanov et al. [COMPASS], Transverse extension of partons in the proton probed in the sea-quark range by measuring the dvcs cross section, *Phys. Lett. B* **793** (2019) 188–194. [doi:https://doi.org/10.1016/j.physletb.2019.04.038].

[50] M. Alexeev et al. [COMPASS], Measurement of the cross section for hard exclusive π^0 leptoproduction, *Phys. Lett. B* **805** (2020) 135454. [doi:https://doi.org/10.1016/j.physletb.2020.135454].

[51] G. D. Alexeev et al. [COMPASS], Spin density matrix elements in exclusive ω meson muoproduction, *Eur. Phys. J. C* **81** (2021) 126. [doi:10.1140/epjc/s10052-020-08740-y].

[52] S. V. Goloskokov and P. Kroll, Transversity in hard exclusive electroproduction of pseudoscalar mesons, *Eur. Phys. J.* **A47** (2011) 112. [doi:10.1140/epja/i2011-11112-6].

[53] G. R. Goldstein, J. O. Gonzalez Hernandez, and S. Liuti, Flexible Parametrization of Generalized Parton Distributions: The Chiral-Odd Sector, *Phys. Rev. D* **91** (2015) 114013. [doi:10.1103/PhysRevD.91.114013].

[54] A. Sandacz and P. Sznajder, HEPGEN - generator for hard exclusive leptoproduction, arXiv:1207.0333 (2012).

[55] C. Regali. *Exclusive event generation for the COMPASS-II experiment at CERN and improvement of the MC chain*. PhD thesis, University of Freiburg, (2016). URL `https://freidok.uni-freiburg.de/data/11449`.

[56] S. Goloskokov and P. Kroll. private communication, adapted model for the 2012 data set, (2016).

[57] L. N. Hand, Experimental investigation of pion electroproduction, *Phys. Rev.* **129** (1963) 1834–1846. [doi:10.1103/PhysRev.129.1834].

[58] A. Aktas et al. [H1], Measurement of deeply virtual compton scattering at HERA, *Eur. Phys. J. C* **44** (2005) 1–11. [doi:10.1140/epjc/s2005-02345-3].

[59] F. D. Aaron et al. [H1], Deeply Virtual Compton Scattering and its Beam Charge Asymmetry in e+- Collisions at HERA, *Phys. Lett. B* **681** (2009) 391–399. [doi:10.1016/j.physletb.2009.10.035].

[60] S. Chekanov et al. [ZEUS], A Measurement of the Q**2, W and t dependences of deeply virtual Compton scattering at HERA, *JHEP* **05** (2009) 108. [doi:10.1088/1126-6708/2009/05/108].

[61] S. V. Goloskokov and P. Kroll, Vector meson electroproduction at small Bjorken-x and generalized parton distributions, *Eur. Phys. J. C* **42** (2005) 281–301. [doi:10.1140/epjc/s2005-02298-5].

[62] S. V. Goloskokov and P. Kroll, The role of the quark and gluon GPDs in hard vector-meson electroproduction, *Eur. Phys. J.* **C53** (2008) 367–384. [doi:10.1140/epjc/s10052-007-0466-5].

[63] S. V. Goloskokov and P. Kroll, An Attempt to understand exclusive pi+ electroproduction, *Eur. Phys. J.* **C65** (2010) 137–151. [doi:10.1140/epjc/s10052-009-1178-9].

[64] K. Kumerički and D. Mueller, Deeply virtual Compton scattering at small x_B and the access to the GPD H, *Nucl. Phys. B* **841** (2010) 1–58. [doi:10.1016/j.nuclphysb.2010.07.015].

[65] K. Kumerički and D. Müller, Description and interpretation of DVCS measurements, *EPJ Web Conf.* **112** (2016) 01012. [doi:10.1051/epjconf/201611201012].

[66] S. Chekanov et al. [ZEUS], Exclusive electroproduction of phi mesons at HERA, *Nucl. Phys. B* **718** (2005) 3–31. [doi:10.1016/j.nuclphysb.2005.04.009].

[67] A. Ali et al. [GlueX], First Measurement of Near-Threshold J/ψ Exclusive Photoproduction off the Proton, *Phys. Rev. Lett.* **123** (2019) 072001. [doi:10.1103/PhysRevLett.123.072001].

[68] S. Arnold, A. Metz, and M. Schlegel, Dilepton production from polarized hadron hadron collisions, *Phys. Rev.* **D79** (2009) 034005. [doi:10.1103/PhysRevD.79.034005].

[69] F. Gautheron et al. [COMPASS], COMPASS-II Proposal, (2010).

[70] S. Bastami, L. Gamberg, B. Parsamyan, B. Pasquini, A. Prokudin, and P. Schweitzer, The Drell-Yan process with pions and polarized nucleons, *JHEP* **02** (2021) 166. [doi:10.1007/JHEP02(2021)166].

[71] A. Kotzinian, New quark distributions and semiinclusive electroproduction on the polarized nucleons, *Nucl. Phys.* **B441** (1995) 234–248. [doi:10.1016/0550-3213(95)00098-D].

[72] A. Airapetian et al. [HERMES collaboration], Observation of the Naive-T-odd Sivers Effect in Deep-Inelastic Scattering, *Phys. Rev. Lett.* **103** (2009) 152002. [doi:10.1103/PhysRevLett.103.152002].

[73] C. Adolph et al. [COMPASS], Collins and Sivers asymmetries in muonproduction of pions and kaons off transversely polarised protons, *Phys. Lett.* **B744** (2015) 250–259. [doi:10.1016/j.physletb.2015.03.056].

[74] D. W. Sivers, Single Spin Production Asymmetries from the Hard Scattering of Point-Like Constituents, *Phys. Rev.* **D41** (1990) 83. [doi:10.1103/PhysRevD.41.83].

[75] J. C. Collins, Leading-twist Single-transverse-spin asymmetries: Drell- Yan and Deep-Inelastic Scattering, *Phys. Lett.* **B536** (2002) 43–48. [doi:10.1016/S0370-2693(02)01819-1].

[76] S. J. Brodsky, D. S. Hwang, and I. Schmidt, Final state interactions and single spin asymmetries in semiinclusive deep inelastic scattering, *Phys. Lett.* **B530** (2002) 99–107. [doi:10.1016/S0370-2693(02)01320-5].

[77] S. J. Brodsky, D. S. Hwang, and I. Schmidt, Initial state interactions and single spin asymmetries in Drell-Yan processes, *Nucl. Phys.* **B642** (2002) 344–356. [doi:10.1016/S0550-3213(02)00617-X].

[78] J. Collins, *Foundations of perturbative QCD* (Cambridge University Press, 2013). ISBN 9781107645257, 9781107645257, 9780521855334, 9781139097826. URL `http://www.cambridge.org/de/knowledge/isbn/item5756723`.

[79] C. Adolph et al. [COMPASS], Sivers asymmetry extracted in SIDIS at the hard scales of the Drell–Yan process at COMPASS, *Phys. Lett. B* **770** (2017) 138–145. [doi:10.1016/j.physletb.2017.04.042].

[80] M. Anselmino, V. Barone, and M. Boglione, The Sivers asymmetry in Drell–Yan production at the J/Ψ peak at COMPASS, *Phys. Lett.* **B770** (2017) 302–306. [doi:10.1016/j.physletb.2017.04.074].

[81] W.-C. Chang, J.-C. Peng, S. Platchkov, and T. Sawada, Constraining gluon density of pions at large x by pion-induced J/ψ production, *Phys. Rev. D* **102** (2020) 054024. [doi:10.1103/PhysRevD.102.054024].

[82] P. Faccioli, I. Krätschmer, and C. Lourenço, Quarkonium polarization in low-p_{T} hadro-production: from past data to future opportunities, arXiv:2210.09845 (2022).

[83] M. Aghasyan et al. [COMPASS], First measurement of transverse-spin-dependent azimuthal asymmetries in the Drell-Yan process, *Phys. Rev. Lett.* **119** (2017) 112002. [doi:10.1103/PhysRevLett.119.112002].

[84] B. A. Kniehl, D. V. Vasin, and V. A. Saleev, Charmonium production at high energy in the k_T -factorization approach, *Phys. Rev. D* **73** (2006) 074022. [doi:10.1103/PhysRevD.73.074022].

[85] A. V. Karpishkov, M. A. Nefedov, and V. A. Saleev, $B\bar{B}$ angular correlations at the LHC in parton Reggeization approach merged with higher-order matrix elements, *Phys. Rev. D* **96** (2017) 096019. [doi:10.1103/PhysRevD.96.096019].

[86] A. V. Karpishkov, M. A. Nefedov, and V. A. Saleev, Spectra and polarizations of prompt J/ψ at the NICA within collinear parton model and parton Reggeization approach, *J. Phys. Conf. Ser.* **1435** (2020) 012015. [doi:10.1088/1742-6596/1435/1/012015].

[87] C. Adolph et al. [COMPASS], Transverse spin effects in hadron-pair production from semi-inclusive deep inelastic scattering, *Phys. Lett.* **B713** (2012) 10–16. [doi:10.1016/j.physletb.2012.05.015].

[88] F. Arleo and S. Peigné, Heavy-quarkonium suppression in p-A collisions from parton energy loss in cold QCD matter, *JHEP* **2013** (2013). [doi:10.1007/JHEP03(2013)122].

[89] J. Conway et al. [E615 Collaboration], *Phys. Rev. D* **39** (1989) 92.

[90] B. Betev et al. [NA10], DIFFERENTIAL CROSS-SECTION OF HIGH MASS MUON PAIRS PRODUCED BY A 194-GeV/c pi- BEAM ON A TUNGSTEN TARGET, *Z. Phys.* **C28** (1985) 9. [doi:10.1007/BF01550243].

[91] W. J. Stirling and M. R. Whalley, A Compilation of Drell-Yan cross-sections, *J. Phys. G* **19** (1993) D1–D102. [doi:10.1088/0954-3899/19/D/001].

[92] J. S. Conway et al., Experimental Study of Muon Pairs Produced by 252-GeV Pions on Tungsten, *Phys. Rev.* **D39** (1989) 92–122. [doi:10.1103/PhysRevD.39.92].

[93] A. Kotzinian and J. Mulders, Longitudinal quark polarization in transversely polarized nucleons, *Phys. Rev.* **D54** (1996) 1229–1232.

[94] A. M. Kotzinian and P. J. Mulders, Probing transverse quark polarization via azimuthal asymmetries in leptoproduction, *Phys. Lett. B* **406** (1997) 373–380. [doi:10.1016/S0370-2693(97)00708-9].

[95] D. Boer and P. J. Mulders, Time-reversal odd distribution functions in leptoproduction, *Phys. Rev.* **D57** (1998) 5780–5786. [doi:10.1103/PhysRevD.57.5780].

[96] M. G. Alexeev et al. [COMPASS], Measurement of P_T-weighted Sivers asymmetries in leptoproduction of hadrons, *Nucl. Phys. B* **940** (2019) 34–53. [doi:10.1016/j.nuclphysb.2018.12.024].

[97] xFitter [xFitter - A PDF fit program from HERA], (2014). URL `https://gitlab.cern.ch/fitters/xfitter`.

[98] M. Cerutti, L. Rossi, S. Venturini, A. Bacchetta, V. Bertone, C. Bissolotti, and M. Radici [MAP (Multi-dimensional Analyses of Partonic distributions)], Extraction of pion transverse momentum distributions from Drell-Yan data, *Phys. Rev. D* **107** (2023) 014014. [doi:10.1103/PhysRevD.107.014014].

[99] A. Martin. New measurements of transverse spin asymmetries at COMPASS. talk at the workshop “SPIN2023”, Durham (NC), USA, 24–29 September 2023, (2023). URL `https://indico.jlab.org/event/663/contributions/13273/`.

[100] M. Diehl and S. Sapeta, On the analysis of lepton scattering on longitudinally or transversely polarized protons, *Eur. Phys. J. C* **41** (2005) 515–533. [doi:10.1140/epjc/s2005-02242-9].

[101] E. S. Ageev et al. [COMPASS], A New measurement of the Collins and Sivers asymmetries on a transversely polarised deuteron target, *Nucl. Phys. B* **765** (2007) 31–70. [doi:10.1016/j.nuclphysb.2006.10.027].

[102] C. Adolph et al. [COMPASS], Experimental investigation of transverse spin asymmetries in muon-p SIDIS processes: Collins asymmetries, *Phys. Lett. B* **717** (2012) 376–382. [doi:10.1016/j.physletb.2012.09.055].

[103] C. Adolph et al. [COMPASS], II – Experimental investigation of transverse spin asymmetries in μ -p SIDIS processes: Sivers asymmetries, *Phys. Lett. B* **717** (2012) 383–389. [doi:10.1016/j.physletb.2012.09.056].

[104] P. J. Mulders and R. D. Tangerman, The Complete tree level result up to order 1/Q for polarized deep inelastic leptoproduction, *Nucl. Phys. B* **461** (1996) 197–237. [doi:10.1016/0550-3213(95)00632-X]. [Erratum: Nucl.Phys.B 484, 538–540 (1997)].

[105] W. Mao, Z. Lu, B.-Q. Ma, and I. Schmidt, Double spin asymmetries $A_{LT}^{\cos\phi_S}$ and $A_{LT}^{\cos(2\phi_h-\phi_S)}$ in semi-inclusive DIS, *Phys. Rev. D* **91** (2015) 034029. [doi:10.1103/PhysRevD.91.034029].

[106] K. Augsten et al. [COMPASS Collaboration], Addendum to the COMPASS-II Proposal: d-Quark Transversity and Proton Radius, *CERN–SPSC–2017–034, SPSC-P-340-ADD-1* (2018).

[107] C. Adolph et al. [COMPASS], Transverse spin effects in hadron-pair production from semi-inclusive deep inelastic scattering, *Phys. Lett. B* **713** (2012) 10–16. [doi:10.1016/j.physletb.2012.05.015].

[108] M. Anselmino, M. Boglione, U. D'Alesio, S. Melis, F. Murgia, and A. Prokudin, Simultaneous extraction of transversity and Collins functions from new SIDIS and e+e- data, *Phys. Rev. D* **87** (2013) 094019. [doi:10.1103/PhysRevD.87.094019].

[109] C. Adolph et al. [COMPASS], II – Experimental investigation of transverse spin asymmetries in μ -p SIDIS processes: Sivers asymmetries, *Phys. Lett. B* **717** (2012) 383–389. [doi:10.1016/j.physletb.2012.09.056].

[110] A. Kotzinian, B. Parsamyan, and A. Prokudin, Predictions for double spin asymmetry A(LT) in semi inclusive DIS, *Phys. Rev. D* **73** (2006) 114017. [doi:10.1103/PhysRevD.73.114017].

[111] S. Bhattacharya, Z.-B. Kang, A. Metz, G. Penn, and D. Pitonyak, First global QCD analysis of the TMD g1T from semi-inclusive DIS data, *Phys. Rev. D* **105** (2022) 034007. [doi:10.1103/PhysRevD.105.034007].

[112] M. Horstmann, A. Schafer, and A. Vladimirov, Study of the worm-gear-T function g1T with semi-inclusive DIS data, *Phys. Rev. D* **107** (2023) 034016. [doi:10.1103/PhysRevD.107.034016].